BEHAVIOR OF BIOLOGICAL AND AQUEOUS SYSTEMS AT LOW TEMPERATURE

A Dissertation

Presented to the Faculty of the Graduate School

of Cornell University

In Partial Fulfillment of the Requirements for the Degree of

Doctor of Philosophy

by

Matthew Adam Warkentin

February 2010

BEHAVIOR OF BIOLOGICAL AND AQUEOUS SYSTEMS AT LOW TEMPERATURE

Matthew Adam Warkentin, Ph. D.

Cornell University 2010

The fields of protein crystallography, cryo-electron microscopy and cryopreservation require that aqueous biological samples or aqueous solutions be cooled to very low temperatures. The outcomes of experiments in those fields also depend on the behavior of the water contained in such samples. This makes understanding that behavior central to such experiments, even if that understanding is not the aim of the research. In particular, samples often must be cooled so that the water is in a metastable amorphous state, i.e. so that no crystalline ice forms.

This dissertation covers topics ranging from the very practical matter of how this metastable state can be achieved and maintained to more fundamental questions surrounding its formation. A cheap and simple method by which tiny samples can be cooled at very high rates is demonstrated, which will allow cooling at rates previously requiring expensive and complicated apparatus. The relationship between the cooling rate required to produce an amorphous sample and the amount of solute in the sample is demonstrated to be a simple exponential, which may indicate the fundamental mechanism by which ice forms from supercooled solution. Finally, the radiation sensitivity of protein crystals is shown to be linked with the diffusive motions of the supercooled solvent within them: radiation sensitivity is suppressed by lowering the temperature because diffusive motion is also suppressed.

BIOGRAPHICAL SKETCH

Matthew was born in Portland, Oregon in 1982. He attended Banks High School in Banks, Oregon and developed an interest in physics outside of school. He attended the University of California at Santa Cruz, earning a degree in Physics. His undergraduate thesis project there involved the analysis and interpretation of EXAFS data, which impressed upon him the tremendous power of synchrotron X-rays as a tool to understand the world. In August of 2004 he entered the graduate program in physics at Cornell University with the intention of doing experimental research using the synchrotron at Cornell. In June of 2005 he began his research in the group of Robert Thorne, with this dissertation as one result.

ACKNOWLEDGMENTS

I would like to thank the professors that I learned so much from during my undergrad. In particular: Zach Schlesinger, Josh Deutsch, Onuttom Narayan, and Frank “Bud” Bridges. These people taught me how to think about physics problems, and, in the case of Bud, how to think about research.

I must also thank the people in my life who have provided the essential emotional support that any normal human needs: My family, and my housemates in Ithaca. In particular I need to thank Ryan Shannon for making me lunch every day.

I want to express my gratitude for having had Rob Thorne as an advisor. He has given me just the right amount of guidance and encouragement as I pursued my research projects.

I will acknowledge financial support from the physics department at Cornell, the Department of Education, the National Institutes of Health, and the Cornell High Energy Synchrotron Source (CHESS, and MacCHESS).

TABLE OF CONTENTS

LIST OF FIGURES

CHAPTER 1

INTRODUCTION

Water is an unusual substance in many respects. It is ubiquitous on earth and in many astrophysical objects. The molecule itself has a simple structure. It is of course essential for life. For these and other reasons it ranks among the most studied of all substances, and as a result it is very well understood. It serves as the canonical example for countless phenomena, at all stages of our education, including heat capacities and latent heats, surface tension, phase transformations, and "the three phases of matter". One phenomenon for which it is not particularly known is glass formation. This is because it is a poor glass former.

Water is a poor glass former in two senses of the phrase. Literally, it is a poor glass former because it requires a comparatively large cooling rate to avoid crystallization. But it is also a poor glass former because it is a poorly understood glass former. It doesn't seem to follow the same rules as most other glass forming substances, and so the lessons from the study of other glasses don't always apply to water. There is every reason to understand it, though, because the glassy behavior of water is important to many diverse fields.

Cryo-electron microscopy, macromolecular crystallography, and cryopreservation all rely on the glassy (or amorphous) state of water. The goal of a particular study might be to determine the structure of a protein or virus, understand how misfolded proteins cause disease, or even to produce a panda from frozen semen, but the glassy state of water will be important in every case. This is because the transformation to the crystalline state of water is discontinuous, and often distorts the data to the point of

irrelevance or else prevents data collection altogether. In the case of cryopreservation, it may damage or destroy whatever is being preserved.

An overarching theme in this thesis is the cooling of small aqueous samples. The remainder of this introduction will serve as an introduction to the field, and a guide to the chapters.

In 1985, Erwin Mayer reported the vitrification of pure water by splat-cooling ~10 μm-sized droplets on a copper plate. (Mayer, 1985) It was reckoned that the required cooling rate for vitrification was 10^5 - 10^6 K/s, which has been supported by experiments that followed. (Johari *et al*., 1987; Huang & Bartell, 1994) The vitrification of water is of central importance to the fields of cryopreservation, cryoelectron microscopy, and macromolecular crystallography.

The classic review of vitrification for cryoelectron microscopy was written by Dubochet *et al*. (1988). The reason vitrification is necessary for electron microscopy of biological specimens is twofold: First, the formation of nanometer- to micron-sized ice clusters disrupts the biological structures that exist on those same length scales which are the aim of the study. Second, the sharp contrast between the amorphous and crystalline phases in the sample obscure the (often lesser) contrast between different types of biological structure.

In practice, vitrification is achieved by cooling small samples, and using liquid cryogens such as propane and ethane. Samples of characteristic size ~50 μm or smaller are common in this field, and allow cooling rates approaching 100,000 K/s. Another important point is made by Zasadzinski (1988) and Zasadzinski & Bailey

(1991): for the cooling conditions of interest for electron microscopy (small samples, cooling in liquid propane or ethane), the process of cooling is well approximated by the so-called "lumped approximation". In this approximation, the sample is regarded as having a constant temperature throughout, with a thermal gradient in the cryogen at its surface. This simplification implies that the sample is completely described by its thermal mass and surface-to-volume ratio. That is, the sample's composition only matters insofar as the thermal mass is concerned. Since there are no gradients in the sample, its thermal conductivity is irrelevant to the cooling rate, and every part cools at the same rate.

Cryopreservation also concerns itself with the cooling of aqueous biological samples, but the cooling regime is completely different. Mazur (1970) provides a review. Samples tend to be very large (centimeters), so that cooling rates are limited to ~1 K/s or slower. Because of this, large amounts (~50 %) of cryoprotectant (alcohols, glycerol, sugars, etc) must be added to prevent (or control) ice formation during cooling. The nucleation and growth of ice in these aqueous solutions is has been studied for decades (Mackenzie, 1977), but studies have been limited to very slow cooling rates (~1 K/s or slower). Correspondingly large concentrations of cryoprotectant are typically employed, which limits the parallels that can be drawn to the experience of the electron microscopy community.

Cryocooling in protein crystallography is at the intersection between these two cooling regimes. Samples can be as large as 0.5 - 1.0 mm, (if the liquid surrounding the crystal is included), or as small as 5 - 10 μm. This means that both rapid cooling and cryoprotectants are involved in the process of cooling protein crystals. The present day methods for cryocooling in protein crystallography were developed in the late 80s

and early 90s. (Hope, 1988; Hope, 1990; Rodgers, 1994) Since that time, some attention has been paid to the systematic study of the methods. A recent systematic exploration of the effect of flash-freezing temperature on the quality of nucleosome crystals (Edayathumangalam & Luger, 2005) suggests that if more attention is paid to the details of protein crystal freezing, substantial gains might be made in practice. However, this is still an exceptional case, as most systems do not attract the kind of intense study as the nucleosome.

Cooling rates using "standard methods" have been measured to be in the 100 - 1000 K/s range (Walker *et al*., 1998; Teng & Moffat, 1998), but no systematic effort has been made to determine their effect on experimental outcomes. Of course, faster cooling does reduce concentration of cryoprotectant needed, but experimenters have chosen to focus on sample size, as opposed to cooling rate, as the determinant of the needed concentration. (Chinte *et al*., 2005; Berejnov *et al*., 2006) Theoretical work has argued that protein crystallography samples can be considered to be in the "lumped model" regime of heat transfer (Kriminski *et al*., 2003), unless very efficient cryogens (propane, ethane) are employed.

This dissertation covers a number of topics, each related to the behavior of water at low temperatures. Some are very practical, like Chapters 2 and 3, others are a mixture of practical methods and fundamental science. Each chapter begins with a technical introduction and review of the literature. Here, a brief summary is given only, with as little jargon as possible.

Chapter 2 deals with the problem of cooling samples rapidly. As mentioned above, water is a poor glass former, which means that it must be cooled at a very high rate

(about 1 million degrees Kelvin per second) to avoid the formation of crystalline ice. Depending on how many (and what kind) of molecules are dissolved in a solution, the required cooling rate will be lower. What this means is that the faster an experimenter can cool their samples, the wider a range of solute concentrations the samples may contain and still be studied at low temperature.

In both cryo-electron microscopy and protein crystallography, samples are cooled to low temperatures to reduce the harmful effects of the radiation (electrons or X-rays) that are inherent to the experiment. Expensive robots exist that can attain cooling rates of 100,000 K/s and are commonly used for cryo-electron microscopy experiments, but in for protein crystallography, simply plunging samples into a dewar of liquid nitrogen is the most common method. While it should be possible to achieve cooling rates in the 10 – 20 kK/s range with liquid nitrogen, it was found that cooling rates were limited to the hundreds of K/s. The reason for this turned out to be very simple.

A dewar of liquid nitrogen sitting on a lab bench will be at its boiling point (77.25 K), and so it will be constantly evolving fresh gas. This gas will form a layer above the liquid, with warmer gas at the top and colder gas at the bottom. Large samples are not affected by the gas layer, but smaller ones (which should cool faster in the liquid) instead cool in the gas as they are plunged into the dewar. The result is a limiting cooling rate about 20 times slower than would be possible without the gas layer for a 100 micron sample.

The solution to this problem was just as simple as the problem itself: direct a stream of warm, dry nitrogen gas at the liquid. The size of the cold gas layer is reduced to under

100 microns, and cooling rates during plunging are what they should be (Warkentin *et al*., 2006)

Tiny samples are advantageous in that they can be cooled very rapidly, but care must be taken because they are so sensitive to thermal variations. This is the subject of Chapter 3. Once a sample is frozen, it must be kept at liquid nitrogen temperature during transportation and mounting in the experimental apparatus. In the case of protein crystallography, storage of samples is under liquid nitrogen, but data collection takes place in a stream of cold nitrogen gas. During the transfer process from liquid to gas, there is the possibility for the sample to warm up briefly, which nullifies whatever effect the initial rapid cooling might have had.

This chapter describes measurements of the sample temperature during this mounting process, showing that small enough samples can indeed warm to unacceptably high temperatures. The reason for the warming is investigated using schlieren imaging of the cold gas stream during the transfer process. Schlieren imaging allows for thermal gradients (between regions of warm and cold gas) to be displayed in sharp contrast. Videos were recorded of the sample as it was placed into the cold gas stream, and turbulent mixing of warm and cold gas can be clearly seen at the sample position.

To overcome this difficulty, a method was developed that keeps the sample wetted with liquid nitrogen during the entire mounting process. A stream of liquid nitrogen is directed at the sample position prior to mounting, and only removed after the sample is in place. The measured sample temperatures using this method showed no sign of warming, implying that the effects of rapid cooling had been preserved.

Chapter 4 focuses on aqueous samples in small capillaries, and would apply as well to rod-shaped samples, such as muscle fibers. First, the rate at which capillaries of various sizes can be cooled in liquid nitrogen and liquid propane was measured. Tubes with diameters as low as 150 microns are investigated. Not surprisingly, smaller tubes cool more rapidly than large ones, with a relationship that can be predicted theoretically in some (but not all) cases. Since capillaries of a given diameter cool at a given rate, there will be some concentration of solute (in this case glycerol) that will yield a glassy sample. So next, this "critical concentration" was determined for each diameter of capillary as well.

These findings are important for protein crystallography because doing experiments on crystals frozen into capillaries has been proposed as a method that could simplify data collection. If samples are to be cooled in capillaries, experimenters will need to know how much of a given solute will yield a glassy sample. On a more fundamental level, the amount of solute should not depend on the capillary diameter at all, it should only depend on the cooling rate of the sample. So there is a fundamental relationship revealed by the data in Chapter 4 as well: The critical cooling rate for glass formation as a function of solute concentration. This study has determined this quantity up to cooling rates approaching 10,000 K/s, a hundred times higher than in any previous study. The result is a clear exponential dependence, which extrapolates to the correct value for pure water. (Warkentin *et al*., 2008)

This fundamental relationship is explored further in Chapter 5, where a variety of solutes are studied. Each one shows an exponential dependence of critical cooling rate on solute concentration, but the characteristic of the exponential is different for each solute. One explanation for the exponential dependence is that the solutes modify the

free energy barrier to the formation of the critical nucleus. If this were the case, the characteristic of the exponential would be related to the critical nucleation radius – a fundamentally important quantity. The characteristic is correlated with the size of the solute however, so the data cannot be interpreted unambiguously.

In Chapter 6, it is shown that the channels of a protein crystal are at least as effective at suppressing ice formation as a very large amount of solute (70 % glycerol, for example). This is demonstrated by cooling protein crystals very slowly (at 0.1 K/s, ten-million times slower than the rate required to prevent ice formation in pure water). Despite the very slow cooling, and the large water content of the protein crystals studied (56 % by volume), no ice forms at any temperature. This result is of important practical consequence: it opens the door to the study of protein crystals at any temperature from room temperature down to very low temperature. (Warkentin & Thorne, 2009)

In Chapter 7, one such temperature-dependent study is described. The radiation sensitivity of protein crystals is measured as a function of temperature, at temperatures ranging from room temperature down to 100 Kelvin. This covers the full range of temperatures likely to be of interest in protein crystallography. The radiation sensitivity is shown to be tied to the diffusive motions of protein and solvent atoms inside the protein crystal down to 170 Kelvin, where diffusive motion is believed to cease. Below that temperature, the radiation sensitivity is relatively constant, in accord with other organic crystals in which there is no diffusive motion.

With the results of Chapters 6 and 7, all the pieces are in place for temperature dependent studies of proteins in crystals, including the interesting temperature range near 200 K, where biological activity has been shown to first appear.

REFERENCES

Bailey, S. M. & Zasadzinski, J. A. N. (1991). *Journal of Microscopy-Oxford* **163**, 307-320.

Bartell, L. S. & Huang, J. F. (1994). *Journal of Physical Chemistry* **98**, 7455-7457.

Berejnov, V., Husseini, N. S., Alsaied, O. A., & Thorne, R. E. (2006). *Journal of Applied Crystallography* **39**, 244-251.

Chinte, U., Shah, B., DeWitt, K., Kirschbaum, K., Pinkerton, A. A., & Schall, C. (2005). *Journal of Applied Crystallography* **38**, 412-419.

Dubochet, J., Adrian, M., Chang, J. J., Homo, J. C., Lepault, J., Mcdowall, A. W., & Schultz, P. (1988). *Quarterly Reviews of Biophysics* **21**, 129-228.

Edayathumangalam, R. S. & Luger, K. (2005). *Acta Crystallographica Section D-Biological Crystallography* **61**, 891-898.

Hope, H. (1988). *Acta Crystallographica Section B-Structural Science* **44**, 22-26.

Hope, H. (1990). *Annual Review of Biophysics and Biophysical Chemistry* **19**, 107-126.

Johari, G. P., Hallbrucker, A., & Mayer, E. (1987). *Nature* **330**, 552-553.

Kriminski, S., Kazmierczak, M., & Thorne, R. E. (2003). *Acta Crystallographica Section D-Biological Crystallography* **59**, 697-708.

Mackenzie, A. P., Derbyshire, W., & Reid, D. S. (1977). *Philosophical Transactions of the Royal Society of London Series B-Biological Sciences* **278**, 167-&.

Mayer, E. (1985). *Journal of Applied Physics* **58**, 663-667.

Mazur, P. (1970). *Science* **168**, 939-&.

Rodgers, D. W. (1994). *Structure* **2**, 1135-1140.

Teng, T. Y. & Moffat, K. (1998). *Journal of Applied Crystallography* **31**, 252-257.

Walker, L. J., Moreno, P. O., & Hope, H. (1998). *Journal of Applied Crystallography* **31**, 954-956.

Warkentin, M., Berejnov, V., Husseini, N. S., & Thorne, R. E. (2006). *Journal of Applied Crystallography* **39**, 805-811.

Warkentin, M., Stanislavskaia, V., Hammes, K., & Thorne, R. E. (2008). *Journal of Applied Crystallography* **41**, 791-797.

Warkentin, M., & Thorne, R. E. (2009). *Journal of Applied Crystallography* **42**, (in press.)

Zasadzinski, J. A. N. (1988). *Journal of Microscopy-Oxford* **150**, 137-149.

CHAPTER 2

HYPERQUENCHING FOR PROTEIN CRYSTALLOGRAPHY

2.1 Introduction

The introduction of cryocrystallographic methods in the late 1980's revolutionized the determination of protein structures by X-ray diffraction (Hope, 1988; Hope, 1990). As is known from cryoelectron microscopy (Zeitler, 1982; Dubochet et al., 1982), lowering the sample's temperature to cryogenic temperatures (~100 K) dramatically reduces radiation damage, because the glass transition temperature for solvent within crystals is typically in the range 150-200 K. (Weik et al., 2001; Weik et al., 2005). Diffusion of atomic and molecular radicals produced by irradiation is greatly reduced, and the rigidified water network provides a scaffold for the protein that prevents large motions in response to local damage. With advances in synchrotron X-ray sources, optics and X-ray detectors, cryocrystallographic methods now allow complete data sets to be obtained from macromolecular crystals smaller than 10 μm. It is generally assumed (although seldom verified in detail (Earnest et al., 1991)) that the low temperature structures correspond to the biologically active form.

Despite these triumphs, cryopreservation of protein crystals has remained a problematic art (Juers and Matthews, 2004). Protein crystal order and especially mosaicity nearly always degrade during flash cooling. Many cooled crystals do not yield usable diffraction. Formation of hexagonal ice both inside and outside the crystal can damage it and introduce ice rings that interfere with diffraction from the protein lattice. Ice rings can be eliminated and damage reduced by cooling fast enough to obtain vitreous or amorphous ice. For pure water, the required cooling rates are ~10^6

K/s (Bruggeller & Mayer, 1980; Johari et al, 1987), orders of magnitude larger than those achieved in current cryocrystallography practice. Adding cryoprotectants such as glycerol, ethylene glycol, and MPD can reduce required cooling rates to 10^2 K/s or less (Peyridieu et al., 1996; Lu & Liu, 2003). Unfortunately, cryoprotectants can be unfriendly to the protein's native conformation, they can cause osmotic stress, and they affect protein solubility, and so can cause crystal cracking, dissolution and structural changes, especially at the relatively high concentrations (20-30% w/v) used in current practice. Furthermore, internal solvent (whose crystallization is strongly inhibited by the protein) and external solvent should in general be cryoprotected differently (Kriminski et al., 2002). As a result, optimizing cryoprotectant conditions can be time consuming.

Protein crystals are cooled by direct insertion into a stream of cold nitrogen gas at T~100 K, or by plunging into liquid nitrogen (Tv=77 K) or liquid propane (T_m=86 K) (Rodgers, 1994; Chayen et al., 1996; Garman & Schneider 1997; Garman, 1999; Pflugrath, 2004). Simple physical arguments, scaling analysis (Kriminski et al., 2003) and the experience of cryoelectron microscopists clearly suggest that plunge cooling in liquid cryogens should produce far larger cooling rates and thus better (or at least different) diffraction outcomes than gas stream cooling. However, diffraction outcomes obtained using cold gases and liquids have not differed substantially, and two studies to determine the most effective method (Teng & Moffat, 1998; Walker et al., 1998) reached different conclusions, so that both methods remain in wide use (Garman & Owen, 2006). Even more puzzling — and troubling — is that the measured cooling rates achieved in conventional plunge or gas stream cooling of ordinary-size samples (200-1500 K/s) are small (Teng & Moffat, 1998; Walker et al., 1998). Crystals take a fraction of a second to cool below water's glass transition

temperature and on the order of 0.1 s to cool below T=220 K (Snell et al., 2002), where conformational motions are largely frozen out (Fraunenfelder et al., 1979; Tilton et al., 1992; Halle, 2004).

Here we show that during plunge cooling into liquid cryogens of the small volume (<0.1 μl) samples typical in protein crystallography, the cooling rate in the critical region between room temperature and T=150 K is controlled not by the liquid but by heat transfer to the cold gas layer that exists above it. By removing this cold gas layer, cooling rates can be increased to at least 1.5×10^4 K/s in liquid nitrogen and cooling times reduced to <10 ms to reach 77 K (the temperature of boiling liquid nitrogen). With these high cooling rates, cryoprotectant concentrations required to achieve vitrification of water-glycerol mixtures are reduced from ~30% to less than 6% w/v. Consequently, cooling-induced crystal damage should be reduced, and cryoprotectant screening should be simplified.

2.2 Methods and Results

2.2.1 Plunge cooling of small volumes: A puzzle

To obtain vitreous ice, the time to cool to below Tg should be shorter than the characteristic time for nucleation of crystalline ice. Cryoprotectants like glycerol slow down or inhibit crystalline ice nucleation, decreasing the required cooling rate. Smaller volume samples have larger surface-to-volume ratios and should cool more quickly, decreasing the required cryoprotectant concentration. An elementary analysis suggests that the cooling rate should scale as $V^{-1/2}$ (Kriminski et al., 2003).

Berejenov et al. (2006) examined the minimum concentration required to achieve vitrification of aqueous mixtures of fourteen different cryoprotectants as a function of the liquid volume V, for plunge cooling in liquid nitrogen using standard methods. As illustrated in Figure 2.1 (open circles) for glycerol, at large volumes (>10 μl) Berejnov et al. found that the required cryoprotectant concentration is large and independent of volume, as expected in the limit when cooling rates are so slow that nucleation must be completely inhibited. At smaller volumes, the cryoprotectant concentration decreases with decreasing volume, as expected based on the argument in the preceding paragraph. However, for volumes below ~0.1 μl — for glycerol and all other cryoprotectants studied by Berejnov et al. — the required cryoprotectant concentration becomes roughly independent of volume. Similar volume-independent glycerol concentrations were required for volumes below ~0.1 μl when drops were plunge cooled in liquid propane. This volume range corresponds to crystals smaller than about 500 μm in all three dimensions, i.e., to essentially all crystals of interest in macromolecular X-ray crystallography.

The apparent small-volume saturation found by Berejnov et al. cannot represent an intrinsic feature of glycerol-water mixtures because pure water can be vitrified at high cooling rates (Mayer, 1985). To explore the origin of this saturation, aqueous mixtures were prepared in 2% (w/v) glycerol increments. An aerosol spray of each mixture deposited drops with a range of sizes onto the bottom of a cup made from 25 μm copper foil. The cup plus drops was then plunged into liquid nitrogen and the result photographed through a microscope. As in previous work (Garman & Schneider, 1997; McFerrin & Snell, 2002; Chinte et al., 2005; Berejnov et al., 2006), clear drops were judged to be vitrified, while opaque drops were judged to be polycrystalline. The largest drop volume for which the drops were consistently transparent was then

recorded as the critical volume for vitrification at that glycerol concentration. Drop volumes were estimated based on the drop radius and separate calibration measurements of drop height versus radius on copper foil.

Copper's thermal conductivity is much larger than that of the boiling gas layer that envelops drops when they are directly plunged into liquid cryogens. This fact is used to advantage in the splat freezing method (in which drops are sprayed onto cold metals) to vitrify ~10 μm drops of pure water (Mayer, 1985). Our variant of this method yields frozen drops with much simpler shapes, allowing more accurate volume estimation. As shown by the solid circles in Figure 2.1, the saturation of critical concentration at small drop volumes disappears, and the concentration decreases monotonically (approximately logarithmically) with volume down to the smallest volume (~40 pl) studied. For large volumes, data from the two methods almost agree, with the points from copper foil being slightly higher. This is most likely due to the added mass of copper that must also cool.

2.2.2 The cold gas layer: Temperature versus height above the liquid cryogen

The gas immediately above a liquid cryogen will be cooled through radiation, convection and conduction by the cold liquid below. For large sample volumes, the sample can pass through the resulting cold gas layer without appreciable internal temperature drop, so that cooling occurs mainly in the liquid cryogen. For small sample volumes, the sample will remain in equilibrium with the surrounding gas as it passes through the cold gas layer. Most of the cooling as well as solidification of the solvent within the sample (vitrification or crystallization) may then occur in the gas, before the sample reaches the liquid. The dangers of cold gas layers have been

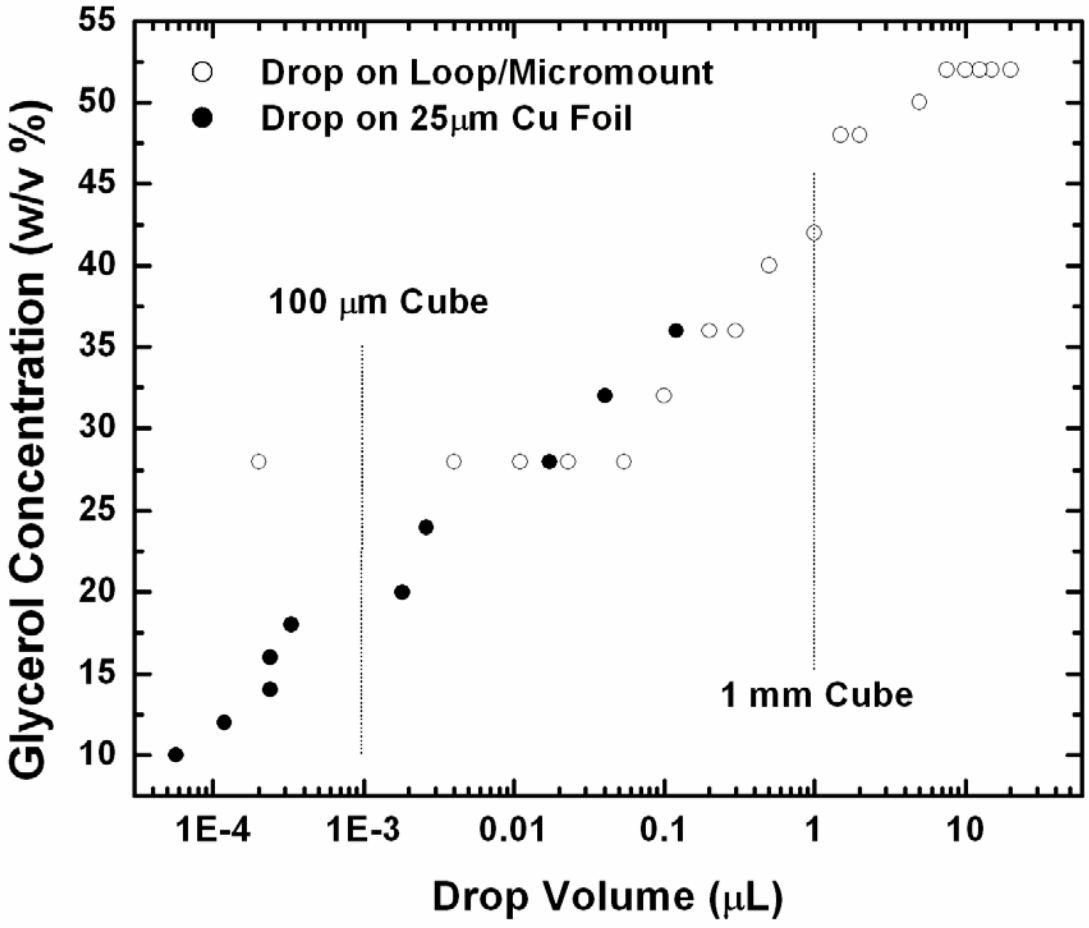

Figure 2.1

Minimum glycerol concentration required for vitrification of glycerol-water mixtures versus drop volume. Open circles are data collected by plunging drops held in tungsten wire loops (for volumes above 1 μl) or in MicroMounts (below 1 μl) into liquid nitrogen, from Berejnov et al. (2006). Solid circles represent data collected by spraying drops onto the bottom of a 25 μm thick copper cup and then plunging into liquid nitrogen. Vertical lines indicate corresponding linear dimensions of cubic samples.

discussed in the context of cryo-electron microscopy (Ryan et al., 1992), and the problem of heat transfer from a small drop moving through the cold gas above a liquid cryogen has been analyzed (Chang & Baust, 1991). In the protein crystallography community, the cold gas layer's existence has been recognized (Pflugrath, 2004) but its effects have not been quantified.

To quantify the cold gas layer, a glass hemispherical dewar 12 cm across and 8 cm deep (Pope Scientific Inc, Saukville, WI, USA) was filled with liquid nitrogen at T=77 K. The temperature of the gas above the liquid was measured using a chromel-constantan (E-type) bare-wire thermocouple with a 120 μm bead and 75 μm diameter leads, and recorded using a computer with an SCB-386 DAQ interface and running LabView. The thermocouple was initially positioned well above the liquid nitrogen surface and then lowered by a stepper motor under computer control. The recorded temperature vs. time was converted to temperature vs. height using the measured speed of the stepper motor. To check for, e.g., radiative cooling of the thermocouple below the gas temperature, measurements were repeated at speeds from 0.1 mm/s to 5 mm/s and in the reverse direction, and no appreciable variation in temperature profiles was observed. To emulate conditions used by crystallographers, no special effort was made to isolate the dewar, and so air currents in the room randomly perturbed the gas layer. Measurements were thus repeated until a satisfactorily clean curve was obtained. Temperature versus height profiles were recorded at different radial distances from the dewar's center, and showed no measurable variations from the center to the inner walls.

Figure 2.2 shows the resulting temperature profiles obtained when the dewar was filled to its brim and to levels 2 and 4 cm below its brim. With the dewar filled to the

brim, the gas temperature falls below water's freezing point 1 cm above the surface, and below water's glass transition T_g about 4 mm above the surface. For a more typical and safe fill level of 4 cm, the cold gas layer extends more than 2 cm above the liquid surface, and the temperature drops below T_g nearly 1 cm above the liquid surface.

2.2.3 Plunging through cold gas

We next investigated cooling rates obtained when plunging a thermocouple through the cold gas layer into liquid nitrogen, as a function of the layer thickness (dewar fill level) and plunge velocity. To obtain the fastest temperature response time, a thermocouple with an 80 μm bead and 25 μm diameter leads was flattened between two machine-tool bits to a thickness of 20 μm. This allowed us to explore the thermal mass/response time regime relevant to cryocooling sub-100 μm protein crystals. Our geometry is particularly relevant to crystals with thin plate or rod-like morphologies. The thermocouple was plunged by hand, and the plunge velocity was determined using frame-by-frame analysis of a video of the experiment.

Figure 2.3 shows the temperature of the thermocouple during plunges into liquid nitrogen at different plunge velocities. In (a), the dewar was filled to 4 cm from its brim, and in (b) it was filled to the brim. Arrows on each curve indicate the point at which the thermocouple entered the liquid nitrogen. For all conditions studied, the thermocouple cools within the gas layer below water's freezing point, and below water's homogeneous nucleation temperature (233 K) for all but the fastest plunge into a full dewar. For conditions most closely matching those used in typical cryocrystallography practice — a dewar filled 4 cm below the brim and a plunge

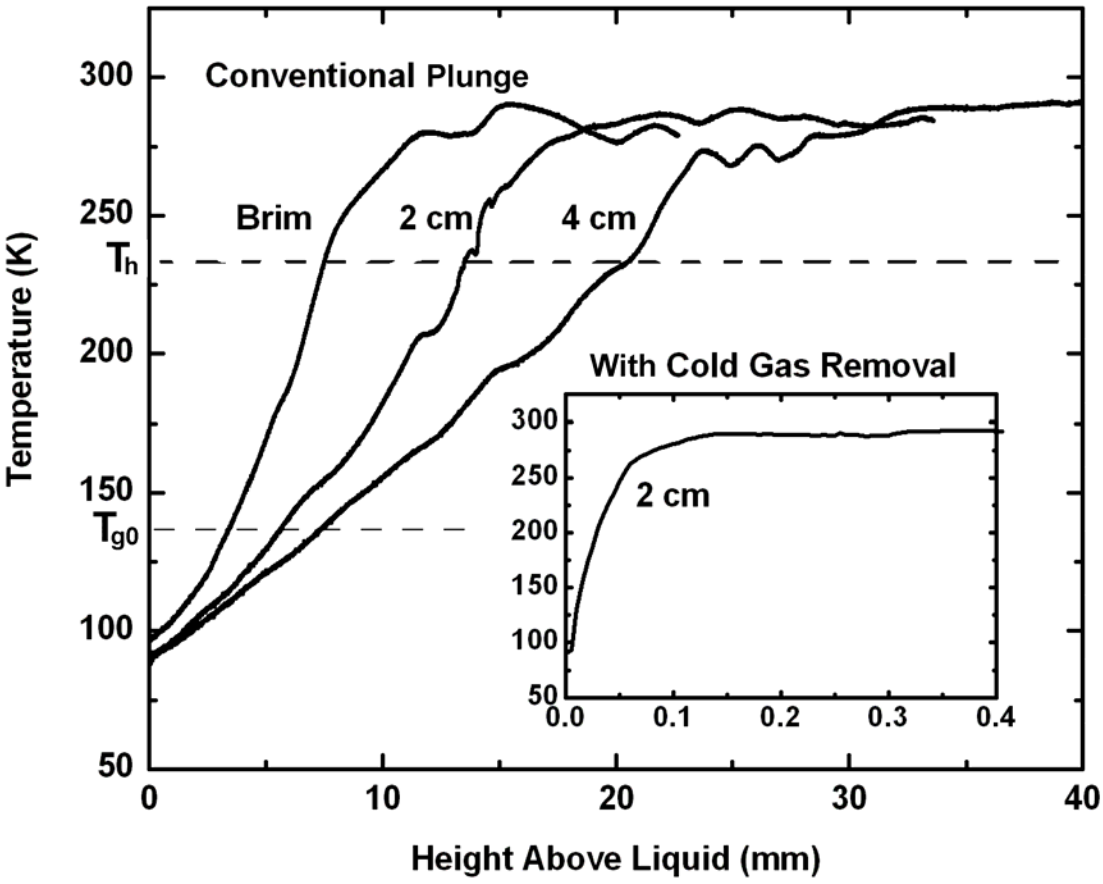

Figure 2.2

Gas temperature as a function of height above liquid nitrogen held in a 12 cm diameter hemispherical dewar, for different liquid fill levels (measured in cm from the brim). Fluctuations at large height are due to room air currents. Inset: Gas temperature versus height above liquid nitrogen when dry nitrogen gas is blown along the thermocouple's path, as described in the text. Blowing reduces the thickness of the cold gas layer above the liquid from ~2 cm to less than 100 μm, a reduction of more than two orders of magnitude.

speed of 0.4 m/s — the thermocouple cools below Tg within the gas layer. The time required is ~0.1 s, corresponding to a cooling rate of 1500 K/s. This is only three times larger than reported by Teng & Moffat (1998), despite our use of a thermocouple six times thinner and with leads six times smaller in diameter.

The maximum cooling rate prior to entering the liquid increases roughly linearly with increasing plunge velocity. Once the thermocouple enters the liquid, the cooling rate in all cases is much larger (~15,000 K/s). Unlike in the gas, cooling rates in liquid are largely unaffected by the plunge velocity in the velocity range examined.

One way to defeat the cold gas layer is to plunge at high velocity (>5 m/s) into a full dewar. High speed plunging is used in commercial devices for cooling electron microscopy samples, which are comprised of very thin (sub-micron) films mounted on thick (20-30 μm) metal grids that have much higher thermal mass than protein crystallography mounts. It is not clear that the more delicate samples and mounts used in protein crystallography could routinely survive such treatment, except when the sample thickness and thus the force on entering the liquid is small. Large accelerations and decelerations (>100 times that due to gravity), required for a compact device and to prevent enormous splashing when the goniometer base holding the sample impacts the liquid cryogen, could also be problematic.

2.2.4 Removing the cold gas layer

Another way to increase cooling rates is to remove the cold gas layer, producing an abrupt transition along the plunge path from gas at room temperature to liquid at cryogenic temperature. To remove the cold gas layer, we simply blow it away.

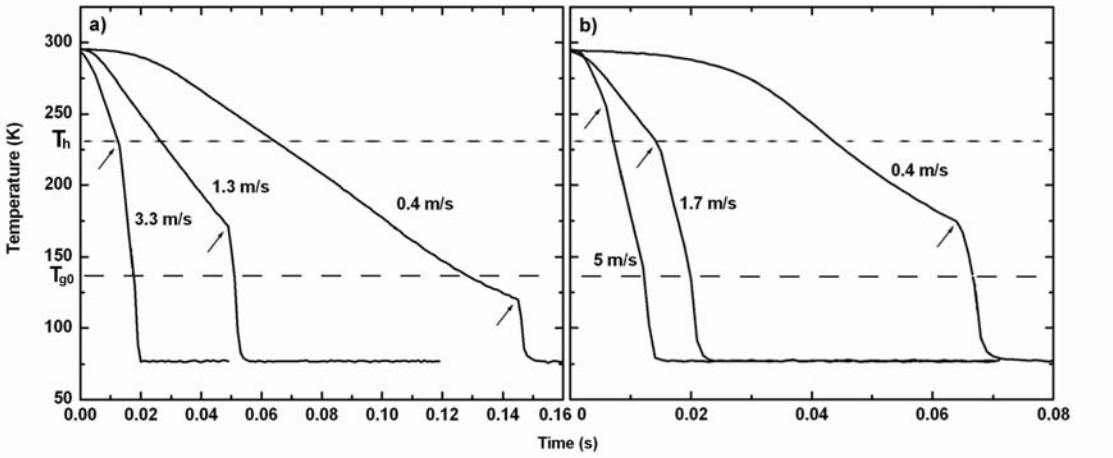

Figure 2.3

Temperature versus time recorded as a thermocouple is plunged at different velocities into a dewar of liquid nitrogen. The liquid level is (a) 4 cm from the brim and (b) at the brim. Arrows indicate the time the thermocouple enters the liquid. Measurements used a chromel-constantan bare-wire thermocouple with 25 μm leads and a flattened, ~20 μm thick bead (see text.)

A Teflon nozzle with a diameter of 8 millimeters was connected to a cylinder of dry nitrogen gas through a high flow-rate rotameter. The nozzle was positioned 30 cm from the liquid level and tipped 10 degrees from the vertical, and its flow directed at the radial center of the liquid surface. Other geometries for the nozzle and its positioning were examined and most were found to be satisfactory, but the geometry described here gave the most repeatable results.

The inset to Figure 2.2 shows the dramatic effect of blowing on the temperature profile. Nitrogen gas flowing at 20 liters per minute, corresponding to a maximum velocity at the nozzle of ~6.6 m/s, was directed at the liquid nitrogen surface in a dewar filled to within 2 cm of its brim. The temperature falls below water's melting point at a height of ~80 μm above the liquid surface, and below water's glass transition at ~20 μm, a height comparable to the thickness of the thermocouple bead used to measure the profile. Our simple blowing procedure thus reduces the gas layer thickness by a factor of at least 300. At a modest plunge velocity of 0.4 m/s, the time to traverse this layer can be calculated to be less than 0.2 ms, more than 500 times shorter than the cooling times without gas layer removal in Figure 2.3. Consequently, nearly all the cooling during a plunge should occur in the liquid, not the gas.

2.2.5 Cooling rates with cold gas layer removal

To test the effect of cold gas layer removal on cooling rates, samples were plunged in the presence of flowing nitrogen gas. The gas flow was turned on prior to the plunge and then turned off just after the sample was beneath the liquid surface so as to minimize nitrogen boil-off. (For liquid propane and ethane, flowing gas can warm the liquid layers near the surface above T_g, so minimizing the time the gas is on is even more important.) Figure 2.4 shows the resulting temperature profile obtained with a 20

liter per minute gas flow when the thermocouple was plunged at 0.3 m/s along the axis of a dewar filled to within 2 cm of its brim. Unlike in all of the data of Figure 2.3, there is no evidence of cooling by the gas; all cooling occurs in the liquid nitrogen. The cooling time from room temperature to below Tg is ~0.01 s, 10 times shorter than without gas removal. The average cooling rate over this temperature range is 15,000 K/s, 10 times larger than without gas layer removal, and it is slightly larger than the cooling rate achieved without gas removal at a plunge velocity of 5 m/s into a full dewar. Very similar temperature-time curves are obtained for plunge velocities from 0.01 m/s to 1 m/s and flow rates from 10 to 60 LPM, with only a slight increase in liquid cooling rate for larger plunge velocities. This is a significant advantage of cold gas layer removal: very large cooling rates are achieved even with very leisurely plunges that pose no risk to the sample.

In every temperature history shown in Figures 2.3 and 2.4 in which the thermocouple enters the liquid with a temperature well above 150 K, (i.e., with blowing or high plunge velocities), there is a transition to a higher cooling rate at 130-150 K. This is due to a change from film boiling to nucleate boiling of the nitrogen near the sample surface (Incropera & DeWitt, 2002). In the film boiling regime, the cooling rate within the liquid increases slightly with increasing plunge velocity (roughly 30% for a factor 15 in velocity). A similar very weak dependence of cooling rate on plunge velocity is observed in liquid propane and ethane, which cool only in the nucleate boiling regime (Ryan et al., 1992).

2.2.6 Tiny cryoprotectant concentrations for tiny samples

Finally, we return to the experiments of Berejnov et al. (2006) on the minimum (critical) cryoprotectant concentration required to achieve vitreous ice as a function of sample volume. Glycerol-water drops mounted on MicroMounts (Mitegen, Ithaca, NY) and ranging in size from 1 μl down to 100 pl were plunge cooled into liquid nitrogen, using the set-up described in Section 2.2.4 to remove the cold gas layer. The state of the drop (vitreous or polycrystalline) after plunge cooling was deduced by visual observation through a microscope, as described by Berejnov et al. The results are shown in Figure 2.5, along with those of Berejnov et al. obtained without cold gas removal. The small volume saturation of critical concentration is removed, and glycerol concentrations decrease monotonically with drop volume down to the smallest drop examined. At all volumes studied, the required concentrations are somewhat lower than for drops cooled on copper foil (Figure 2.1). For a 100 pl drop, corresponding to a 60 μm diameter sample, the required glycerol concentration is reduced from 28% w/v without blowing to 6% w/v. The point for vitrification of pure water (0% glycerol) at a volume of ~4 pl was measured by Mayer (Mayer, 1985) using splat freezing on cold copper. If the extrapolation of the fit to our data in Figure 2.5 is valid, then plunging into liquid nitrogen with cold gas removal should cool small samples as effectively as splat freezing, the standard method for achieving the highest cooling rates.

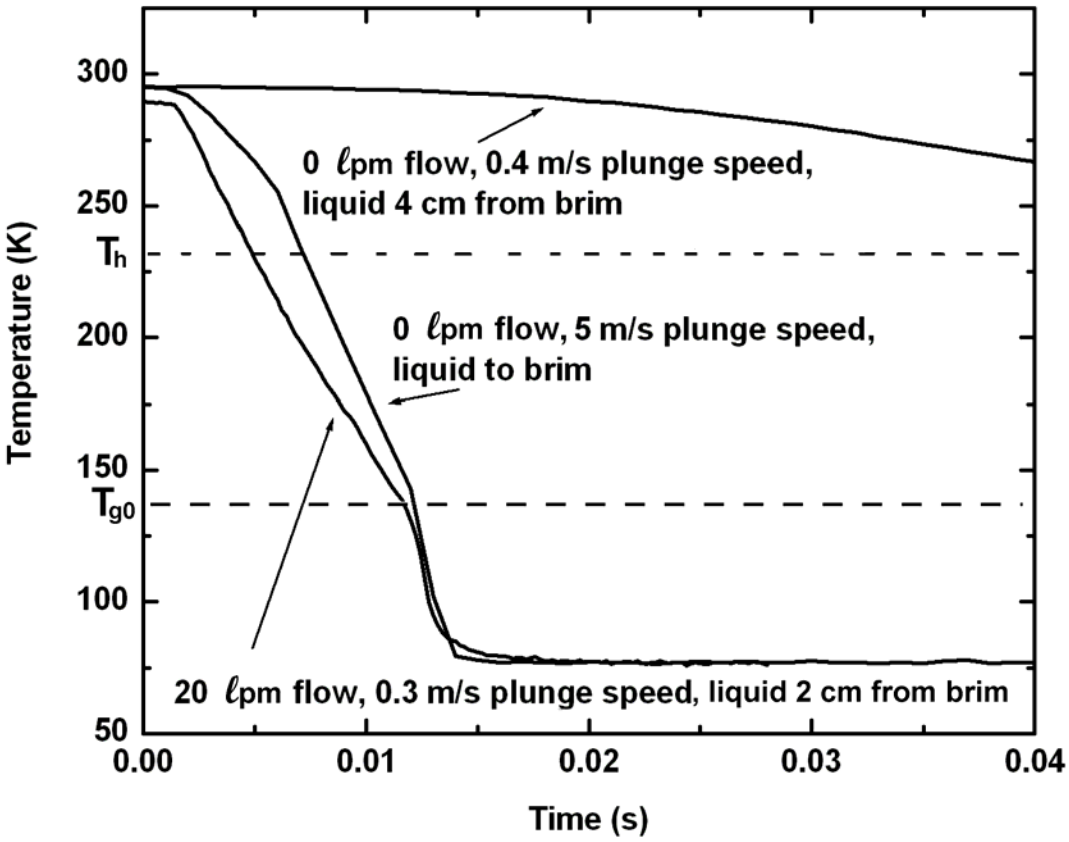

Figure 2.4

Temperature versus time recorded as a thermocouple is plunged into liquid nitrogen, with and without cold gas layer removal by blowing. Without blowing, the plunge velocity required to minimize the effect of the gas layer is ~5 m/s. With blowing, very similar curves are obtained for all plunge velocities and fill heights. These measurements used the same thermocouple as in Figure 2.3.

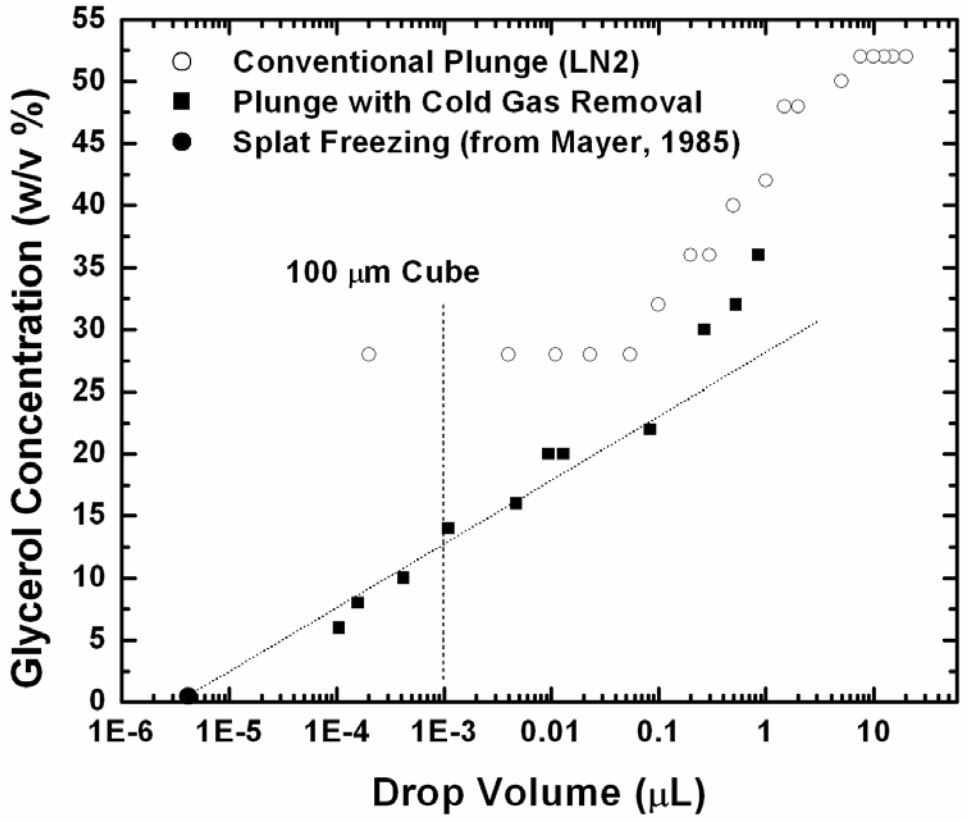

Figure 2.5

Minimum glycerol concentration required for vitrification of glycerol-water mixtures versus drop volume. Open circles are the data of Figure 1 for a direct plunge into liquid nitrogen without cold gas layer removal, taken from Berejnov et al. (2006). Solid squares are data collected for a direct plunge into liquid nitrogen using a dry nitrogen gas stream to remove the cold gas layer. These data show an approximate logarithmic variation of concentration with volume over four orders of magnitude in volume (suggesting an exponential variation of critical cooling rate with concentration.) Extrapolating this variation to zero concentration roughly yields the maximum volume of pure water that can be vitrified by spraying drops onto cold copper surfaces.

2.3 Discussion

2.3.1 Two limiting approaches to cryopreservation

One can imagine two limiting approaches to cryopreservation. The first is to cool very slowly (e.g., 0.1 K/s) through the vitrification point, using large cryoprotectant concentrations (e.g., 60% w/v glycerol) to prevent crystallization. Since all physico-chemical properties are temperature dependent, this might allow relaxations and redistributions to occur so as to maintain quasi-equilibrium and achieve a homogeneous low temperature state. Variants on this approach have been used for cryopreservation of cells and tissues (Mazur, 1970), but in most cases it is impractical for protein crystals.

The other limiting approach is to cool so quickly that the high temperature state is frozen in. This approach is loosely referred to as hyperquenching, and is typically achieved by splat cooling on cold metals (Mayer, 1985; Johari et al., 1987).

Unfortunately, cooling rates achieved in cryopreservation of protein crystals by plunge or gas stream cooling are 10^3 K/s or less (Teng & Moffat, 1998; Walker et al., 1998), too fast to allow gentle relaxations, and yet too slow to be in the hyperquenching regime. Although sufficiently fast to produce full solvent vitrification (with sufficient cryoprotectant), these modest cooling rates produce inhomogeneities within the crystal (evident in X-ray topography and in measurements of lattice constant distributions) that correlate with degradation of mosaicity and resolution (Kriminski et al., 2002). These inhomogeneities are due at least in part to incomplete relaxation of stresses associated with differential thermal expansion of solvent and protein that can occur at

modest cooling rates (Juers & Matthews, 2001; Kriminski et al., 2002). Although most conformational flexibility is thought to be frozen out by T=220 K, with current methods the time to cool to this temperature can be of the order of 0.1 s. This is sufficiently long to allow side chains (perhaps including those in the active site of a protein) to undergo important conformational changes (Deacon et al., 1997; Scheidig et al., 1999; Sandalova et al., 1999).

2.3.2 Cold gas layer removal as a route to hyperquenching

Our experiments show that cooling rates of protein crystals can be increased by at least a factor of 10-20 over current best practice — to greater than 15,000 K/s in liquid nitrogen — by removing the cold gas layer above the liquid. The cooling rate should vary roughly as the square root of crystal volume (consistent with the data in Figure 2.5 and more detailed analysis in Berejnov et al. (2006)). Using ~10 μm microcrystals and liquid propane or ethane, cooling rates approaching 100,000 K/s should be achievable. The apparatus required to achieve these large improvements over current practice is trivial.

2.3.3 Puzzles resolved

The presence of the cold gas layer explains the saturation of minimum cryoprotectant concentrations required to achieve vitreous ice at volumes below ~0.1 μl, observed for plunge cooling in both liquid nitrogen and liquid propane (Berejnov et al., 2006). For essentially the entire range of sample sizes of relevance in protein crystallography and for experimentally convenient plunge velocities, much of the cooling occurs in the cold gas layer, not the liquid. The fact that the cryoprotectant concentration is roughly

volume independent (rather than just showing a change in slope) for volumes below 0.1 μl suggests that these volumes remain in quasi-equilibrium with the surrounding gas during the plunge. For the same plunge velocity and cold gas layer thickness, they all then cool at the same rate, and so require the same cryoprotectant concentration. Cooling in the cold gas layer may in part explain why flash cooling outcomes for samples prepared and cooled in seemingly similar ways can be so variable. That one good crystal may have been plunged as a lab mate walked by, blowing away the cold gas.

Cooling in the cold gas layer explains why plunge cooling in liquid cryogens has so far not proven to be reliably superior to cooling in cold gas streams. In all cases, cooling rates have been limited by heat transfer to a gas, not to a liquid.

2.3.4 Implications for macromolecular crystallography

The present results, by allowing implementation of highly reproducible cooling protocols with dramatically increased cooling rates, will have broad consequences for macromolecular crystallography. Increased cooling rates will reduce conformational changes between room and low temperature structures. They will reduce the relaxations that occur during slow cooling and that give rise to inhomogeneities responsible for mosaic broadening and resolution degradation. They will dramatically reduce — by a factor of 4 or 5 — the cryoprotectant concentrations required to prevent formation of crystalline ice in protein-free solution that may surround the crystal, simplifying the search for cryoprotection conditions. And because the high protein concentrations within the crystal provide excellent protection against ice crystallization (Kriminski et al., 2002), it may routinely be possible to go from

crystallization tray to liquid cryogen to X-ray beam and obtain useable diffraction with no cryoprotectants, for all but the highest solvent-content crystals. Cryoprotectants play other roles aside from inhibiting ice crystallization (Juers & Matthews, 2001; Kriminski et al., 2002), and so they may still be required to obtain the best resolution.

2.4 Conclusion

Cooling protein crystals by plunging into liquid cryogens has been powerfully enabling and annoyingly troublesome, dramatically reducing radiation damage while introducing other damage that limits the quality of X-ray determined structures. It has long been evident that there is a cold gas layer above the liquid cryogen, and that this gas layer can cool a sample that passes through it. What has not been evident is that, for sample sizes spanning essentially the entire range of interest in protein crystallography, most cooling occurs in this gas layer, not in the liquid cryogen. This unfortunate coincidence has limited cooling rates, allowing internal relaxations that disrupt crystal order. By banishing the cold gas layer, the full potential of plunge cooling to capture and preserve protein structure may finally be realized.

REFERENCES

Berejnov, V., Husseini, N. S., Alsaied, O. A., & Thorne, R. E. (2006). *Journal of Applied Crystallography* **39**, 244-251.

Bruggeller, P. & Mayer, E. (1980). *Nature* **288**, 569-571.

Chang, Z. H. & Baust, J. G. (1991). *Journal of Microscopy-Oxford* **161**, 435-444.

Chayen, N. E., Boggon, T. J., Cassetta, A., Deacon, A., Gleichmann, T., Habash, J., Harrop, S. J., Helliwell, J. R., Nieh, Y. P., Peterson, M. R., Raftery, J., Snell, E. H., Hadener, A., Niemann, A. C., Siddons, D. P., Stojanoff, V., Thompson, A. W., Ursby, T., & Wulff, M. (1996). *Quarterly Reviews of Biophysics* **29**, 227-278.

Chinte, U., Shah, B., DeWitt, K., Kirschbaum, K., Pinkerton, A. A., & Schall, C. (2005). *Journal of Applied Crystallography* **38**, 412-419.

Deacon, A., Gleichmann, T., Kalb, A. J., Price, H., Raftery, J., Bradbrook, G., Yariv, J., & Helliwell, J. R. (1997). *Journal of the Chemical Society-Faraday Transactions* **93**, 4305-4312.

Dubochet, J., Lepault, J., Freeman, R., Berriman, J. A., & Homo, J. C. (1982). *Journal of Microscopy-Oxford* **128**, 219-237.

Frauenfelder, H., Petsko, G. A., & Tsernoglou, D. (1979). *Nature* **280**, 558-563.

Garman, E. (1999). *Acta Crystallographica Section D-Biological Crystallography* **55**, 1641-1653.

Garman, E. F. & Schneider, T. R. (1997). *Journal of Applied Crystallography* **30**, 211-237.

Garman, E. F. & Owen, R. L. (2006). *Acta Crystallogr. D. Biol. Crystallogr.* **62**, 32-47.

Halle, B. (2004). *Proceedings of the National Academy of Sciences of the United States of America* **101**, 4793-4798.

Hope, H. (1988). *Acta Crystallographica Section B-Structural Science* **44**, 22-26.

Hope, H. (1990). *Annual Review of Biophysics and Biophysical Chemistry* **19**, 107-126.

Incropera, F. P. & DeWitt, D. P. (2002). *Fundamentals of heat and mass transfer*, 5th ed ed. New York: J. Wiley.

Johari, G. P., Hallbrucker, A., & Mayer, E. (1987). *Nature* **330**, 552-553.

Juers, D. H. & Matthews, B. W. (2001). *Journal of Molecular Biology* **311**, 851-862.

Juers, D. H. & Matthews, B. W. (2004). *Quarterly Reviews of Biophysics* **37**, 105-119.

Kriminski, S., Caylor, C. L., Nonato, M. C., Finkelstein, K. D., & Thorne, R. E. (2002). *Acta Crystallogr. D. Biol. Crystallogr.* **58**, 459-471.

Kriminski, S., Kazmierczak, M., & Thorne, R. E. (2003). *Acta Crystallographica Section D-Biological Crystallography* **59**, 697-708.

Lu, Z. P. & Liu, C. T. (2003). *Phys. Rev. Lett.* **91**, 115505.

Mayer, E. (1985). *Journal of Applied Physics* **58**, 663-667.

Mazur, P. (1970). *Science* **168**, 939-&.

McFerrin, M. B. & Snell, E. H. (2002). *Journal of Applied Crystallography* **35**, 538-545.

Peyridieu, J. F., Baudot, A., Boutron, P., Mazuer, J., Odin, J., Ray, A., Chapelier, E., Payen, E., & Descotes, J. L. (1996). *Cryobiology* **33**, 436-446.

Pflugrath, J. W. (2004). *Methods* **34**, 415-423.

Rodgers, D. W. (1994). *Structure* **2**, 1135-1140.

Ryan, K. P., Bald, W. B., Neumann, K., Simonsberger, P., Purse, D. H., & Nicholson, D. N. (1990). *Journal of Microscopy-Oxford* **158**, 365-378.

Ryan, K. P. (1992). *Scanning Microscopy* **6**, 715-743.

Sandalova, T., Schneider, G., Kack, H., & Lindqvist, Y. (1999). *Acta Crystallographica Section D-Biological Crystallography* **55**, 610-624.

Scheidig, A. J., Burmester, C., & Goody, R. S. (1999). *Structure* **7**, 1311-1324.

Snell, E. H., Judge, R. A., Larson, M., & van der Woerd, M. J. (2002). *Journal of Synchrotron Radiation* **9**, 361-367.

Teng, T. Y. & Moffat, K. (1998). *Journal of Applied Crystallography* **31**, 252-257.

Tilton, R. F., Dewan, J. C., & Petsko, G. A. (1992). *Biochemistry* **31**, 2469-2481.

Walker, L. J., Moreno, P. O., & Hope, H. (1998). *Journal of Applied Crystallography* **31**, 954-956.

Weik, M., Kryger, G., Schreurs, A. M. M., Bouma, B., Silman, I., Sussman, J. L., Gros, P., & Kroon, J. (2001). *Acta Crystallographica Section D-Biological Crystallography* **57**, 566-573.

Weik, M., Vernede, X., Royant, A., & Bourgeois, D. (2004). *Biophysical Journal* **86**, 3176-3185.

Weik, M., Schreurs, A. M. M., Leiros, H. K. S., Zaccai, G., Ravelli, R. B. G., & Gros, P. (2005). *Journal of Synchrotron Radiation* **12**, 310-317.

Zeitler, E. (1982). *Journal of Ultrastructure Research* **81**, 397.

CHAPTER 3

SCHLIEREN IMAGING OF A COLD GAS STREAM FOR CRYOCRYSTALLOGRAPHY

3.1 Introduction

Protein X-ray crystallography is performed at 100 K in nearly every case. This is because low temperatures mitigate radiation damage and allow for easy transportation and storage of samples (Rodgers, 1994; Garman & Schneider; 1997). One important step in this process is the placement of the sample holder onto the goniometer, whether this is done manually or with an automatic mounting system (Parkin & Hope, 1998; Pflugrath, 2004). This step is non-trivial because the sample must be transferred from under liquid nitrogen to a stream of cold gas without significant warming.

As the typical experimental setup moves toward larger X-ray flux and a smaller beam, the crystal size required to obtain a complete dataset is reduced, and complete data has been obtained from crystals on the order of 10 μm on a side (Sanishvili *et al*., 2008). As the size of the sample is reduced, it responds to changes in its thermal environment increasingly rapidly. This is one reason to expect that unintentional annealing during mounting would be more of a problem in recent work utilizing smaller crystals.

One previous study has examined the mounting process using tongs (Parkin & Hope, 1998). This study found that no measurable annealing occurred, but the thermocouple used in the study lacked the sensitivity required for comparison with tiny samples used in modern experiments.

This paper explores the importance of crystal size when transferring the crystal to the goniometer. We find that for samples smaller than 80 μm, large temperature spikes can be expected to occur randomly and unacceptably frequently. It has been reported that in some cases annealing crystals briefly can improve diffraction quality, but this is only done when diffraction is poor to begin with (Harp *et al*., 1998; Harp *et al*., 1999; Stevenson *et al*., 2001; Hanson *et al*., 2003). Furthermore, successive annealing trials and extended annealing times on a single crystal have been shown to eventually degrade the crystal perfection. (Kriminski *et* al., 2002; Hanson *et al.,* 2003; Juers & Matthews, 2004). A temperature spike to ~ 240 K can allow for the formation of crystalline ice in the sample as it cools again at a significantly lower rate than it originally did in the liquid nitrogen. Also a random and uncontrollable amount of annealing in the process of mounting will cause additional variability in cryocooling outcomes that are already unpredictable.

To further understand the source of the temperature spikes, we use a schlieren technique to produce a video of the motions of the gas surrounding the crystal during mounting. These videos show that the gas is turbulent during the process of mounting, partly explaining the variability in thermal histories.

3.2 Experiment

The experiments were carried out on an Oxford Cryosystems 700 Series Cryostream (Oxford Cryosystems, Oxford, UK). A warm, dry gas stream surrounds the cold stream so that humid ambient air is never in contact with the gold gas. Otherwise ice would slowly build up on the nozzle or the crystal. The velocities of the two gases must be matched so that the flow is laminar past the sample position. The flow rate

ranges from 5 to 10 liters per minute (of cold gas), so that the velocity is 4 to 8 m/s through the 5 mm diameter nozzle. The cold gas stream is positioned so that the sample position is on the axis of the nozzle, 5 mm from the opening. A schematic of the cryostream and sample is shown in Figure 3.1.

A previously-cooled crystal will already be mounted on a crystal mount, glued into a goniometer base (Mitegen, Ithaca, NY, USA). A plastic cap is typically either screwed, or held magnetically over the base and mount. In order to mount the crystal, the cap was held with forceps and the vial/cap was withdrawn from the storage dewar. It was then tipped horizontally, at which point any liquid nitrogen remaining in the cap spilled out as the base was attached to the goniometer head. The cap was then detached from the base and pulled away to expose the crystal to the cold gas stream. During this final motion, there was no longer any liquid nitrogen in contact with the sample, but the gas stream had yet to settle over it and reach steady state. This allowed for the annealing due to warm gas entrained by the turbulent flow as the cap is removed.

3.2.1 Imaging

Schleiren imaging allows for the visualization of temperature (or pressure) variations in a transparent medium. A schematic of the system is shown in Figure 3.2. Light emerges from a point source at A, and is collimated by a mirror at B. Parallel rays travel across the imaging area at C, to a second mirror at D. The image of the point light source is focused at E, onto the edge of a razor blade. A camera at F focuses on

the imaging area through the mirror at D, but half of the light coming from the image

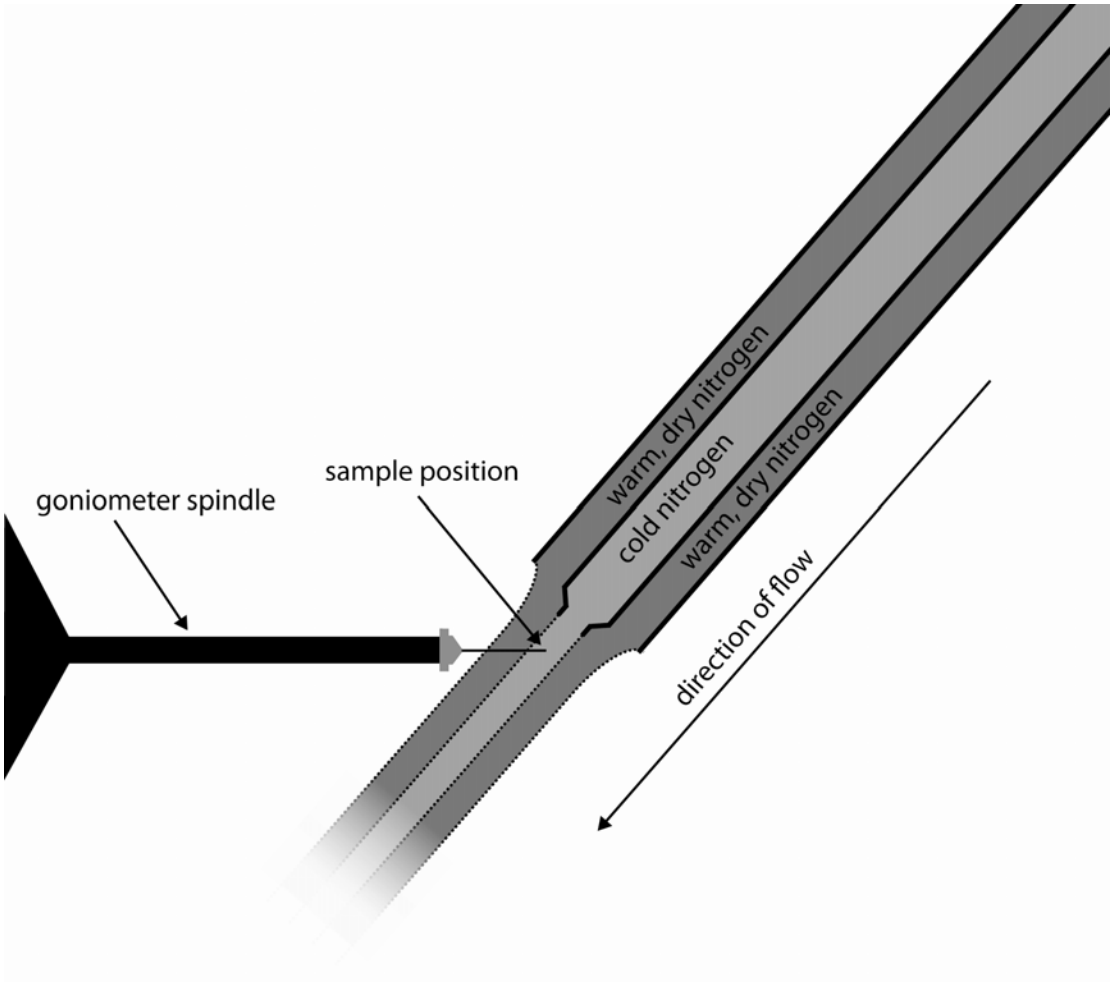

Figure 3.1

A schematic representation of the cryostream is shown. Cold (typically 100 K) nitrogen gas (light gray) flows out of the end of the cryostream nozzle (thick lines) while ambient-temperature nitrogen gas flows out of a sheath surrounding the nozzle. There is a region of laminar flow that extends past the nozzle, and the sample is positioned in the cold gas in this region.

area is blocked out by the razor blade. This filtering gives rise to contrast variations because regions of varying refractive index deflect the light either onto or away from the razor blade.

For our experiments, the light source was a 150 W Schott Fostec Ace (Schott, Southbridge, MA, USA), covered with aluminum foil, with a 50 um hole in the foil. The mirrors were 114 mm diameter, f/8, with a surface accuracy of 1/8 wave from www.e-scopes.cc. A goniometer head and Cryostream were positioned in the imaging area, and the images were recorded with a digital camera.

3.2.2 Thermal histories

To record the temperature at the sample position during mounting, a thermocouple with a very small bead was placed there. Since goniometer bases and mounts are metallic, the thermocouple leads were coated with non-conductive glue. The glue was applied so as not to increase the size (and thermal mass) of the thermocouple bead.

A chrome-constantan thermocouple from Omega Engineering (catalog number CHCO-001) was connected to Labview (www.ni.com/labview) through a 6025e PCI DAQ interface (National Instruments, www.ni.com), and positioned on a base, inside a vial, as though it was a previously frozen crystal. Several mounting trials were then carried out as the temperature was recorded.

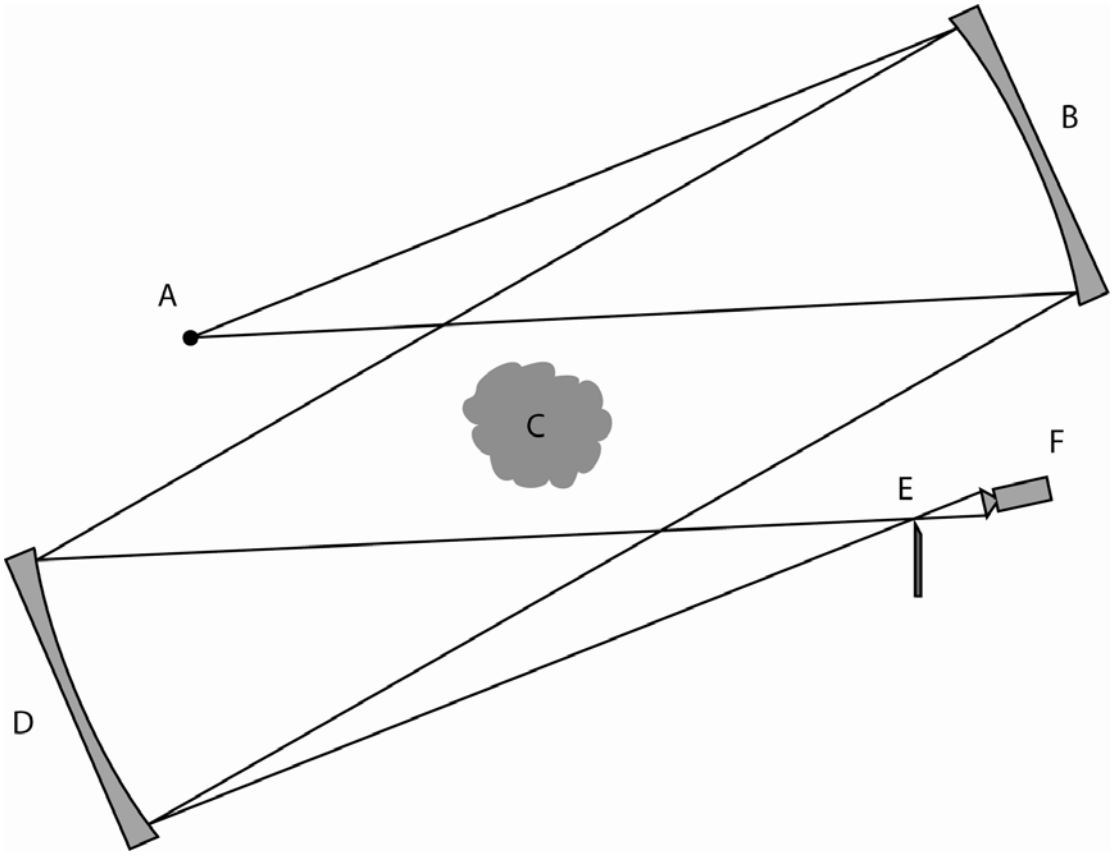

Figure 3.2

A schematic representation of the apparatus used in schlieren imaging. Light from a point source (A) is collimated and then refocused by two mirrors (B and D). A razor blade (E) is positioned at the focus. A small refractive index variation in the imaging area (C) will produce a deflection in the path of the light so that it is blocked either more or less by the razor blade, giving sharp contrast to the image recorded by the camera (F). Note that the camera has a separate lens system (not shown) focused on the imaging area (C).

3.2.3 Images

In Figure 3.3a, we show a schlieren image of the cryostream operating under normal conditions. The goniometer head can be seen with no base attached. The interface between the cold and warm streams from the cryostream can be clearly seen, however the interface between the warm, dry gas from the cryostream and the ambient air in the lab is invisible because it does not present enough of a refractive index mismatch. Figure 3.3b is an analogous image with a base and mount attached to the goniometer head.

In Figure 3.4, we show a typical set of frames from the process of mounting. We focus on the stage of withdrawing the cap from the base. We note that there is significant mixing of warm and cold gas, even at the sample position. Due to the turbulent nature of the process, we expect the thermal history of the sample during mounting to be highly variable.

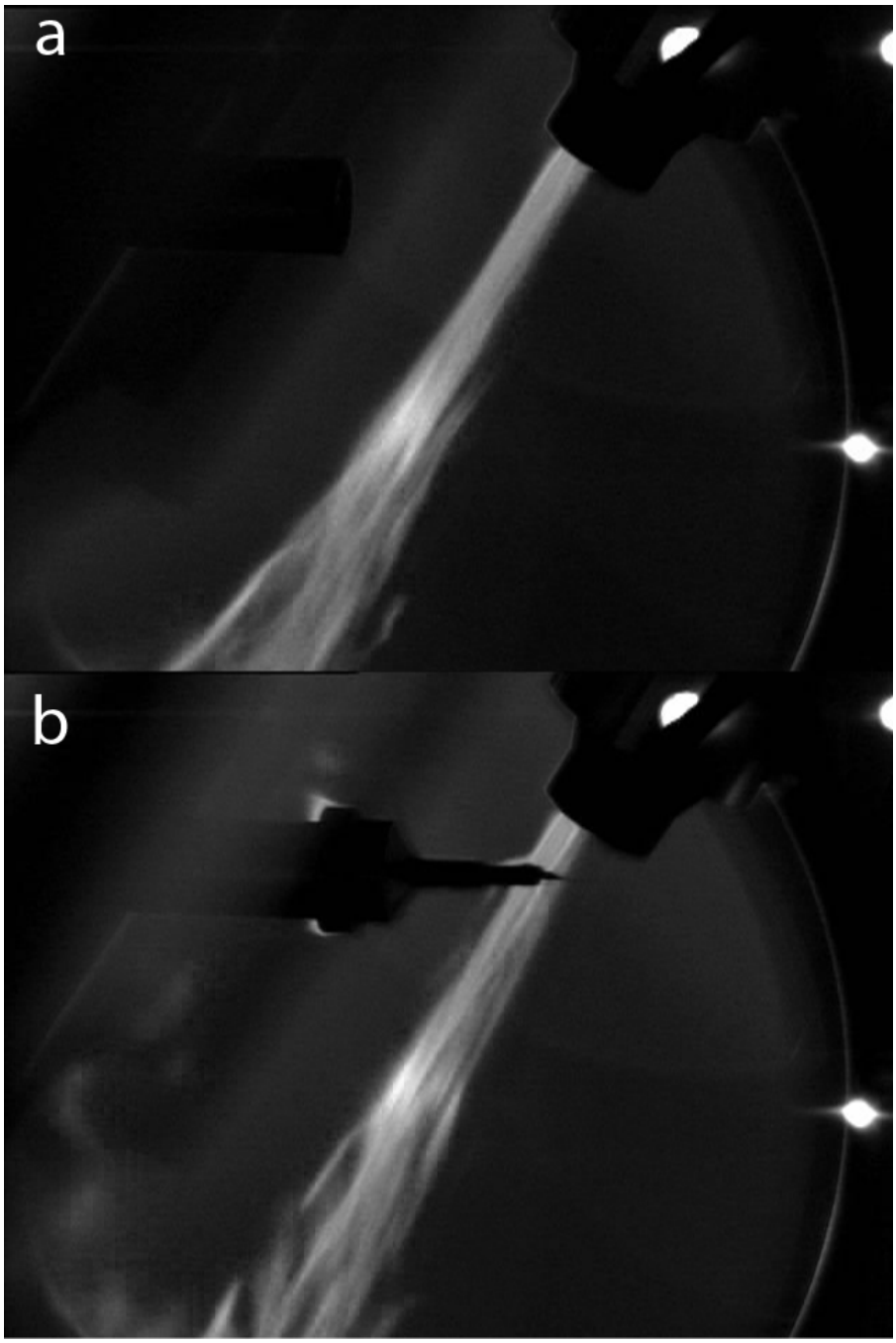

Figure 3.3

Schlieren images of the cryostream in operation. The goniometer spindle is visible in a), and a base + mount can be seen attached to the spindle in b. It is evident that the base + mount does not disturb the flow appreciably in steady state.

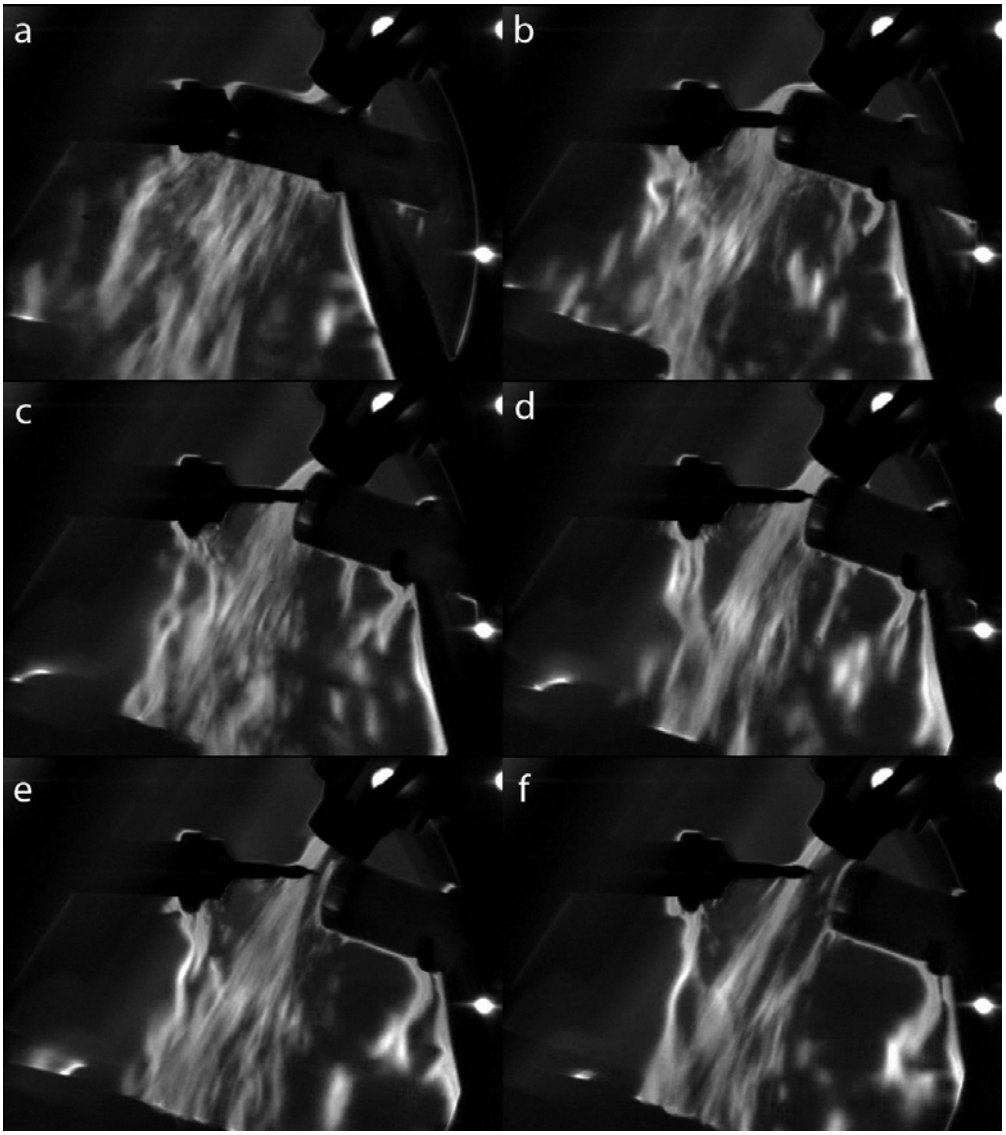

Figure 3.4

Schlieren images from successive frames of a video of mounting the base on the goniometer head. As the vial is withdrawn, large disturbances in the cold gas flow are observed, suggesting that the sample may come in contact with ambient-temperature air.

3.2.4 Annealing during mounting

In Figure 3.5 we show typical and worst-case examples of the thermal history of the thermocouple during the mounting process. There is a large variability: from the large spike shown in Figure 3.5b to no feature at all. A typical spike is shown in Figure 3.5a. The chaotic nature of the turbulence during mounting makes it difficult to quantify the amount of annealing when comparing different setups.

3.2.5 Improved method using liquid nitrogen stream wetted to the goniometer base

We experimented with different ways of mounting to eliminate temperature spikes during mounting. Some variables explored were the sample-to-nozzle distance, the angle between the goniometer axis and the nozzle axis, the flow rate, and the speed with which the cap was withdrawn (within reasonable speeds attainable by manual withdrawal). We did not perform enough trials with each variable to discern any systematic effects, but temperature spikes were observed at least once with each configuration tried.

Another method of keeping the sample cold during mounting is to direct a stream of liquid nitrogen at the goniometer base throughout the mounting process. This presented its own difficulties, but we were eventually able to find a method that always prevented any measurable temperature spike.

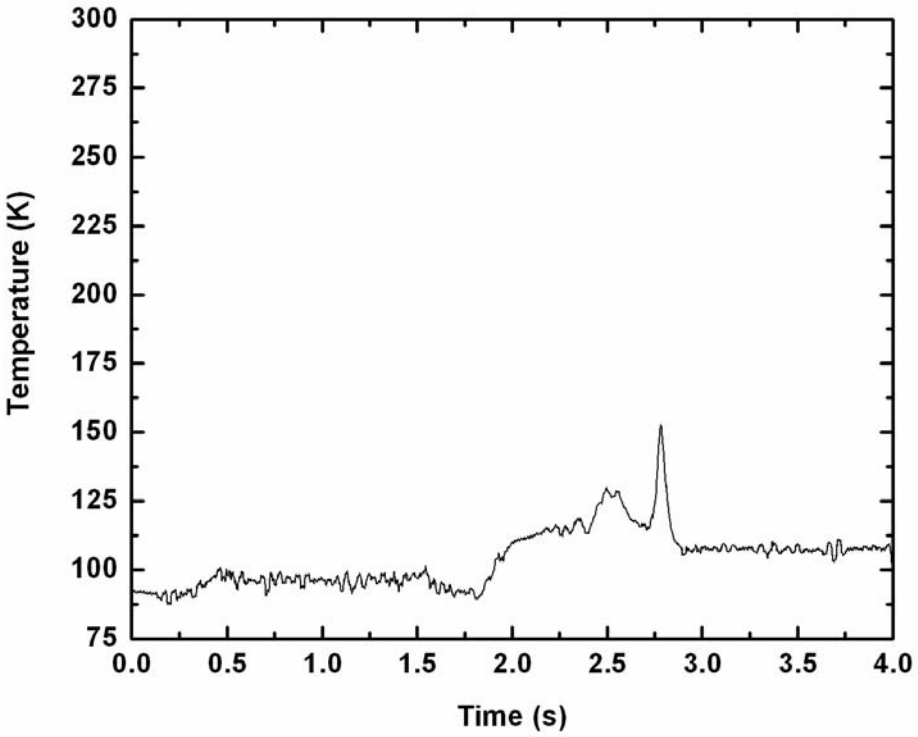

Figure 3.5a

The thermal history of a thermocouple placed at the sample position during mounting is shown. The temperature remains at liquid nitrogen temperature (~77 K) until the vial is tipped horizontally, at which point it begins to warm slowly. As the vial is withdrawn from the base, the temperature becomes erratic. In this trial, the maximum temperature recorded was 150 K, a typical value.

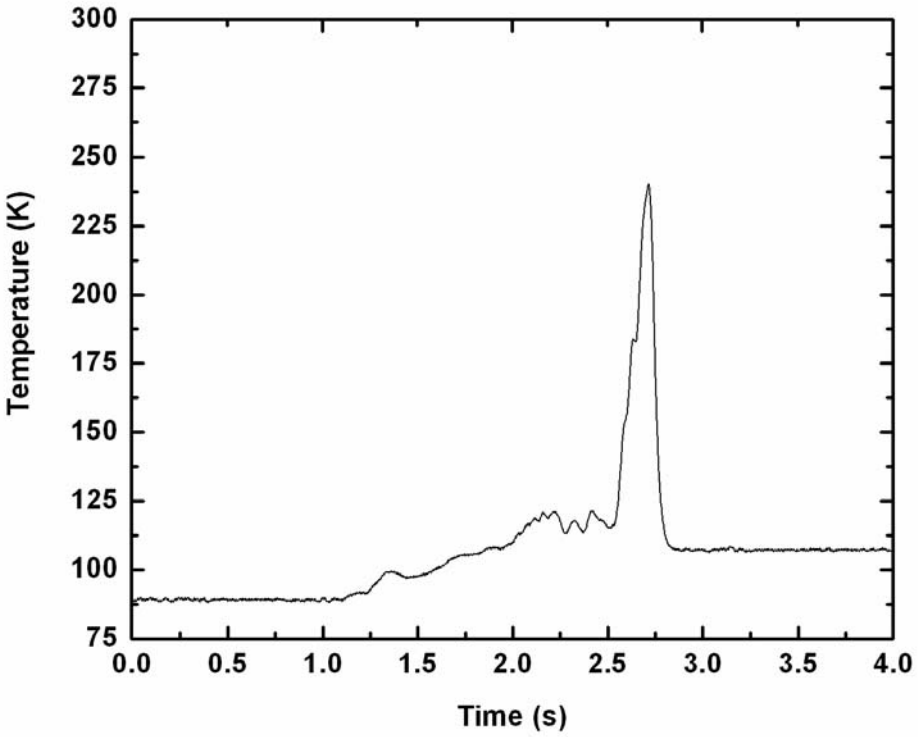

Figure 3.5b

A second trial identical to the one shown in Figure 3.5a is shown. In this case, the sample temperature reaches 240 K.

If liquid nitrogen comes in contact with a room-temperature surface, it will not wet the surface due to the boiling regime (a property of the liquid). Instead, a thin layer of gas will form between the liquid and the warm surface. At lower temperatures, the liquid will wet the surface, and cling to it because of surface tension. The temperature at which the wetting transition occurs is called the Leidenfrost temperature (Incropera & DeWitt, 2002).

This means that if the stream of liquid nitrogen is directed at a warm part of the apparatus, it will simply slide off. If it instead is directed at a cold part (the pin of the mount, or the pin of the base, for example), it will stick. An example of the type of wetting desired is shown in Figure 3.6. If the stream is directed along the pin, it will run all the way down to the end of the pin and keep the sample wetted. This ensures that it remains at 77 K during the entire mounting process.

3.3 Discussion

The unintentional annealing of protein crystals during mounting is undesirable for several reasons. When designing a cooling strategy, experimenters typically add cryoprotectants (solutes that inhibit ice formation) (Garman & Mitchell, 1996; Chinte *et al*., 2005; Berejnov *et al*., 2006). Once a sufficiently high concentration of cryoprotectant is reached, no ice will be observed on cooling. However, the required concentration decreases as the cooling rate increases. Small samples that can be cooled rapidly require less cryoprotectant, or even none at all (Warkentin *et al*., 2006). Since sample sizes vary from experiment to experiment, different amounts of cryoprotectant will be required with each experiment. This unpredictability leads

experimenters to err on the side of caution, often using more cryoprotectant than is necessary. Unintentional annealing adds to this variability, and exaggerates the required cryoprotectant concentration.

If care is taken to cool a sample into a state far from equilibrium (perhaps by hyperquenching (Warkentin *et al*., 2006) or at high pressure (Kim *et al*., 2007)), annealing can allow the system to relax, undoing whatever effect the special protocol might have had. For example, the thermocouple used in this study will cool at ~20,000 K/s during hyperquenching, and yet the re-cooling following unintentional annealing in Figure 3.3 proceeds at 1,000 K/s.

The cooling process itself almost always produces disorder in the crystal. The amount of disorder produced varies from sample to sample in an unpredictable way. If methods of cooling are to be devised that reduce this disorder, it is important to reduce variability as much as possible. Introducing an unknown amount of annealing into each trial will add to the variability and confound the search for optimal cooling protocols.

3.3.1 Sample size determines thermal response time

It is important that the reported thermal response of our thermocouples reflects the actual thermal response of biological samples. In general, the thermal response is a determined by properties of the sample and the surroundings. In particular, the sample's thermal mass and conductivity are important, as well as its geometry. The properties of the surroundings can be summarized in the boundary layer approximation with a fixed heat transfer coefficient. In the limit of infinite sample

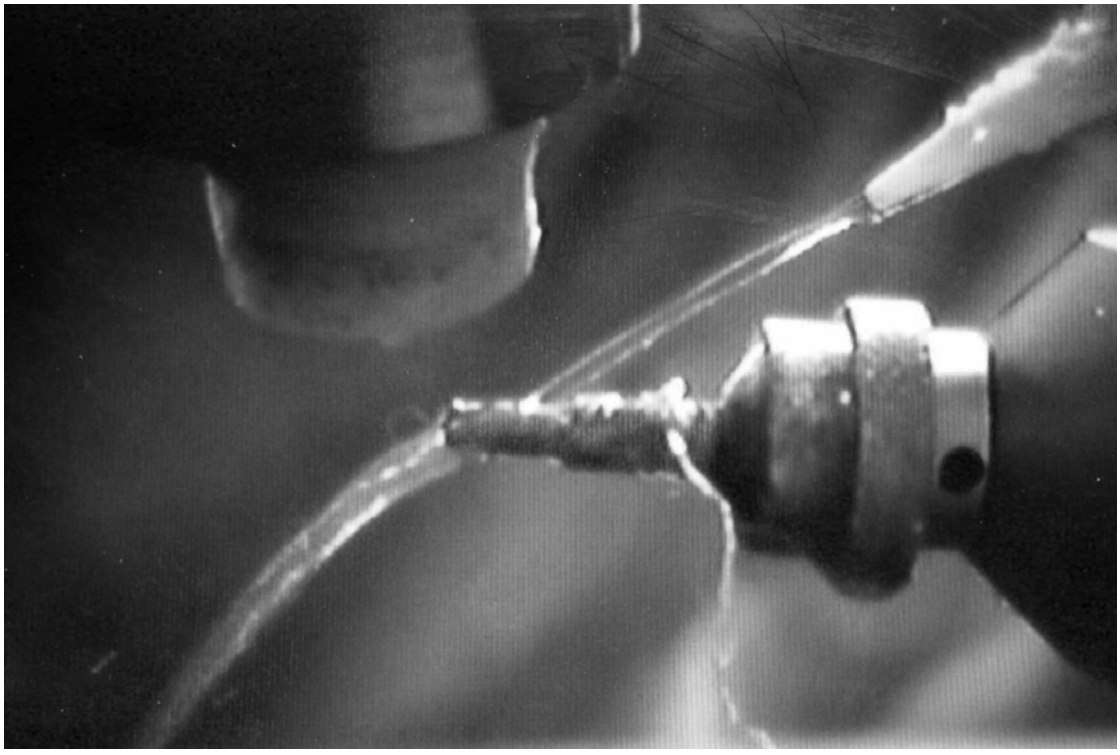

Figure 3.6

A photograph of a mounting method that prevents unintentional annealing is shown. Liquid nitrogen emerges from a pipette tip and clings to the base. This technique can be used to keep the sample wetted with liquid nitrogen during the entire mounting process. Once the cryostream reaches steady state, the stream can be taken away.

thermal conductivity, the cooling rate is determined completely by the heat transfer coefficient, the sample's surface-to-volume ratio, and the sample's thermal mass. It has been shown that cooling of samples of the size under consideration take place in this regime, both for metals and aqueous samples (Zasadzinski, 1988; Bailey & Zasadzinski, 1991). We point out in addition that the volumetric heat capacities of chrome and constantan (the materials comprising our thermocouples) differ from that of water by less than 50 %.

If differences in volumetric heat capacities are ignored, then the thermal mass is determined by the sample volume. Additionally, if all samples are assumed to be spherical, then the thermal response is determined entirely by the size of the sample size. These approximations will be valid to at least a factor of two for most protein crystallography experiments, making the measured thermal histories a valid comparison.

3.3.2 Comparison to previous work

Parkin & Hope, (1998) have measured sample temperature during the mounting process and observed that no measurable annealing occurs. They used a home-made thermocouple with 76 μm leads. They do not state the size of the junction however, and the junction size determines the sensitivity of the probe (see previous section). We can get an estimate of the response of their thermocouple based on its rise time. In Figure 9a of their paper, the thermocouple warms at ~10 K/s once mounted in the cryostream. This is the fastest temperature change they observe. By comparison, the thermocouple we used cools at a rate of ~1000 K/s following the large temperature

spike shown in Figure 3.3 of this chapter. Based on this comparison, we conclude that their thermojunction had a rise time approximately 100 times larger than the one used in this study. This suggests that they could not have observed the thermal fluctuations even if they were present.

Another difference in that study was the use of tongs for mounting, as opposed to vial + forceps. It is possible that tongs eliminate unintentional annealing, but this conclusion cannot be drawn based on the Parkin & Hope study due to the limited sensitivity of the thermocouple used in that study.

3.3.3 Effect of reducing sample size

As already mentioned, the sensitivity of a sample to its thermal environment is determined almost exclusively by its overall size. In protein crystallography, there are a number of reasons that smaller and smaller samples are being used. It is easier to grow small crystals than it is to grow large ones. Most proteins simply do not crystallize, but of those that do, few grow to sizes in excess of 100 - 200 μm. Additionally, X-ray sources have become bright enough that a complete dataset can be obtained from a 20 - 50 μm crystal in a reasonable amount of time. This means that there is no need to work towards growing larger crystals. Finally, the sample size is determined by the size of the crystal plus the volume of surrounding liquid. To obtain the highest resolution datasets, practitioners work to eliminate as much surrounding liquid as possible, because it contributes to the diffuse background in the diffraction pattern obtained.

The importance of sample size has also been seen in the case of plunging into liquid nitrogen in a dewar. As the sample size is reduced, cold gas above the liquid nitrogen in the dewar becomes the determining factor in the cooling rate. This is because a small sample (less than 100 μm) equilibrates with the cold gas in a time comparable to the time required to traverse the cold gas layer. The solution in this case is simple: blow the gas away using warm, dry nitrogen (Warkentin *et al*., 2006).

3.4 Conclusions

Size is the most important determinant of a sample's sensitivity to temperature fluctuations. As the samples used in protein crystallography have gotten progressively smaller, complications have arisen that were not present with larger samples. In this study, we have examined the susceptibility of tiny samples to unintentional annealing during the mounting process. We find that samples of size ~ 20 μm can warm to ~240 K during standard procedures. We have used schlieren imaging to show that the source of this annealing is the chaotic nature of the cold gas during mounting. This implies that even a robotic system will be unable to prevent the annealing. Finally, we have demonstrated a simple method to eliminate the annealing completely, in every case. We direct a stream of liquid nitrogen at the sample during the entire mounting process.

REFERENCES

Bailey, S. M. & Zasadzinski, J. A. N. (1991). *Journal of Microscopy-Oxford* **163**, 307-320.

Berejnov, V., Husseini, N. S., Alsaied, O. A. & Thorne, R. E. (2006). *Journal of Applied Crystallography* **39**, 244-251.

Chinte, U., Shah, B., DeWitt, K., Kirschbaum, K., Pinkerton, A. A. & Schall, C. (2005). *Journal of Applied Crystallography* **38**, 412-419.

Garman, E. F. & Mitchell, E. P. (1996). *Journal of Applied Crystallography* **29**, 584-587.

Garman, E. F. & Schneider, T. R. (1997). *Journal of Applied Crystallography* **30**, 211-237.

Hanson, B. L., Harp, J. M. & Bunick, G. J. (2003). *Methods in Enzymology*, Vol. 368. *Macromolecular Crystallography, Pt C*, pp. 217-235.

Harp, J. M., Hanson, B. L., Timm, D. E. & Bunick, G. J. (1999). *Acta Crystallographica Section D-Biological Crystallography* **55**, 1329-1334.

Harp, J. M., Timm, D. E. & Bunick, G. J. (1998). *Acta Crystallographica Section D-Biological Crystallography* **54**, 622-628.

Incropera, F. P. & DeWitt, D. P. (2002). *Fundamentals of heat and mass transfer*. New York: J. Wiley.

Juers, D. H. & Matthews, B. W. (2004). *Acta Crystallographica Section D-Biological Crystallography* **60**, 412-421.

Kim, C., Hao, Q. & Gruner, S. (2007). *Biophysical Journal* 317A-317A.

Kriminski, S., Caylor, C. L., Nonato, M. C., Finkelstein, K. D. & Thorne, R. E. (2002). *Acta Crystallographica Section D-Biological Crystallography* **58**, 459-471.

Parkin, S. & Hope, H. (1998). *Journal of Applied Crystallography* **31**, 945-953.

Pflugrath, J. W. (2004). *Methods* **34**, 415-423.

Rodgers, D. W. (1994). *Structure* **2**, 1135-1140.

Sanishvili, R., Nagarajan, V., Yoder, D., Becker, M., Xu, S. L., Corcoran, S., Akey, D. L., Smith, J. L. & Fischetti, R. F. (2008). *Acta Crystallographica Section D-Biological Crystallography* **64**, 425-435.

Stevenson, C. E. M., Mayer, S. M., Delarbre, L. & Lawson, D. M. (2001). *Journal of Crystal Growth* **232**, 629-637.

Warkentin, M., Berejnov, V., Husseini, N. & Thorne, R. (2006). *Journal of Applied Crystallography* **39**, 805-811.

Zasadzinski, J. A. N. (1988). *Journal of Microscopy-Oxford* **150**, 137-149.

CHAPTER 4

CRYOCRYSTALLOGRAPHY IN CAPILLARIES: CRITICAL GLYCEROL CONCENTRATIONS AND COOLING RATES

4.1 Introduction

Capillary tubes have long been used to grow macromolecular crystals (Salemme, 1972; McPherson, 1982). They provide a convenient way of controlling crystallization conditions and of handling and storing the resulting crystals. If thin-walled glass or plastic capillaries are used, crystals can be examined *in situ* by X-ray diffraction.

A variety of growth methods can be implemented in capillaries, including equilibrium dialysis (Zeppezauer *et al.*, 1968), liquid counterdiffusion (Salemme, 1972), gel acupuncture (García-Ruiz and Moreno, 1994), vapor diffusion along the capillary (Sibille *et al.*, 1991), and vapor diffusion through the capillary walls (Kalinin & Thorne, 2005). Vapor diffusion rates along the capillary between liquid plugs can be controlled by the choice of separating liquid or gas. When polymer capillaries are used, vapor diffusion rates can be controlled by adjusting the wall thickness and ambient humidity.

Crystal growth in capillaries is attracting renewed interest in the high-throughput era as an alternative to growth in crystallization plates. Using conventional liquid handling devices (Meldrum *et al*., 2000) or microfluidics (Li *et al.*, 2006; Zheng *et al*., 2005; Zheng *et al.*, 2004; Zheng *et al*., 2003), a large number of small-volume crystallization experiments can be conducted in a single capillary. Reagent volumes and the extent of reagent mixing can be precisely controlled. The system described by Meldrum *et al*. accurately dispenses volume increments as small as 0.3 nl in glass capillaries with an

inner diameter of 340 μm. The microfluidic system described by Zheng *et al*. dispenses 10-100 nl volumes in glass or Teflon capillaries with diameters near 200 μm. Recent implementations replace free-standing capillary tubes with arrays of capillary lines fabricated in a flat PDMS/Teflon or plastic "card".

An important reason for interest in capillary growth is the possibility of *in-situ* X-ray examination of individual drops, both as a compliment to optical examination in screening and for full structure determination. Well-faceted crystals are often poorly ordered, and any crystals present in a drop may be visually obscured by precipitate or by "skins" covering the drop surface. X-rays directly probe the presence of crystalline order and the extent of this order, the properties of interest in crystallography. For X-ray examination in capillaries, the capillary walls should be thin (typically 10 μm for glass and 25-50 μm for polymers) and of an amorphous, isotropic material to minimize background scatter. Thin-walled polyethylene terephthalate (PET), Kapton and Teflon tubing with good optical and X-ray clarity is commercially available, and unlike glass does not crack or shatter during handling (Kalinin *et al.*, 2005).

In situ structure determination at room temperature is complicated by rapid accumulation of radiation damage and by crystal slippage/sedimentation as the capillary is rotated during data collection. Slippage can be reduced by removing excess liquid (which is not practical when multiple drops are dispensed in a single capillary) or by growing the crystals in gels (which increases background scatter.) The obvious solution to these difficulties is to cool the crystals *in situ* to cryogenic temperatures. Solidification of the solvent inside the crystals dramatically reduces radiation damage rates, and solidification of the solvent outside the crystals immobilizes them. *In situ* capillary cryocrystallography using crystals grown with cryoprotectants and heavy atom compounds has been demonstrated for some model proteins (Lopez-Jaramillo *et al.*, 2001; Gavira *et al.*, 2002; Ng *et al.*, 2003). High

pressure freezing without cryoprotectants has also been demonstrated as a route to structure solution in capillaries (Kim *et al.*, 2007).

When cooling at ambient pressure, cryoprotectants such as glycerol, polyethylene glycols, and 2-methyl-2,4-pentanediol are added to inhibit formation of crystalline ice, both within the crystal and in the surrounding liquid. Ice creates diffraction rings that obscure diffraction from the protein crystal, and growth of ice crystals can disrupt the crystal lattice. Typical cryoprotectant concentrations required to inhibit crystallization of the surrounding liquid are 20-30% w/v (Garman & Mitchell, 1996). In high-throughput capillary growth, these cryoprotectants must be introduced with the original mother liquor, and can thus constrain the search for optimal crystallization conditions. Cryoprotectant concentrations required to prevent crystalline ice formation can be reduced by cooling the sample faster (Chinte *et al.*, 2005; Berejnov *et al.*, 2006; Warkentin *et al.*, 2006) or by increasing the pressure (Kim *et al.*, 2007).

Here we report the cooling rates achieved when thin-walled PET tubing containing a glycerol-water solution is plunged into liquid nitrogen and into liquid propane, and the corresponding minimum glycerol concentrations required to prevent crystalline ice formation. Tubing diameters from 150 μm to 3.3 mm, covering the range of interest for protein crystallography and cryopreservation, are examined. Maximum cooling rates are significantly smaller and minimum glycerol concentrations and significantly larger than can be achieved when crystals are cooled in standard loop or microfabricated X-ray crystallography mounts (Warkentin *et al.*, 2006). Combining our results with those of previous studies, we find a nearly exponential dependence of the minimum cooling rate for vitrification on glycerol concentration, spanning more

than five orders of magnitude in cooling rate. This relation provides a basis for designing cryopreservation protocols.

4.2 Materials and Methods

4.2.1 Critical concentration measurements

One way to determine the efficacy of capillaries for cryopreservation is to measure the minimum amount of cryoprotectant required for vitrification of water-cryoprotectant solutions as a function of tubing diameter and wall thickness. Smaller diameters should give larger cooling rates and require smaller cryoprotectant concentrations.

Optical assays have long been used to quantify phase separation and crystallization in aqueous mixtures and in biological samples, especially during rapid cooling of small volumes for which microcalorimetry measurements are extremely challenging. Density fluctuations associated with the appearance of new phases produce refractive index fluctuations that scatter light, and index variations of as little as 10^{-5} on scales of roughly one-tenth the optical wavelength produce visible contrast and cloudiness. Previous studies have explored the structural state (vitreous/amorphous or crystalline) of rapidly cooled aqueous cryoprotectant solutions. If the sample vitrifies as it cools, it remains transparent; if ice microcrystallites form, they scatter light and the sample becomes cloudy (Luyet, 1957; Fahy *et al.*, 1984; Garman & Schneider, 1997; McFerrin & Snell, 2002, Chinte *et al.,* 2005). The transition from transparent to non-transparent occurs over a narrow range of glycerol concentration (less than 2%), if all else is held fixed (Garman & Mitchell, 1996; Berejnov *et al*,. 2006). Although earlier X-ray diffraction measurements suggested the presence of crystalline ice in optically transparent samples (McFerrin & Snell, 2002, Chinte *et al.,* 2005), more recent

measurements with more accurate evaluation of the first visual deviation from complete transparency confirm that this deviation corresponds to a state change from vitreous to microcrystalline, and limit any discrepancy between the optical and X-ray deduced transitions to less than 2% in glycerol concentration (Berejnov *et al.*, 2006).

The PET tubing used for all experiments was obtained from Advanced Polymers (Salem, NH, USA), and has excellent X-ray transparency (Kalinin *et al.*, 2005). Tubing inner diameters ranged from 150 μm to 3.3 mm. Wall thicknesses were either 25 or 50 μm for diameters of 500 μm and larger, and either 12 or 25 μm for smaller diameters. Open-ended pieces of tubing at least ten diameters long were completely filled with water-glycerol solutions of increasing concentration, in increments of 2 % w/v. The solutions were prepared by first weighing out the appropriate amount of glycerol, and then thoroughly mixing in water to bring the total solution volume to the desired value. Each solution's refractive index was measured and indicated an error in final concentration of less than 0.2 % w/v, or 10% of our concentration increment. Each sample was then plunged at ~0.5 m/s into liquid propane or liquid nitrogen and held horizontally until all boiling ceased. Sample transparency was determined by holding the sample immediately above the liquid surface and observing it against a black paper background with fiber optic illumination and a boom-mounted stereomicroscope.. For each tubing diameter, the smallest glycerol concentration that resulted in a completely transparent sample was recorded, as shown in Figure 4.1.

Liquid nitrogen was held in a glass hemispherical Dewar, 12 cm across and 8 cm deep (Pope Scientific Inc, Saukville, WI, USA), with the liquid level maintained within 2 cm of the brim. Commercial liquid propane, (Coleman brand) was transferred from the tank into a 50 ml centrifuge tube held under liquid nitrogen. Commercial propane is safer (due to additives that give it a putrid smell) and cheaper than pure propane and, because of impurities, freezes at a lower temperature. 10 ml of liquid propane was

poured from the tube into a custom aluminium trough roughly 10 cm long, 2 cm deep and with 1 mm thick walls that was partially submerged in liquid nitrogen. The propane's temperature was measured using a chrome-constantan thermocouple (CHCO-005, Omega Engineering), and remained in the range 90 to 95 K provided that the liquid nitrogen level was kept halfway up the side of the trough.

For 150 and 200 μm diameter capillaries plunged in liquid nitrogen, the fastest cooling was obtained by blowing away the cold gas layer that forms above the liquid using dry room temperature nitrogen gas (Warkentin *et al.*, 2006), and only those data are reported. For larger capillaries, the cold gas layer had no effect on the critical concentration. For plunging into liquid propane, the propane was held in a fume hood. The flowing air kept the thickness of the cold gas layer small, and additional blowing was not used so as to minimize warming of the liquid.

4.2.2 Cooling rate measurements

The temperature inside the capillary during cooling was measured using chrome-constantan thermocouples with lead diameters of either 25 μm or 75 μm and bead diameters of 80 μm or 125 μm, respectively (CHCO-001 or CHCO-003 Omega Engineering). Thermocouple response times were measured by directly plunging into propane and into nitrogen, and were much shorter than all measured cooling times of liquid-filled capillaries.

For cooling rate measurements in capillaries, a thermocouple was threaded lengthwise through the capillary to place its bead near the center. The capillary was filled with a 60 *% w/v* glycerol solution, which vitrifies for all cooling rates and thus does not exhibit temperature anomalies associated crystallization and release of latent heat.

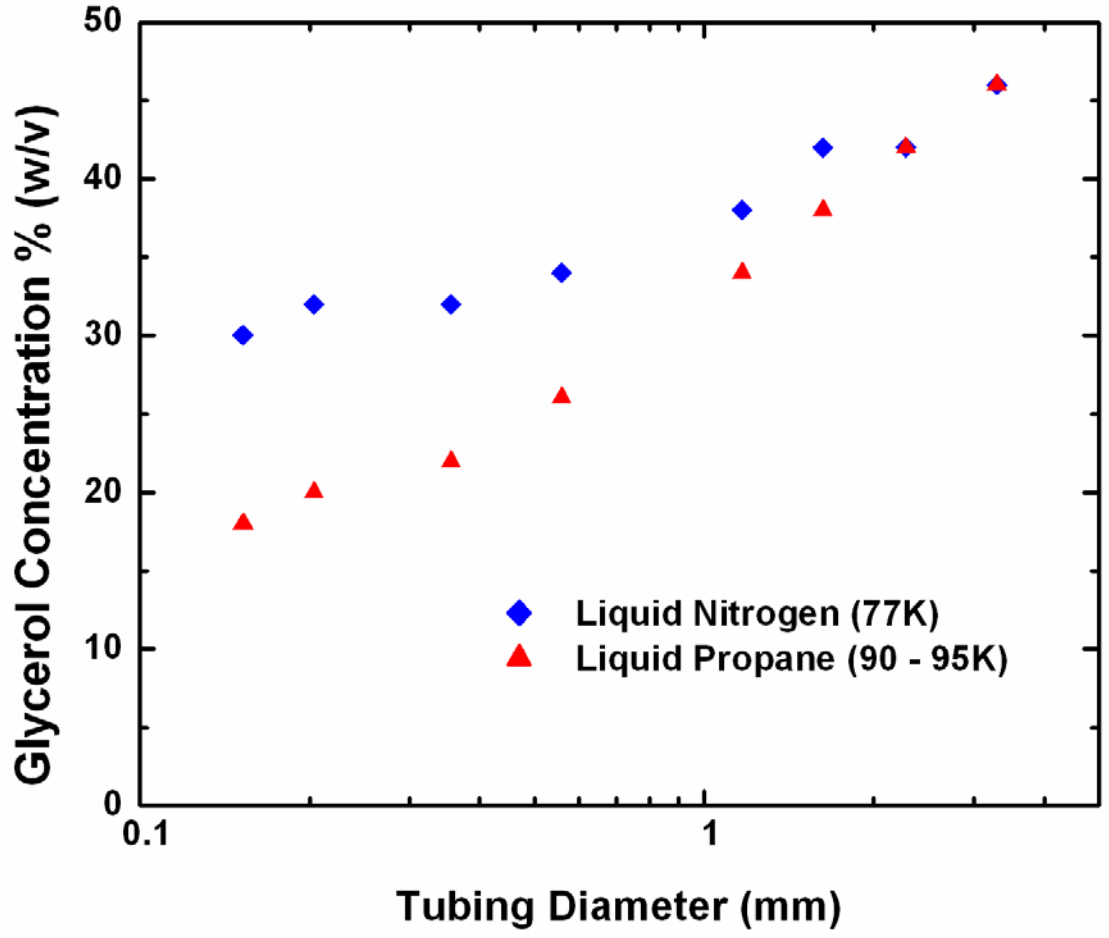

Figure 4.1

The concentration of glycerol in water required to obtain a completely transparent sample upon plunging into either liquid propane or liquid nitrogen. PET tubing wall thicknesses are 12.5 or 25 μm for diameters below 500 μm and 25 or 50 μm for larger diameters.

These samples were plunged into the liquid cryogen as in the critical concentration measurements. The thermocouple's bead size and radial position should affect the measured temperature. In practice, capillary time-temperature profiles for different bead sizes and positions within the capillary were indistinguishable — within the typical 20% trial-to-trial variation in measured cooling rates — down to the smallest capillary sizes. This variation is small compared with the nearly three-order-of-magnitude variation in cooling rate with tubing diameter. Temperature *versus* time data were recorded by a 6025e PCI DAQ interface controlled by LabView (http://www.ni.com/labview), both from National Instruments.

4.3 Results

4.3.1 Estimation of cooling rates

Figure 4.2 shows representative cooling curves for capillaries filled with 60% *w/v* glycerol solution and plunged into liquid nitrogen or liquid propane. Because the slopes of these curves are not constant, it is not immediately clear how to define the relevant cooling rate. For propane, the cooling rate is highest immediately after the sample enters the propane. For nitrogen, the cooling rate is largest midway through the cooling process, just after the transition from film to nucleate boiling at ~200 K (Incropera & DeWitt, 2002; Gakhar & Wiencek, 2005). The region of the cooling curves most relevant to successful cryocooling will depend upon the properties of the solution being cooled, as cryoprotectants decrease the homogeneous nucleation temperature and increase the glass transition temperature. (Rasmussen & Luyet, 1970; MacKenzie, 1977).

We thus estimated three different cooling rates, as shown in Figure 4.2. For cooling in liquid propane (Figure 4.2c), we evaluated the average cooling rate from the initial temperature down to T=150 K. The latter temperature was chosen because the glass transition temperatures of most cryoprotectant solutions (MacKenzie, 1977; Harran, 1987) and of the solvents within protein crystals (Weik, 2001; Weik, 2004; Weik, 2005) are between 140 and 180 K. For cooling in liquid nitrogen (Figure 4.2d), there are two distinct regimes of cooling. In the nucleate boiling regime at lower temperatures, the liquid nitrogen directly contacts the sample and the cooling rate is large. In the film boiling regime at higher temperatures, the cooling rate is roughly an order of magnitude smaller due to a layer of vapor insulating the sample from the liquid nitrogen. The transition between these two regimes occurs at the Leidenfrost temperature. (Incropera & DeWitt, 2002). We thus evaluated the average cooling rate in the film boiling regime from room temperature down to the Leidenfrost temperature, and the maximum cooling rate just below this temperature in the nucleate boiling regime. A fourth cooling rate (not shown in Figure 4.2) — the average cooling rate in nitrogen from the initial temperature down to T=150 K — was also evaluated, and is close to the average cooling rate in the film boiling regime.

Figure 4.3 shows the resulting cooling rates versus capillary diameter d. All cooling curves show a smooth variation with tubing size. They are well fit by power laws $dT/dt \sim d^{\alpha}$ with exponents α of -1.75 for cooling in liquid propane, -1.46 for the film boiling regime in liquid nitrogen, and -1.14 for the nucleate boiling regime in liquid nitrogen. An exponent of 1 is expected if the cooling rate is dominated by the gas or liquid boundary layer immediately adjacent to the tubing, while a value of 2 is expected if the cooling rate limited by thermal diffusion (e.g., through the sample, or through a coolant in which convection was unimportant) (Zasadzinksi, 1988; Bailey & Zasadzinksi, 1991).

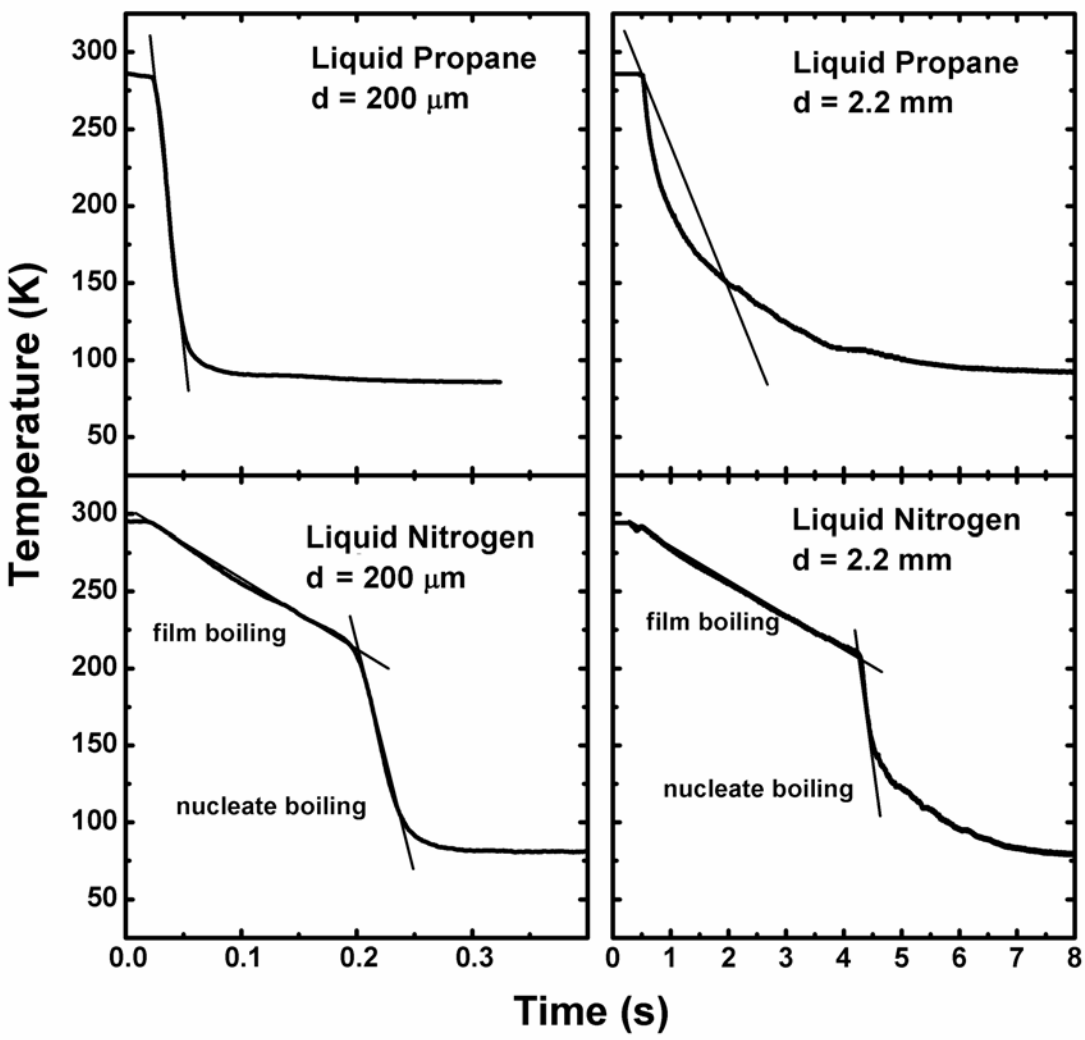

Figure 4.2

Representative cooling curves when capillaries containing 60% glycerol-water solutions are plunged into liquid propane and liquid nitrogen. The slopes of the straight lines give the cooling rates shown in Figure 4.3.

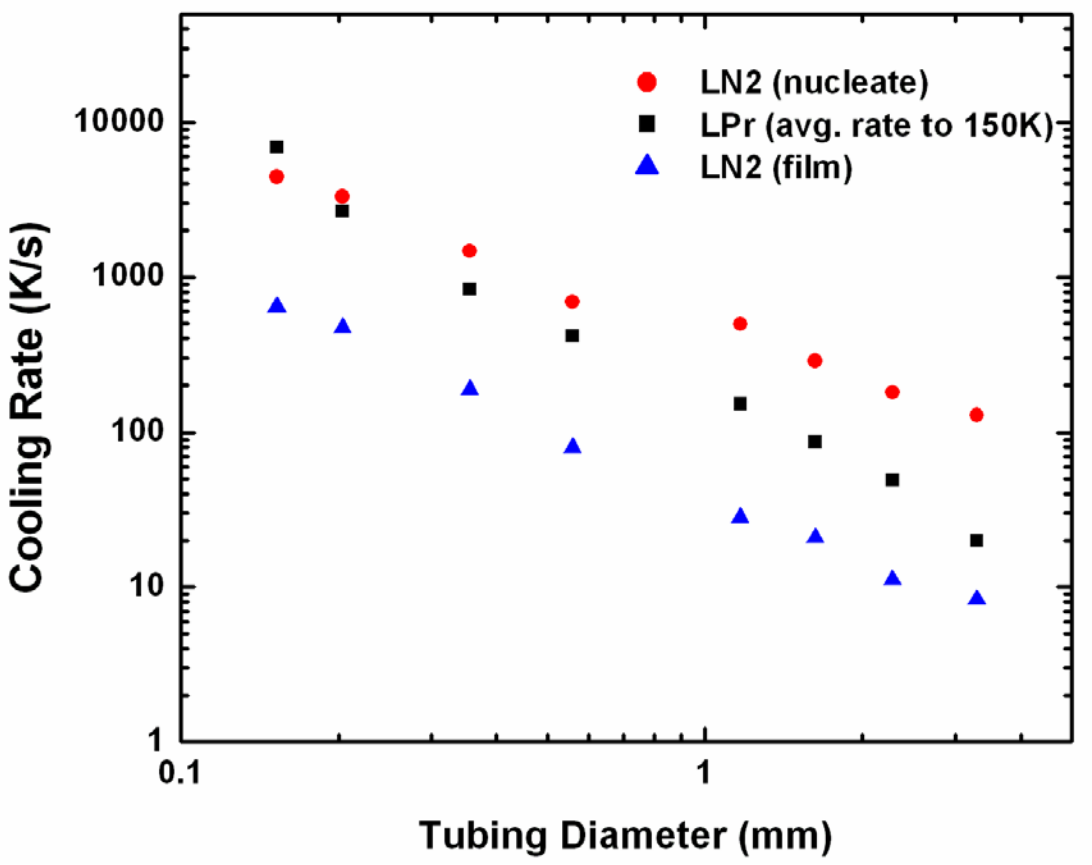

Figure 4.3

Cooling rates as a function of tubing diameter, for liquid propane and liquid nitrogen, as estimated in Figure 4.2. Each data point represents an average over 5 to 10 trials. The trial-to-trial variation was 10% (for larger diameters) to 20% (for smaller diameters), and comparable to the height of the symbols used to mark the data.

4.3.2 Comparison to previous work

Previous studies of cooling using loop-mounted samples found cooling rates similar to those reported here for similar size samples. Teng and Moffat (1998) examined 125 μm to 450 μm thick films of cryoprotected crystallization buffers suspended on 1.5 mm loops, and found cooling rates in gas streams, liquid nitrogen and liquid propane ranging from 130 to 1200 K/s, depending upon the film thickness, the cooling agent, and (in the case of liquid nitrogen) the boiling regime. These rates are in rough agreement with the corresponding rates observed in a ~350 μm capillary shown in Figure 4.3. Walker *et al.* (1998) found average cooling rates of 250 K/s and 750 K/s in liquid nitrogen and liquid propane, respectively, for a rubber cement coated thermocouple forming a spherical sample of diameter 0.7 mm. Interpolating the data of Figure 4.3 to a capillary tube with 0.7 mm diameter gives cooling rates of 67, 338, and 726 K/s for film-boiling liquid nitrogen, liquid propane, and nucleate-boiling liquid nitrogen, respectively.

The material at the sample's surface (aqueous solution in the case of loop mounted samples, PET or glass for capillary mounted samples) affects the Leidenfrost temperature and so should modify observed cooling rates in liquid nitrogen (Gakhar & Wiencek, 2005). With a higher Leidenfrost temperature, the nitrogen near the sample's surface will enter the nucleate boiling regime sooner, and the cooling rate to ~150 K will be larger. For example, the Leidenfrost temperatures for the bare thermocouples (chrome/constantan alloy surfaces) used by Gakhar & Wiencek (2005), and by Warkentin *et al*. (2006), were 130-150 K, compared with nearly 200 K for the PET covered samples here (see Figure 4.3). In addition, surface roughness can influence the Leidenfrost temperature and the rate of heat transfer in the nucleate

boiling regime (Bald & Wang, 1976; Dhir, 1998), in both liquid nitrogen and (for larger samples) liquid propane.

In the film boiling regime, the mechanism of heat transfer is comparatively well understood. For a horizontally held cylinder of diameter d, Bromley (1950) derived a heat transfer coefficient $h \sim d^{-1/4}$. The cooling rate should then follow $dT/dt \sim d^{-5/4}$. Subsequent experiments revealed deviations from this power law at small diameters that have been fit with more sophisticated empirical forms for h (Breen & Westwater, 1962; Baumeister & Hamill, 1967). Over the range of diameters examined here, these forms can be approximated by $h \sim d^{-7/12}$ (Bakhru & Lienhard, 1972). The cooling rate in the film boiling regime is then $dT/dt \sim d^{-1.58}$. The exponent is close to the value of -1.46 observed here. A more detailed fit based upon the correlation of Baumeister & Hamill (1967) gives even closer agreement with our experimental results.

4.4 Discussion

4.4.1 Implications for cryocrystallography in capillaries

Figure 4.1 indicates that successfully cooling protein crystals in capillaries at ambient pressure will require large cryoprotectant concentrations to prevent crystalline ice formation in the liquid surrounding the crystal. Even with 150 μm diameter tubing, 30% and 20% *w/v* glycerol will be required for cooling in liquid nitrogen and liquid propane, respectively. Similarly large concentrations of other cryoprotectants can be expected (Berejnov *et al*., 2006). For samples in this range of surface-to-volume ratios that are cooled using these cryogens, it has been shown experimentally and theoretically that the thermal conductivity of the sample does not affect the cooling

rate (Zasadzinksi, 1988; Bailey & Zasadzinksi, 1991; Kriminski *et al*., 2003), and so these results will approximately hold for capillaries made from other materials as well. Figure 4.1 suggests that more manageable cryoprotectant concentrations may be achieved using 10 to 50 μm diameter capillaries. For a fixed pressure drop, the speed of capillary flow varies as d^4 (Poiseuille's Law), so filling such small capillaries may be problematic. Handling such tiny capillaries and obtaining useable diffraction from the tiny crystals inside would also be difficult. Arrays of capillary tubes can be fabricated in flat plastic sheets, but these have a much larger thermal mass per unit length of capillary and a more unfavorable geometry for heat transfer than isolated capillary tubes.

Compared with crystals on loops (Teng, 1990) or microfabricated mounts (Thorne *et al.*, 2003), performing cryocrystallography on crystals in capillaries presents substantial difficulties. Large cryoprotectant concentrations are required to prevent ice crystallization in the mother liquor surrounding the crystals. Much less cryoprotectant is required to prevent ice formation within the crystal itself, because protein acts as a excellent cryoprotectant at the concentrations found within the crystal (Kriminski *et al.*, 2002). For crystals in loops or on microfabricated mounts, surrounding mother liquor can be wicked away or replaced with low-viscosity oil. For capillary-grown and mounted crystals, removing or replacing this mother liquor without damaging the crystal is not easy, and would be less-so in high-throughput applications where each small-diameter capillary contains multiple samples. Furthermore, the mother liquor typically has a much larger total mass and thermal mass than the crystals that grow within it; the mother liquor + crystal have a much larger volume and thus a much smaller surface to volume ratio than the crystal itself; and cylindrical capillaries have 1/3 the surface-to-volume ratio of equal volume spherical samples. As a result,

achievable cooling rates in capillaries are much smaller than for conventionally mounted crystals, and penetrating cryoprotectants must be included in large concentrations.

The surrounding mother liquor present in capillaries produces background scatter that reduces a data set's signal-to-noise and ultimate resolution. In batch growth, 1-3% w/v of the initial growth solution (10-30 mg/ml) is protein, so that the maximum protein + solvent mass that ends up within crystals is typically less than 5% of the total mass. A 100 × 50 × 30 μm crystal examined by a 100 μm X-ray beam in a 200 μm capillary will typically have to compete with background scatter from surrounding liquid more than ten times its own volume.

The large amount of surrounding liquid present in capillaries will exert non-uniform stresses on the crystal during cooling, resulting from differences in thermal expansion/contraction of the crystal, of the surrounding liquid and of the capillary itself. Crystals with rod or plate-like shapes are likely to crack under these stresses, broadening their mosaicities.

4.4.2 Critical Cooling Rate vs. Glycerol Concentration

The data in Figures 4.1 and 4.3 can be combined to estimate the minimum cooling rate required to vitrify a given glycerol concentration, for a wide range of concentrations. The critical cooling rate to achieve vitrification is an intrinsic property of the solution, so it does not depend upon details such as sample geometry or coolant type, and directly reflects the fundamental physics of glass formation in the water-glycerol system. It can thus be used to design practical cryoprotection protocols in a variety of biological applications. Figure 4.4 is a composite showing our results (taken from

Figures 4.1 and 4.3), results for high concentrations / slow cooling rates determined by differential scanning calorimetry (DSC) on emulsified samples (Sutton, 1991), results where cooling rates were estimated from the time between the initial plunge into liquid nitrogen and the Leidenfrost transition to nucleate boiling (Berejnov *et al*., 2006), and results for pure water (Brugeller & Mayer, 1980). Our data span a large range of glycerol concentrations/cooling rates between those examined in previous studies. A crude fit to the merged data (solid line in Figure 4.4) suggests a simple exponential relation between glycerol concentration and cooling rate. The required cooling rate is halved with the addition of each ~3% glycerol concentration increment.

In generating Figure 4.4 we have assumed that the cooling rate of a capillary filled with 20-40% glycerol (data from Figure 4.1) is the same as the cooling rate of that same capillary filled with 60% glycerol (data from Figure 4.3). For samples cooled with liquid nitrogen or propane and having surface-to-volume ratios in the range studied here, it has been shown experimentally and theoretically (Zasadzinksi, 1988; Bailey & Zasadzinksi, 1991) that cooling rates depend upon the surface-to-volume ratio, the heat transfer coefficient (a property of the coolant), and the volumetric heat capacity of the sample. Similar cooling rates are obtained for samples differing in thermal conductivity by three orders of magnitude. In our experiments, the small difference in heat capacities of 20% glycerol and 60% glycerol solutions modifies cooling rates by less than 10%, and the small difference in thermal conductivity (~30%) is too small to affect our conclusions.

A potentially important issue in comparing cooling rate results from different measurements is the residual crystalline ice fraction at which a sample is deemed vitrified. Kresin & Korber (1991) reported measurements similar to Sutton's, using

DSC on emulsified samples. For Sutton's 59 % *w/v* sample, they estimate an ice fraction of 0.023, and suggest that reducing the ice fraction to 10^{-6} would require a cooling rate almost two orders of magnitude larger. The emulsion's drop size is also important: Kresin & Korber estimate that bulk systems would require a factor of two larger cooling rates than their 2.4 μm diameter droplets. Measurements of cooling rates to vitrify pure water also have uncertainties associated with the residual crystalline fractions.

In the X-ray diffraction experiments connecting the transparent to non-transparent visual transition with the vitreous ice to crystalline ice transition, crystalline ice becomes clearly noticeable when the ice ring intensity becomes significant compared to the intensity produced by the amorphous ice fraction of the sample (Berejnov *et al.*, 2006). The minimum detectable crystalline fraction can be estimated from measurements of scattered X-ray intensities from crystalline and amorphous samples *versus d* spacing. The signal-to-background ratios at the ice ring *d* spacing for typical amorphous and crystalline samples are ~1.5 and 10, respectively. If we assume a minimum detectable ice ring intensity of 1/10 the background intensity from vitreous ice, then this implies a minimum detectable crystalline ice fraction of roughly 0.01. This is comparable the fraction estimated for Sutton's experiment, but much smaller than that in Kresin & Korber. Since the visual assay for crystallinity (Luyet, 1957; Fahy *et al.*, 1984; Garman & Mitchell, 1996) corresponds so well with X-ray diffraction measurements (Berejnov *et al.*, 2006), the values quoted by Sutton are most appropriate for comparison to cooling rates determined here.

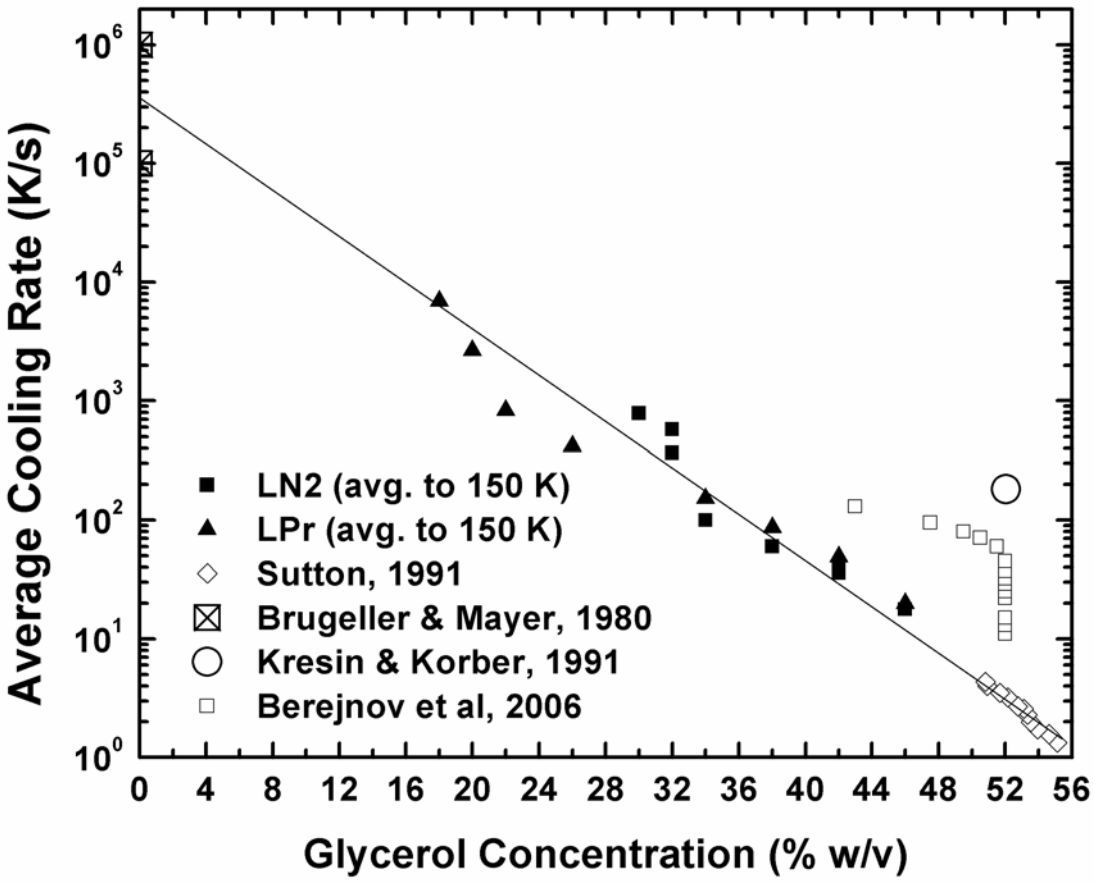

Figure 4.4

Minimum cooling rates to achieve vitrification of glycerol-water solutions as a function of glycerol concentration. Data inferred from the present study, as well as data for pure water and for glycerol-water solutions obtained in previous studies are shown. The thin line corresponds to an exponential relation between cooling rate and glycerol concentration.

4.5 Conclusion

We have determined the cooling rates of a glycerol-water solution inside thin-walled capillaries when plunged into liquid nitrogen and liquid propane, and the corresponding minimum glycerol concentrations required to prevent formation of crystalline ice. These results can be combined to yield the minimum cooling rate to achieve a vitreous sample as a function of glycerol concentration, a fundamental property of the water-glycerol solution. For PET capillary tubes of diameters ranging from 150 μm to 3.3 mm, the minimum required glycerol concentration is 20% and 30% for cooling in nitrogen and propane, respectively. These values are comparable to those currently used in cryocrystallography practice, but are much larger than is generally necessary to prevent ice crystallization within the crystal itself. Maximum achievable cooling rates of 300 K/s to 7000 K/s are at least an order of magnitude smaller than can be achieved using crystals on loop or microfabricated mounts. *In situ* capillary cryocrystallography will thus likely involve higher cryoprotectant concentrations, more crystal damage during cooling and much larger background scatter from surrounding liquid, and so in most cases is unlikely to yield the highest resolution structures. Its primary benefit will be in screening diffraction properties and crystallization outcomes in high throughput capillary crystallization.

REFERENCES

Bailey, S. M. & Zasadzinski, J. A. N. (1991). *Journal of Microscopy-Oxford* **163**, 307-320.

Bakhru, N. & Lienhard, J. H. (1972). *International Journal of Heat and Mass Transfer* **15**, 2011-2025.

Bald, W. B. & Wang, T. Y. (1976). *Cryogenics* **16**, 314-315.

Baumeister, K. M. & Hamill, T. D. (1967). *Mechanical Engineering* **89**, 79-88.

Berejnov, V., Husseini, N. S., Alsaied, O. A., & Thorne, R. E. (2006). *Journal of Applied Crystallography* **39**, 244-251.

Breen, B. P. & Westwater J.W. (1962). *Mechanical Engineering Progress* **58**, 67-72

Bromley, L. A. (1950). *Chemical Engineering Progress* **46**, 221-227.

Bruggeller, P. & Mayer, E. (1980). *Nature* **288**, 569-571.

Chinte, U., Shah, B., DeWitt, K., Kirschbaum, K., Pinkerton, A. A., & Schall, C. (2005). *Journal of Applied Crystallography* **38**, 412-419.

Dhir, V. K. (1998). *Annual Review of Fluid Mechanics* **30**, 365-401.

Fahy, G. M., Macfarlane, D. R., Angell, C. A., & Meryman, H. T. (1984). *Cryobiology* **21**, 407-426.

Gakhar, L. & Wiencek, J. M. (2005). *Journal of Applied Crystallography* **38**, 945-950.

Garcia-Ruiz, J. M. & Moreno, A. (1994). *Acta Crystallographica Section D-Biological Crystallography* **50**, 484-490.

Garman, E. F. & Mitchell, E. P. (1996). *Journal of Applied Crystallography* **29**, 584-587.

Garman, E. F. & Schneider, T. R. (1997). *Journal of Applied Crystallography* **30**, 211-237.

Gavira, J. A., Toh, D., Lopez-Jaramillo, J., Garcia-Ruiz, J. M., & Ng, J. D. (2002). *Acta Crystallographica Section D-Biological Crystallography* **58**, 1147-1154.

Harran, D. (1978). *Bulletin de la Societe Chimique de France Partie I-Physicochimie des Systemes Liquides Electrochimie Catalyse Genie Chimique* I40-I44.

Incropera, F. P. & DeWitt, D. P. (2002). *Fundamentals of heat and mass transfer*, 5th ed ed. New York: J. Wiley.

Johari, G. P., Hallbrucker, A., & Mayer, E. (1987). *Nature* **330**, 552-553.

Kalinin, Y. & Thorne, R. (2005). *Acta Crystallographica Section D-Biological Crystallography* **61**, 1528-1532.

Kida, M., Kikuchi, Y., Takahashi, O., & Michiyoshi, I. (1981). *Journal of Nuclear Science and Technology* **18**, 501-513.

Kim, C. U., Hao, Q., & Gruner, S. M. (2007). *Acta Crystallographica Section D-Biological Crystallography* **63**, 653-659.

Kresin, M. & Korber, C. (1991). *Journal of Chemical Physics* **95**, 5249-5255.

Kriminski, S., Kazmierczak, M., & Thorne, R. E. (2003). *Acta Crystallographica Section D-Biological Crystallography* **59**, 697-708.

Li, L., Mustafi, D., Fu, Q., Tereshko, V., Chen, D. L. L., Tice, J. D., & Ismagilov, R. F. (2006). *Proceedings of the National Academy of Sciences of the United States of America* **103**, 19243-19248.

Lopez-Jaramillo, F. J., Garcia-Ruiz, J. M., Gavira, J. A., & Otalora, F. (2001). *Journal of Applied Crystallography* **34**, 365-370.

Luyet, B. J. (1957). *Proceedings of the Royal Society of London Series B-Biological Sciences* **147**, 434-451.

Mackenzie, A. P., Derbyshire, W., & Reid, D. S. (1977). Philosophical *Transactions of the Royal Society of London Series B-Biological Sciences* **278**, 167-189.

McFerrin, M. B. & Snell, E. H. (2002). *Journal of Applied Crystallography* **35**, 538-545.

Meldrum, D. R., Evensen, H. T., Pence, W. H., Moody, S. E., Cunningham, D. L., & Wiktor, P. J. (2000). *Genome Research* **10**, 95-104.

Ng, J. D., Gavira, J. A., & Garcia-Ruiz, J. M. (2003). *Journal of Structural Biology* **142**, 218-231.

Rasmussen ,D. & Luyet, B. (1970). *Biodynamica* **11**, 33-44.

Salemme, F. R. (1972). *Archives of Biochemistry and Biophysics* **151**, 533-539.

Sibille, L., Clunie, J. C., & Baird, J. K. (1991). *Journal of Crystal Growth* **110**, 80-88.

Sutton, R. L. (1991). *Journal of the Chemical Society-Faraday Transactions* **87**, 101-105.

Teng, T. Y. (1990). *Journal of Applied Crystallography* **23**, 387-391.

Teng, T. Y. & Moffat, K. (1998). *Journal of Applied Crystallography* **31**, 252-257.

Thorne, R. E., Stum, Z., Kmetko, J., O'Neill, K., & Gillilan, R. (2003). *Journal of Applied Crystallography* **36**, 1455-1460.

Walker, L. J., Moreno, P. O., & Hope, H. (1998). *Journal of Applied Crystallography* **31**, 954-956.

Warkentin, M., Berejnov, V., Husseini, N. S., & Thorne, R. E. (2006). *Journal of Applied Crystallography* **39**, 805-811.

Weik, M., Kryger, G., Schreurs, A. M. M., Bouma, B., Silman, I., Sussman, J. L., Gros, P., & Kroon, J. (2001). *Acta Crystallographica Section D-Biological Crystallography* **57**, 566-573.

Weik, M., Vernede, X., Royant, A., & Bourgeois, D. (2004). *Biophysical Journal* **86**, 3176-3185.

Weik, M., Schreurs, A. M. M., Leiros, H. K. S., Zaccai, G., Ravelli, R. B. G., & Gros, P. (2005). *Journal of Synchrotron Radiation* **12**, 310-317.

Zasadzinski, J. A. N. (1988). *Journal of Microscopy-Oxford* **150**, 137-149.

Zeppezauer, M., Eklund, H., & Zeppezauer, E. S. (1968). *Archives of Biochemistry and Biophysics* **126**, 564-573.

Zheng, B., Roach, L. S., & Ismagilov, R. F. (2003). *Journal of the American Chemical Society* **125**, 11170-11171.

Zheng, B., Tice, J. D., Roach, L. S., & Ismagilov, R. F. (2004). *Angewandte Chemie-International Edition* **43**, 2508-2511.

Zheng, B., Gerdts, C. J., & Ismagilov, R. F. (2005). *Current Opinion in Structural Biology* **15**, 548-555.

CHAPTER 5

CRITICAL DROPLET THEORY FOR NUCLEATION OF CUBIC ICE IN AQUEOUS SOLTUTIONS

5.1 Introduction

The transformation of liquid water to crystalline ice is relevant to a wide range of scientific fields. It is central to cryopreservation of cells and tissues (Mazur, 1970), cryocooling of protein and virus crystals (Hope, 1988; Rodgers, 1994), or any field that concerns itself with cooling biological systems to freezing temperatures. Atmospheric science is affected by it because of its importance to cloud formation in the upper atmosphere, which has implications for climate change (Baker, 1997). Finally, it provides insight into nucleation and growth phenomena, which are of fundamental interest to science. Water is also an exceptional example in many ways, because of its many anomalous properties at low temperatures (Debenedetti, 2003).

Many studies have shed light on various aspects of the behavior of water below the freezing point, but there is still much work to be done. Water converts to cubic ice (ice Ic) very rapidly (in ~10 μs) near T = 200 K (Bartell & Huang, 1994), so many experimenters have found ways to increase the timescale (hopefully) without modifying the underlying phenomena to the point of irrelevance.

One important strategy is extrapolation from experimentally accessible temperature ranges. The nucleation and growth of the hexagonal form of ice (ice Ih) has been studied near the homogenous nucleation temperature of T ~ 240 K, where it occurs at

a manageable rate (Wood & Walton, 1970). As the temperature is lowered, the nucleation rate increases rapidly, appearing to diverge at T = 228 K (Pruppacher, 1995). It is thus questionable whether any extrapolation to temperatures below 228 K would be meaningful.

Amorphous solid water (glassy water) can be prepared by a variety of methods (Angell, 2004), and it is metastable on laboratory timescales below T ~ 150 K (Hage *et al*., 1994). Extrapolations to higher temperatures can provide additional information. It is important to note that the phase of crystalline ice that is formed at these low temperatures (and near ~ 200 K) is the cubic form (ice Ic). Given enough time (and a large enough volume), ice Ic will convert to ice Ih, but ice Ic forms comparatively more quickly, and can grow from a smaller nucleus (Johari, 2005). For the purposes of this section, we will neglect the various differences that can exist between different forms of amorphous water.

Another way to access the first stages of ice formation is by increasing the pressure. In fact, at large enough pressures ice formation can be completely suppressed in pure water. The same is also true of adding solutes (such as salts, sugars, polymers, alcohols, etc.). This is perhaps not surprising, as there is a correspondence between increased pressure and increased solute concentration in the thermodynamic phase diagram of water (Koop, 2000).

Finally, ice formation can be slowed (or suppressed completely) by confining water to ~ nm-sized pores. Below a certain pore size, only cubic ice is observed, and at even smaller pore sizes, ice formation is completely suppressed (Rault *et al*., 2003).

Based on these studies, it is generally accepted that ice Ic is the kinetically favored form of ice, which has a stable nucleation radius of ~1 nm, while Ih is the thermodynamically favored form, requiring a considerably larger nucleus. If the conditions are almost (but not quite) sufficient to suppress ice formation entirely, ice Ic forms, while ice Ih is found under more "natural" conditions. As a result, understanding ice formation in general can be broken into two parts: first, an ice Ic nucleus forms from liquid water and grows, second, the nucleus reaches a threshold size and converts to ice Ih given sufficient time.

The goal of this study is to understand the first stage of ice formation: the nucleation of ice Ic. We use solutes to slow the formation of ice to a measurable range, and the rate of formation is determined for a range of solute concentrations and for a variety of solutes. The rate is found to depend exponentially on the solute concentration, with a different characteristic for each solute.

We use critical droplet theory to understand the exponential dependence of the nucleation rate, by taking into account the osmotic pressure of the solution. This approach is able to explain the observed dependence of nucleation rate on concentration, giving a reasonable value for the one free parameter: the critical radius.

Unfortunately, when different solutes are compared, they each predict a different value for the critical radius, and there is a correlation between solute size and predicted critical radius. Two additions to the theory are discussed which can explain this inconsistency. First, the differing sizes of the solutes in solution cause them to probe different "apparent" critical radii. Second, there is the enthalpic contribution to the free energy, which becomes dominant for large solutes.t

5.2 Experimental Methods

The rate of ice formation in each aqueous solution was determined by measuring the critical cooling rate (CCR) above which no ice was observed on cooling in liquid nitrogen. Below the critical rate, the sample turns opaque on cooling, indicating the formation of polycrystalline ice. As the rate is increased, an abrupt transition to transparent samples is observed.

It has been shown that this transition is abrupt, and corresponds to a transition in the X-ray diffraction patterns obtained from the frozen samples (Berejnov *et al*., 2006). Clear samples show diffuse rings characteristic of a glassy state, whereas opaque samples show a sharp ring characteristic of a crystalline powder. The method used to measure the CCR has been described elsewhere (Warkentin *et al*., 2008), and will be summarized here.

Briefly, plastic tubing of varying diameter was filled with the solution of interest and plunged into liquid nitrogen. The state (crystalline or amorphous) was determined visually by noting the transparency or opacity of the frozen sample. Separately, the cooling rate in each piece of tubing was determined using tubes filled with a 60 % (w/v) solution by threading a thermocouple down the center of the tube and plunging into liquid nitrogen.

For each tubing diameter, solutions in 2 % (w/v) increments were sequentially frozen until the transition was observed, and the cooling rate in that tubing diameter was recorded as the CCR for that concentration. Data for glycerol were taken from

Warkentin *et al*., 2008, and it should be noted that they were in agreement with differential scanning calorimetry measurements from an earlier study in a higher concentration range (Sutton, 1991). Additional data were obtained for ethylene glycol, poly-(ethylene glycol) 200, dextrose, trehalose, dimethylsulfoxide (DMSO), sodium chloride, methanol, ethanol, isopropanol, secondary butanol, and tertiary butanol. Representative data are shown in Figure 5.1.

Two features are obvious in the figure. First, each solute shows an exponential dependence of CCR on concentration. Second, each exponential extrapolates to a value between 10^5 and 10^6 K/s for pure water, in agreement with the estimated value for that quantity (Bruggeller & Mayer, 1980). This suggests that the CCR is in fact exponential over the entire range of concentrations in which ice forms for every solute tested.

5.3 Discussion

In Figure 5.1, it is clear that there is a simple exponential dependence of CCR on concentration for every solute tested. This dependence appears to extend over the entire range of concentrations. This suggests that a simple theory, encompassing all solutes and concentrations, can be used to understand the mechanism of ice formation in aqueous solutions. Since the exponentials extrapolate to the correct value for pure water, the theory should encompass pure water as well.

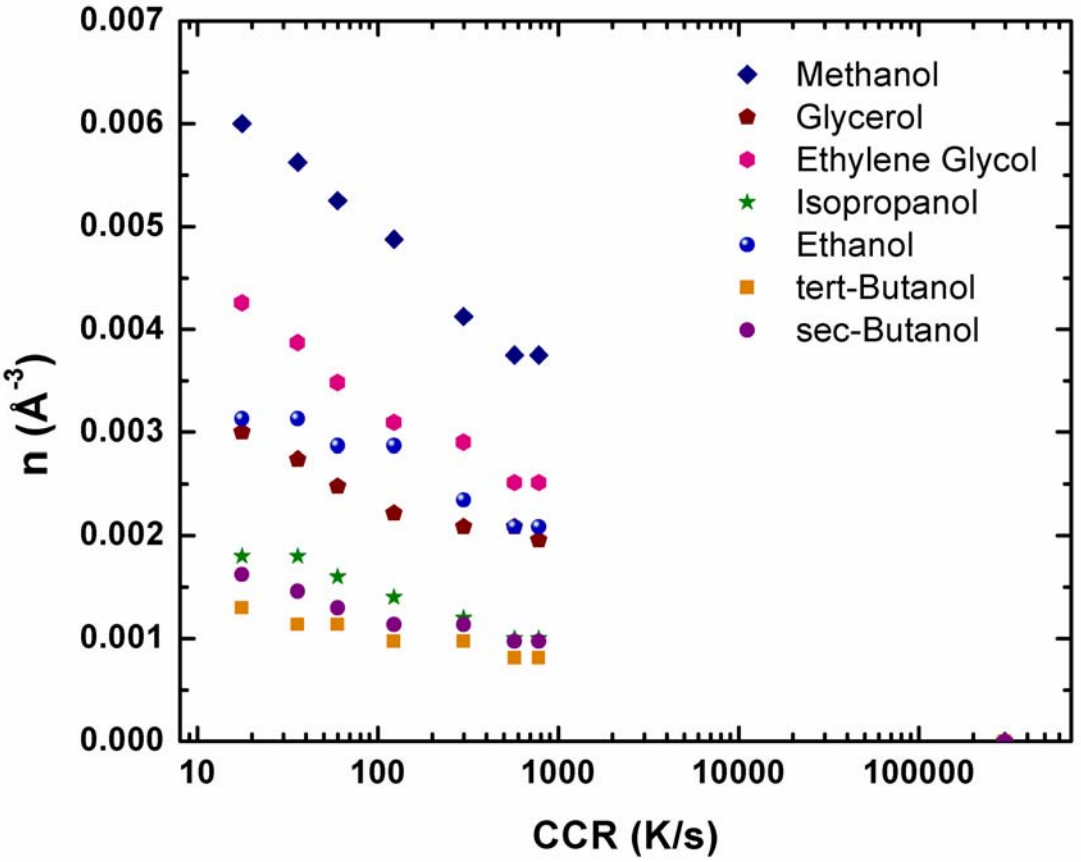

Figure 5.1

The dependence of critical cooling rate (CCR) on solute concentration is shown for a range of representative solutes. In each case there is an exponential dependence of CCR on solute concentration.

5.3.1 Nucleation vs. growth

It is not immediately clear whether nucleation or growth is the rate limiting step determining the CCR. We know, however, that as the cooling rate is increased there is an abrupt (discontinuous) jump in both optical clarity and X-ray diffraction pattern. If growth was the limiting step, we would expect to see a smooth transition from opaque to transparent samples, as well as a smooth transition from amorphous-like to crystalline-like diffraction patterns.

In Berejnov *et al*., 2006, diffraction patterns were recorded at concentrations either just above or just below the opaque-to-transparent transition. They show that the width of the primary diffraction peak increases by ~5 times on going through the transition. Since samples with the narrower diffraction peak were also opaque, this suggests the presence of ~ 100 nm crystallites, 1000 times larger than the critical nucleation radius of cubic ice. What this means is that if a critical nucleus forms, it grows to become very large.

One reason that this is sensible is that as the nucleus grows, it releases heat. Since the cooling rate is not controlled (as in scanning calorimetry), this results in a much lower cooling rate than would exist in the absence of a phase transformation. Because of this effect, our experiment is highly sensitive to the formation of ice: if any forms at all, the heat released causes much more to form.

Based on this reasoning, we will consider nucleation when modeling the data in Figure 5.1.

5.3.2 Critical droplet theory

Even if a new phase is energetically favorable, it will not necessarily form. The system must cross an energy barrier, which is only possible when the barrier height is of the same order of magnitude as the thermal energy. In case of phase transformations, the energy barrier is often a barrier to the formation of a sufficiently large cluster of the new phase, so that it is equally likely to grow as it is to shrink. This cluster is called the *critical nucleus*. A very simple model describing this process is *critical droplet theory*, or *classical nucleation theory* (Bradley, 1951; Buckle, 1961) as follows.

The new phase is assumed to have a lower free energy ρ, per unit volume than the original phase. This is what drives it to form in the first place. The barrier to formation results from a free energy cost, σ, per unit area at the interface between the two phases. Thus the total free energy of the formation of a cluster of the new phase with radius R is given by

$$\Delta G^0 = -4/3\,\pi\rho R^3 + 4\pi\sigma R^2 \tag{5.1}$$

The free energy has a maximum for a cluster of radius

$$R_c^0 = 2\sigma/\rho \tag{5.2}$$

The free energy required to cross this maximum is the nucleation barrier. The rate of crossing this barrier (in this case the nucleation rate) is proportional to the Boltzmann factor associated with this energy:

$$K_0 \sim e^{-\Delta G_c^0 / k_B T} \tag{5.3}$$

In our model, the free energy is modified to include the energy cost of excluding all solute molecules from the critical nucleus. This cost is simply the osmotic pressure of the solute:

$$\Delta G^n = -\frac{4}{3}\pi\rho R^3 + 4\pi\sigma R^2 + \frac{4}{3}\pi n k_B T R^3 \tag{5.4}$$

where *n* is the number density of solute molecules. The critical radius is modified to

$$R_c^n = 2\sigma / \rho - n k_B T \tag{5.5}$$

and the barrier height is:

$$\Delta G_c^n = \Delta G_c^0 + V_c^0 n k_B T + O(n^2) \tag{5.6}$$

where V_c^0 is the volume of the critical nucleus at zero concentration. The nucleation rate at an arbitrary number density of solute can then be expressed as

$$K_n = K_0 e^{-V_c^0 n} \tag{5.7}$$

This result implies that the concentration dependence of the nucleation rate is related to the critical radius of pure water. Equation (5.7) can be fit to the data in Figure 5.1 to give a value of V_c^0 for each solute. The corresponding critical radii range from 7.3 to 12.2 Å, in good agreement with the best estimate available in the literature of 10 ± 5 Å (summarized in Zasetski *et al*., 2009). This indicates that the simple treatment just described is a plausible explanation for the strong concentration dependence of the nucleation rate.

$O(n^2)$ corrections to the free energy can be ruled out based on Figure 5.1. If the various terms of that order (arising from the expansion that led to (5.6), the excluded volume of the solute, and van der Waals attraction between solute molecules) are of non-negligible magnitude, they must cancel out so that the sum is negligible, because the data are well fit by straight lines. If second-order polynomials are fit instead, the coefficients on the *O(n)* terms are essentially unchanged, giving essentially no correction to the predicted value of V_c^0.

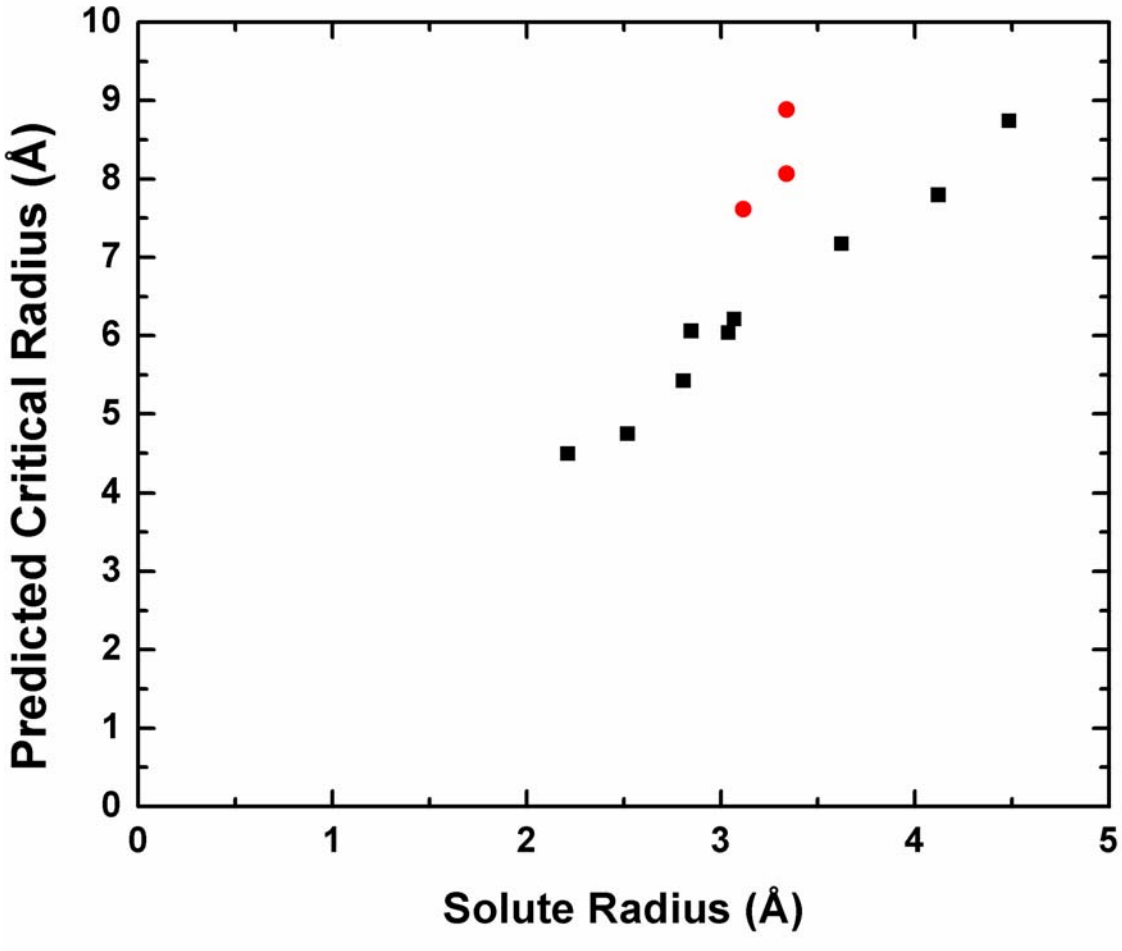

Figure 5.2

The critical droplet theory of equation (5.8) predicts a critical radius that depends strongly on solute radius, even after the solute radius has been taken into account. The points in red are, from top to bottom, tertiary butanol, secondary butanol, and isopropanol. One interpretation is that their non-polar methyl groups order a layer of water around them of ~ 1 Å thickness, giving them a larger effective size.

5.3.3 Modifications to the simple theory

The most obvious correction that can be made to the model is to include the non-zero size of the solute molecules. This is done by requiring that they be excluded from a sphere of radius $R + R_s$ where R_s is the radius of a sphere with volume equal to that occupied by one molecule in the pure substance. (This is equal to the molar volume divided by Avogadro's number.) The resulting free energy is

$$\Delta G^n = -\tfrac{4}{3}\pi\rho R^3 + 4\pi\sigma R^2 + \tfrac{4}{3}\pi n k_B T \left(R + R_s\right)^3 \qquad (5.8)$$

The result of the calculation analogous to equations (5.5) through (5.7) is simply that the critical radius is overestimated by precisely R_s. The range of predicted critical radii is reduced to 8.7 to 4.8 Å. This correction is plausible because larger molecules do give larger estimates for V_c^0, but there is still a residual dependence of predicted critical radius to solute radius as shown in Figure 5.2. Note that isopropanol, secondary butanol, and tertiary butanol appear to have larger radii than would be predicted from their molar volume. One explanation for this is that they are largely non-polar, and so they "order" a ~ 1 Å layer of water. We note that secondary and tertiary butanol were barely soluble enough to make the measurements, and so they may not be valid for that reason as well.

Another important correction to the theory is to include the non-zero heat of mixing of the solute *at the nucleation temperature*, that is, ~200 K. Of course that quantity is likely to be impossible to measure, but it is worthwhile to explore the implications of including it in the theory. The free energy would be:

$$\Delta G^n = -\tfrac{4}{3}\pi\rho R^3 + 4\pi\sigma R^2 + \tfrac{4}{3}\pi n(k_B T + \Delta L / N_A)R^3$$

Where ΔL is the enthalpy of mixing at ~200 K, per mole of solute, and N_A is Avogadro's number. The result is that the predicted critical radius is off by a factor

.

$$(1+\frac{\Delta L / N_A}{k_B T})^{1/3}$$

which is greater than one for positive (exothermic) heats of mixing.

In the case of glycerol, ethylene glycerol, and 1,2-propanediol, the heat of mixing has been taken into account for the study of ice nucleation, albeit in an unrelated regime, by Boutron (1984). His interest in the heat of mixing was simply to correctly estimate the amount of ice that had formed in calorimetry. In all three cases, the heats of mixing are positive, and they lie in the range ~5 - 15 kJ/mol, and depend on solute concentration and temperature.

The inclusion of the heat of mixing in the theory can explain the variation in predicted critical radii apparent in Figure 5.2. First, a heat of mixing of ~4 kJ/mol is enough to increase the apparent critical radius by 50 %, so the effect is large enough to explain the variation. Second, the effect will be more pronounced for the larger solutes, since the heat of mixing, will be larger *per mole*. This could explain the correlation between solute size and apparent critical radius. However, with no detailed information on the heats of mixing at that temperature, it is impossible to correct the data for this effect.

5.3.4 Comparison to previous work

Previous attempts to understand the critical cooling rates of glass forming substances have used semi-empirical correlations. Recently, a large study correlated data for nearly 100 different glass forming systems (Lu & Liu, 2003). Their finding was that

$$CCR \sim Ae^{-b\gamma} \qquad \gamma = \frac{T_x}{T_g - T_l} \tag{5.9}$$

where T_x, T_g, and T_l are the devitrification temperature, glass temperature, and melting temperature, respectively. A and b are empirical constants that depend on the class of glass forming system under consideration. (In their study, the three classes are metallic glasses, glassy oxides, and cryoprotective aqueous solutions.) For cryoprotective aqueous solutions, $A = 5 \bullet 10^{10}$ K/s , and $b = -46.804$.

(We note that the Lu & Liu study made an error of factor 60 for the cryoprotective solutions, because the references they cite all give CCR in K/min, whereas they used K/s without making this correction, i.e. $A = 5 \bullet 10^{10}$ K/min , which we will use.)

Data for the glass and melting temperatures of glycerol solutions are available over a wide range of concentrations (MacKenzie, 1977; Harran, 1978), however, devitrification temperatures are only available for concentrations that can be vitrified in sufficient volume for use in scanning calorimetry. Values of T_x are available at 57 and 63 % (w/v), considerably above the concentration range studied here (Hey & MacFarlane, 1996). Nevertheless, we can obtain a very crude estimate for T_x from the data available by simply assuming that there is a fixed temperature difference between T_x and T_g of 9 degrees (the value at 57 % (w/v) glycerol). As we will show, the error

resulting from this assumption is irrelevant. The data used to calculate γ are shown in Figure 5.3.

The predicted values of CCR are shown in Figure 5.4, along with the measured ones, for glycerol solutions. It is clear that the Lu & Liu correlation works only in the limit of highly concentrated solutions. We point out that the 25 data points in their study all have CCR in the range $10^{-1} - 10^{1}$ K/s, corresponding to very high concentrations of cryoprotectant.

Of course, the most spectacular failure of the Lu & Liu correlation is for pure water, for which they would predict a CCR of 30 K/s, at least four orders of magnitude too low. This is most likely the explanation for the failure of the correlation to fit our data as well: as the system becomes closer to the pure water limit, the discrepancy grows. It should also now be clear that the crude estimate of T_x used in Figure 5.3 is irrelevant to that conclusion.

5.4 Conclusion

We have made critical cooling rate (CCR) measurements on a wide range of aqueous solutions, at cooling rates up to 2 orders of magnitude larger than in previous studies. The result is an unmistakable exponential dependence of CCR on solute concentration, which appears to be valid all the way to zero solute concentration (pure water). A simple theory which takes account of the osmotic pressure of the solution can explain the exponential dependence, however it is not completely satisfactory because of a remaining correlation of solute size to predicted critical nucleation radius.

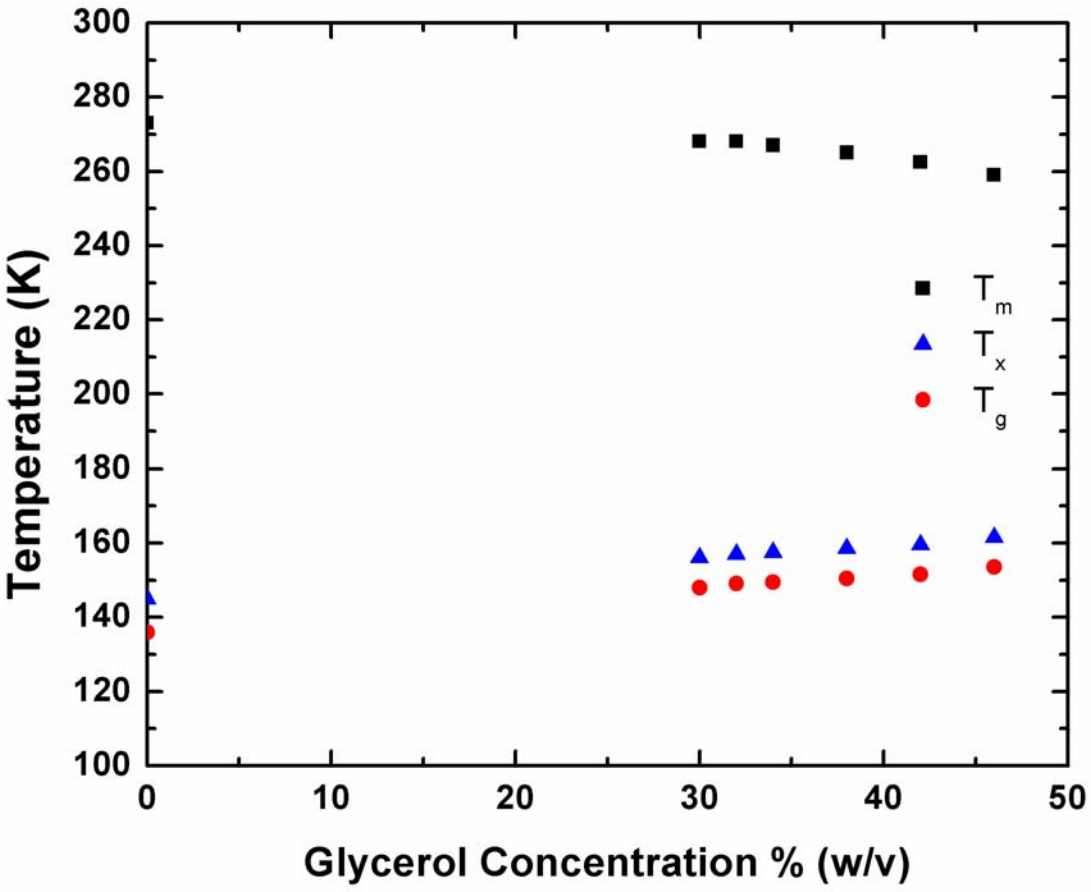

Figure 5.3

The values for the melting temperature, glass temperature, and devitrification temperature used to compute the critical cooling rates predicted by the correlation of Lu & Liu, 2003 are shown.

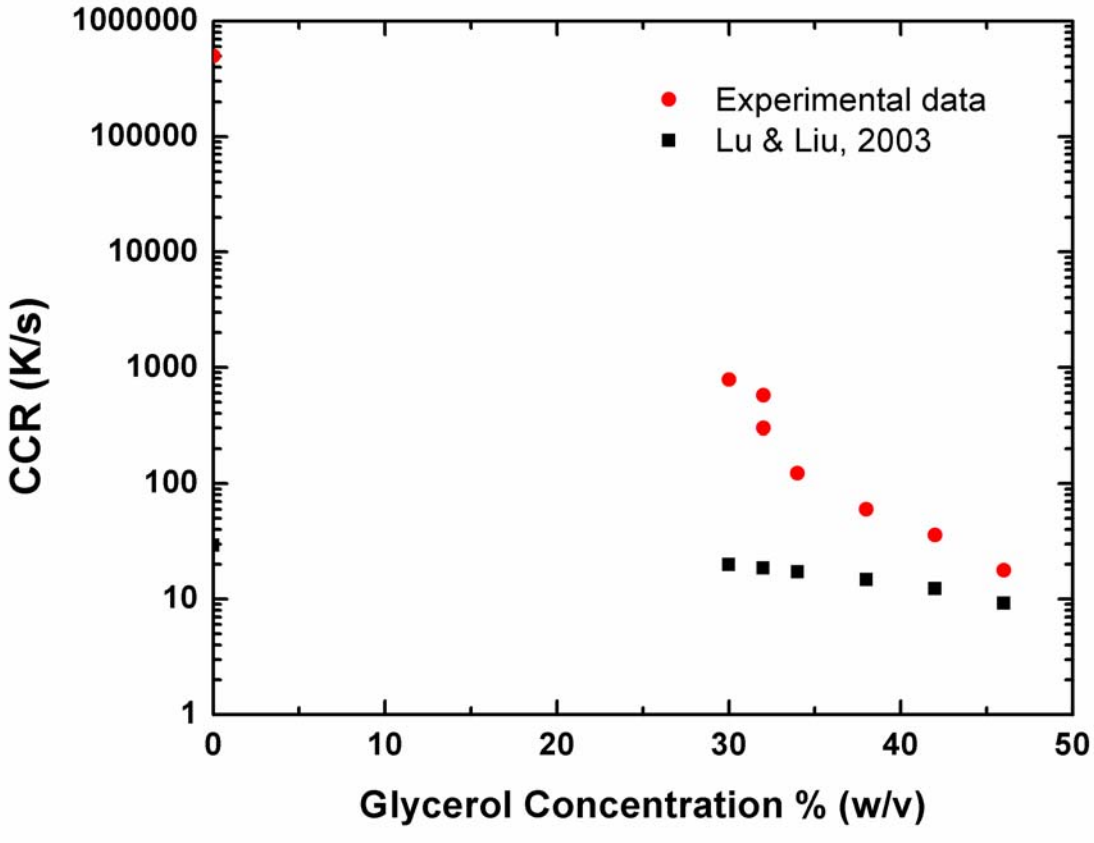

Figure 5.4

A comparison between the measured critical cooling rates for each glycerol concentration and values predicted by the correlation of Lu & Liu, 2003 is shown. The correlation was formulated based on data for solutions of concentrations greater than 50 % (w/v), and it clearly fails to predict critical cooling rates in solutions with higher water content. All of the data on which the Lu & Liu correlation are based are at cooling rates under 10 K/s, where the present data come closest to agreeing with the correlation.

Nevertheless, the critical radius predicted for each solute is in good agreement with the established value in the literature.

Compared to an empirical correlation based on scanning calorimetry, this theory connects the CCRs of highly concentrated aqueous solutions (concentrations used in scanning calorimetry) to the CCR of pure water. The failure of the empirical correlation to encompass the data for pure water underscore the importance of a new approach to understanding glass formation in aqueous systems.

REFERENCES

Angell, C. A. (2004). *Annual Review of Physical Chemistry* **55**, 559-583.

Baker, M. B. (1997). *Science* **276**, 1072-1078.

Bartell, L. S. & Huang, J. F. (1994). *Journal of Physical Chemistry* **98**, 7455-7457.

Debenedetti, P. G. (2003). *Journal of Physics-Condensed Matter* **15**, R1669-R1726.

Hage, W., Hallbrucker, A., Mayer, E., & Johari, G. P. (1994). *Journal of Chemical Physics* **100**, 2743-2747.

Hope, H. (1988). *Acta Crystallographica Section B-Structural Science* **44**, 22-26.

Johari, G. P. (2005). *Journal of Chemical Physics* **122**.

Mazur, P. (1970). *Science* **168**, 939-&.

Pruppacher, H. R. (1995). *Journal of the Atmospheric Sciences* **52**, 1924-1933.

Rodgers, D. W. (1994). *Structure* **2**, 1135-1140.

Wood, G. R. & Walton, A. G. (1970). *Journal of Applied Physics* **41**, 3027-&.

Rault, J., Neffati, R., & Judeinstein, P. (2003). *European Physical Journal B* **36**, 627-637.

Sutton, R. L. (1991). *Journal of the Chemical Society-Faraday Transactions* **87**, 101-105.

Berejnov, V., Husseini, N. S., Alsaied, O. A., & Thorne, R. E. (2006). *Journal of Applied Crystallography* **39**, 244-251.

Warkentin, M., Stanislavskaia, V., Hammes, K., & Thorne, R. E. (2008). *Journal of Applied Crystallography* **41**, 791-797.

Turnbull, D. & Fisher, J. C. (1949). *Journal of Chemical Physics* **17**, 71-73.

Bradley, R. S. (1951). *Quarterly Reviews* **5**, 315-343.

Lu, Z. P. & Liu, C. T. (2003). *Physical Review Letters* **91**.

Mackenzie, A. P., Derbyshire, W., & Reid, D. S. (1977). *Philosophical Transactions of the Royal Society of London Series B-Biological Sciences* **278**, 167-&.

Hey, J. M. & Macfarlane, D. R. (1998). *Cryobiology* **37**, 119-130.

Zasetsky, A. Y., Petelina, S. V., & Svishchev, I. M. (2009). *Atmospheric Chemistry and Physics* **9** , 965-971.

CHAPTER 6

SLOW COOLING OF PROTEIN CRYSTALS

6.1 Introduction

X-ray crystallography performed on crystallized proteins is an essential tool in modern structural biology. The structural data obtained depend upon the protein crystal's temperature and thermal history. Protein crystals are typically grown at temperatures between 277 and 300 K, and then flash cooled to T=100 K to reduce structural damage caused by the X-rays (Hope, 1988; Hope, 1990; Rodgers, 1994; Garman & Schneider, 1997; Garman, 1999; Pflugrath, 2004). The cooling process increases the amount of disorder within the crystal, most clearly manifested in large increases in mosaicity, and this reduces the quality of the information about molecular structure that can be obtained (Low *et al*., 1966; Singh *et al*., 1980).

Why and how cooling creates disorder in protein crystals is still not understood, but a growing body of work has addressed this problem (Walker *et al.,* 1998; Teng & Moffat, 1998; Snell *et al.*, 2002; McFerrin & Snell, 2002; Juers & Matthews, 2004a; Gakhar & Wiencek, 2005). Crystal order at T=100 K has been examined using a variety of methods including X-ray crystallography and X-ray topography (Kriminski *et al*., 2002; Lovelace *et al.*, 2006). Factors affecting this order including cryoprotectant type and concentration (Mitchell & Garman, 1994; Juers & Matthews, 2004b), flash cooling protocol (Warkentin *et al*., 2006), application of high pressures during cooling (Kim *et al*., 2005), and post-cool crystal annealing (Harp *et al.,* 1998, 1999; Kriminski *et al*., 2002) have been examined.

Although nearly all protein crystallography is performed at T=100 K, X-ray data collection at higher temperatures—especially between the solvent glass transition temperature (~150-180 K) and room or body temperature—can provide information about the protein's conformation, energy landscape and dynamics useful in understanding protein function. A few studies have examined how protein and crystal structure evolve with temperature, usually by flash cooling individual crystals from room temperature to different final temperatures (Frauenfelder *et al.*, 1979; Singh *et al.*, 1980; Chong *et al.*, 2001; Edayathumangalam & Luger, 2005). These studies have required large (~50%) cryoprotectant concentrations to prevent crystalline ice formation below T~270 K, and these may have affected the protein structure and its temperature evolution. Changes within individual flash-cooled crystals upon warming from T=100 K toward 200 K have also been explored (Weik *et al*., 2001; Weik *et al*., 2005).

Collecting usable diffraction data near T=200 K has proven particularly difficult (Frauenfelder *et al.,* 1979; Tilton *et al*., 1992; Rasmussen *et al.,* 1992; Kurinov & Harrison, 1995). For example, Tilton *et al*. reported that at T=200 K a ribonuclease A crystal rapidly became opaque and ceased to diffract, despite the use of 50 % (v/v) MPD. The only successes at this temperature used a methanol concentration of 75 % (v/v) (Singh *et al*., 1980), or used crambin, an unusually small and dry protein crystal system (Teeter *et al*., 2001).

The temperature-dependent properties of protein crystals depend upon both the protein and the solvent. The protein molecules are fully (or nearly fully) hydrated, and their packing leaves solvent-filled channels and pockets that are typically 15 – 30 Å in size

(and sometimes much larger.) Protein crystals are thus protein-solvent composites, consisting of a regular lattice of protein molecules interwoven with a lattice of solvent-containing channels. The temperature-dependent properties of the protein, the solvent and their interaction must all be important in determining the temperature-dependent properties of protein crystals.

Here we extend previous work by measuring the evolution of the diffraction properties of a single protein crystal during cooling from 300 K to 100 K. We demonstrate that crystals can be successfully cooled to 100 K without crystalline ice formation using cooling rates of ~0.1 K/s, 10^3 to 10^4 times smaller than in previous studies, and even in the absence of penetrating cryoprotectants. Successful slow cooling requires careful removal of all external solvent, which otherwise will crystallize, generating intense ice diffraction rings that obscure protein crystal diffraction, drawing solvent out of the crystal (Weik *et al.,* 2001), and seeding ice crystal growth within the crystal that degrades crystalline order. Diffraction data can be collected continuously during cooling, so that the evolution of crystal, protein and solvent properties can be characterized as a function of temperature. Our method should be of particular use in probing conformation changes such as in "kinetic crystallography", where enzymatic function is induced in the crystalline state and temperature variations can be used to trap reaction intermediates (Bourgeois & Royant, 2005; Colletier *et al.,* 2008, Bourgeois & Weik, 2009). The present data also provides insight into the protein glass/dynamical transition and into why crystal mosaicity increases during cooling.

6.2 Methods

Tetragonal crystals of thaumatin (MW = 24,000 Da, unit cell dimensions $a = b = 58$ Å, $c = 151$ Å, 56 % solvent, 25-35 Å diameter solvent channels) were grown according to a standard recipe (McPherson, 1999). Protein from Sigma (Product no. T 7638, Lot no. 108FO299) was dissolved in 100 mM potassium phosphate buffer at pH 6.8 to a final concentration of 25 mg/ml. A well solution of 1.5 M sodium potassium tartrate was prepared in the same buffer. In each well of a 24-well plate, a glass cover slip with a hanging drop formed by mixing 5 µl of protein solution and 5 µl of well solution was suspended above 500 ml of well solution, and the well sealed with vacuum grease.

For the cryoprotectant soaks, solutions with glycerol concentrations of 10%, 20%, 30% and 40% (w/v) were prepared by mixing glycerol and well solution. Crystals were serially soaked in solutions of increasing glycerol concentration until the desired final concentration was reached. The crystal was allowed to equilibrate at intermediate concentrations for ~ 1 minute and at the final concentration for between 5 and 10 minutes before further preparation.

Bulk solvent surrounding a crystal rapidly crystallizes during cooling through the T=240 to 220 K temperature range, and must be completely removed for successful slow cooling and X-ray data collection. Figure 6.1 illustrates the method used to prepare crystals for slow cooling. ~300 µm crystals were transferred from their mother liquor (the drop from which the crystal grew) or from a cryoprotectant soak to a large drop of Paratone-n oil (Hampton Research, Aliso Viejo, CA, USA) (Figure 5.1a) or NVH oil (Cargille Laboratories, Cedar Grove, NJ, USA), using a MicroMount

(Mitegen LLC, Ithaca, NY, USA) to minimize the transfer of excess mother liquor. The mixture was stirred so that the crystals shed their surrounding solvent in a trail of emulsified bubbles (Figure 5.1b). The crystals were then transferred to a fresh oil drop and the process repeated until solvent trails were no longer visible. Pockets of solvent often remained stuck to the crystal surface (Figure 5.1c), and were scraped off using a MicroChisel (Mitegen LLC, Ithaca, NY, USA).

When this process was properly executed, the facets of the crystal became nearly invisible (Figure 5.1d). The change was unmistakable and did not depend upon illumination or magnification. We interpret this abrupt change in the appearance of the crystal as follows. The refractive index of the solvent varies between ~1.33 (water) and ~1.38 (40% glycerol); the refractive index of the crystal is likely near n~1.56 measured for tetragonal lysozyme (Cervelle *et al*., 1974); and the refractive index for Paratone oil is likely near the n=1.52 of NVH oil (Cargille Labs, Cedar Grove, NJ, USA). If there is a layer of solvent coating the crystal, it creates two interfaces — oil-solvent and solvent-crystal — with large (Δn~0.15) refractive index steps. Since the reflection coefficient of an interface is proportional to the refractive index difference, light incident from either the oil or the crystal is strongly reflected at both interfaces. When all the solvent has been removed (or at least when its remaining thickness is much smaller than the illuminating light wavelength ~400 nm), the crystal is nearly indexed matched with the oil, little reflection occurs at the oil-crystal interface, and the crystal becomes nearly invisible. This simple visual test thus provides a very sensitive probe of residual solvent.

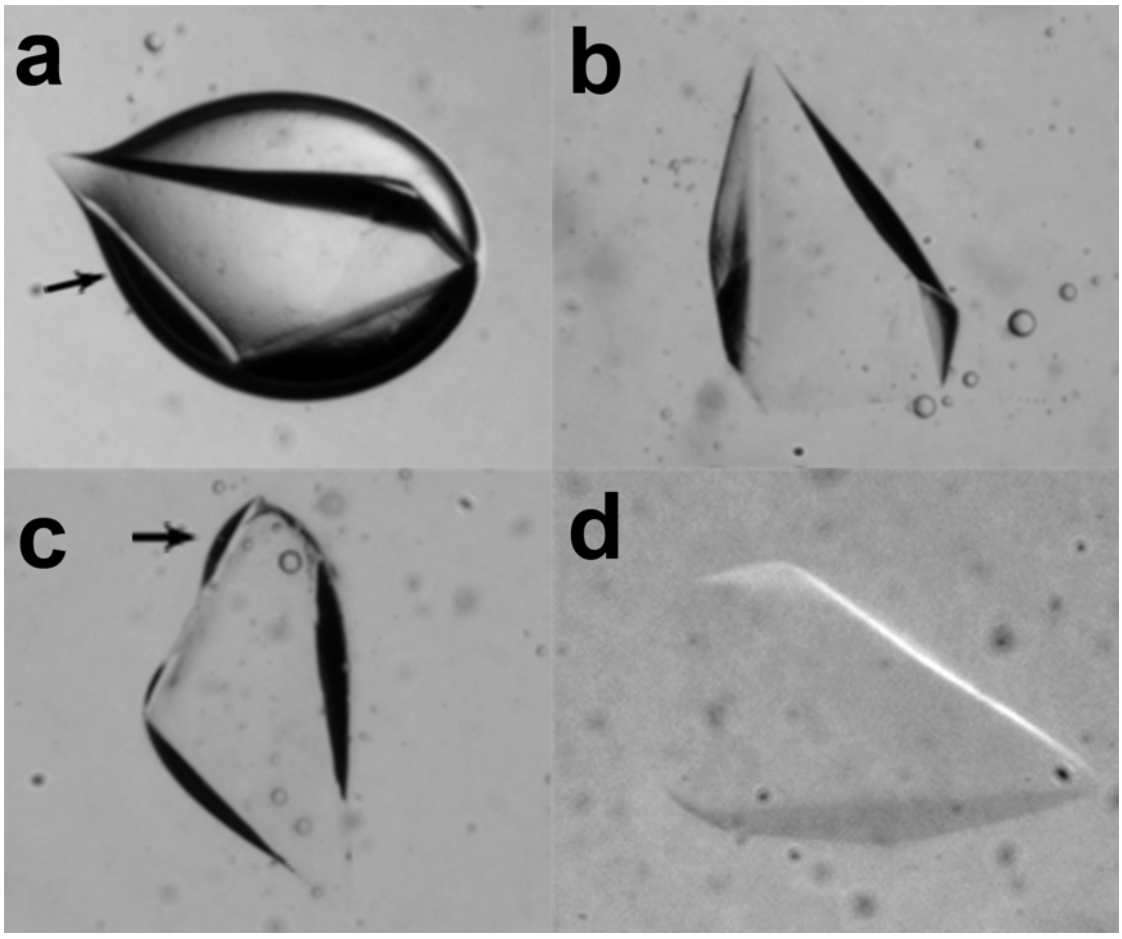

Figure 6.1

Preparation of a thaumatin crystal for slow cooling. **a)** The crystal and surrounding mother liquor are transferred to a large drop of Paratone-n oil. **b)** The crystal is stirred to remove most of the external mother liquor. **c)** The remaining mother liquor, which tends to form beads (indicated by the arrow), is scraped off with a MicroChisel. **d)** When all the external solvent has been removed, the crystal becomes nearly invisible in the oil, indicating that the solvent layer is no thicker than the wavelength of illuminating light. The actual solvent layer is likely much thinner, because any significant layer is unstable to beading on the surface.

A crystal thus prepared was captured together with a thick surrounding layer of Paratone-n oil (to prevent dehydration during the initial stages of the experiment) in a 500 μm – 1 mm nylon Cryoloop (Hampton Research, Aliso Viejo, CA, USA) (Figure 6.2). The sample was immediately placed on a goniometer head and a T=300 K nitrogen gas stream produced by an Oxford Cryosystems 600-Series Cryostream was directed at it. The Cryostream was programmed to cool the sample at 0.1 K/s, and the X-ray data collection software programmed to repeatedly collect five 1° oscillation frames over the same five-degree wedge. A computer running Cryopad software (Oxford Cryosystems) and connected to the Cryostream controller logged the gas stream temperature, so that the temperature for each X-ray frame could be obtained by matching time stamps in the frame file header and in the temperature log file. Cooling and data collection continued until the Cryostream temperature reached 100 K, 34 minutes after the start of cooling.

To verify that radiation damage did not significantly affect our results, the same X-ray dose was delivered as during cooling from T=300 K to 100 K, but with the temperature held fixed at 300 K. Radiation damage for a given dose is approximately 50 - 100 times larger at 300 K than at 100 K (Kmetko *et al*., 2006), so that the radiation damage measured at 300 K sets an upper bound on the damage incurred during cooling experiments. The dose was measured using an ion chamber at the end of the collimator, which was calibrated at the beginning and end of the experiment. The delivered dose increased the unit cell volume by 0.02 %, the mosaicity by 0.04°, and the B-factor by 1.5 $Å^2$. These changes are small compared with those induced by cooling.

This control experiment for radiation damage also serves as a control for dehydration, since water's vapor pressure and the dehydration rate are largest at T=300 K; they are insignificant at (and below) T=250 K, where the vapor pressure is a factor of 35

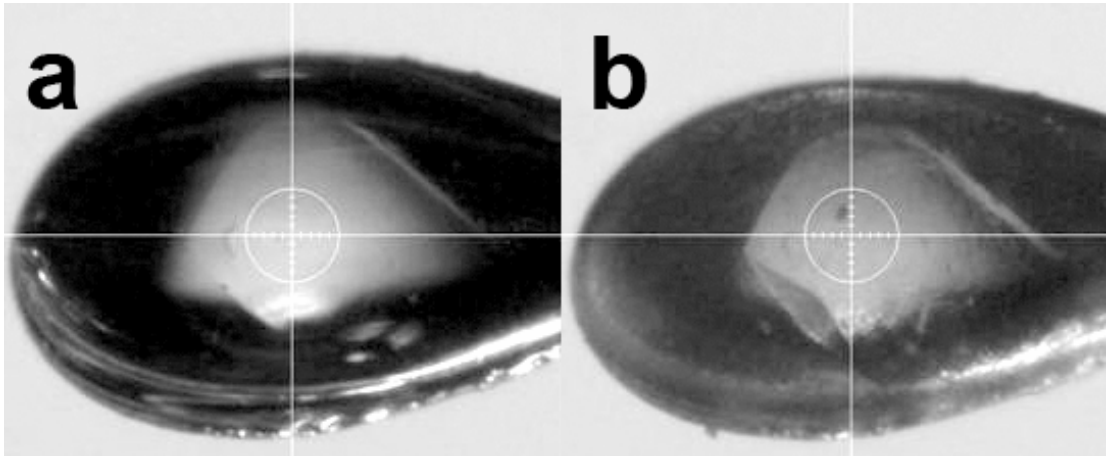

Figure 6.2

A thaumatin crystal prepared as in Figure 6.1 and then mounted in a 1 mm Cryoloop with a large drop of oil, at (a) T=300 K and (b) after slow cooling to T=100 K. During slow cooling the surrounding oil becomes cloudy, indicating formation of a crystalline phase (see text). The thick oil layer prevents crystal dehydration.

smaller. Dehydration decreases the unit cell volume and usually has little effect on mosaicity except at large dehydrations (Kriminski *et al*., 2001). No evidence of dehydration-induced cell volume changes were observed in our control experiment, or for a sample held for one hour at T=300 K before irradiation. The thick (~500 μm) Paratone-n layer surrounding the crystal provides an excellent vapor barrier.

Several other approaches were explored before settling on the sample preparation protocol described above. Mother liquor surrounding the crystal can be removed by allowing it to slowly evaporate either in air or (for much slower removal) through a very thin layer of oil while the sample is observed under a microscope. Unlike with direct mechanical removal of the mother liquor, evaporation leaves behind non-volatile salts that can crystallize, producing diffraction that interferes with that from the protein. For protein crystals grown from high-salt mother liquors (e.g., ribonuclease A grown in 4 M sodium chloride), salt crystal diffraction is observed on cooling even when surrounding mother liquor is mechanically removed, possibly because cooling decreases the salt's solubility below the crystal's initial salt concentration.

The high-viscosity Paratone-n oil used to remove mother liquor from the crystal surface and prevent dehydration also helps prevent sample motion during data collection at higher temperatures. Thick layers of less viscous oils (e.g., mineral and perfluoro(poly)ether oils) allow too much motion. Even with Paratone-n oil, the first few high-temperature X-ray frames sometimes indicated large (~5 degree) crystal motions. Pausing for ~5 minutes after mounting, centering and rotating the sample to the intended data collection angle before collecting frames minimized these motions.

Paratone-n oil has one significant disadvantage that was not recognized until after the bulk of our data collection was complete. As will be discussed later, when slowly cooled to T~255 K, a small fraction of the oil forms a microcrystalline phase that produces two sharp diffraction rings at 4.46 and 3.96 Å. These rings can be avoided either by rapidly cooling to below T255 K, or by using NVH immersion oil (Cargille

Labs, Cedar Grove, NJ, USA), which is also highly viscous but does not crystallize at cooling rates of 0.1 K/s (data not shown.)

Another approach to preventing dehydration during slow cooling is to enclose the sample together with a plug of mother liquor in MicroRT tubing (Mitegen, Ithaca, NY, USA) or in a glass X-ray capillary. Thick oil layers and associated crystal slippage can be eliminated. Using a liquid plug with a vapor pressure slightly lower than that of the mother liquor, the water surrounding the crystal can be evaporated without excessively dehydrating the crystal, eliminating the need for mechanical solvent removal. However, because the tubing/capillary length is comparable to or larger than the diameter of the Cryostream's gas stream, ice crystals tend to condense from the ambient air onto tubing outside the stream. Large temperature gradients across the tubing drive transport and condensation of water from the warmer liquid plug onto the colder sample, and this water eventually crystallizes. These difficulties can be overcome by expanding the cold gas stream or by shortening the tubing so that the tubing fits entirely within the constant-temperature portion of the stream.

X-ray data were collected at beam line A1 of the Cornell High-Energy Synchrotron Source (CHESS) by a Quantum 210 detector (ADSC, Poway, CA) running in binned mode using ADSC Quantum data collection software. Each five-degree wedge of data was independently analyzed using Denzo and Scalepack (Otwinowski & Minor, 1997) to determine unit cell parameters, mosaicity and Wilson B-factor. The Wilson B-factor was determined by a fit to the intensity *vs*. resolution data in the output of Scalepack, with a low-resolution cutoff of 4 Å.

6.3 Results

Thaumatin crystals survive slow-cooling to T=100 K, with or without a soak in 40% glycerol, and exhibit low temperature diffraction properties that are comparable to or better than flash cooled crystals. Figure 6.3a shows diffraction patterns acquired from a single thaumatin crystal at four different temperatures as it was cooled. The crystal contained no cryoprotectants, and the only solutes present in the mother liquor were the buffer and 1.5 M sodium-potassium tartrate. Figure 6.3b shows diffraction patterns from a second slow-cooled thaumatin crystal differing only in that it was first soaked in mother liquor + 40 % (w/v) glycerol.

Neither set of diffraction patterns shows any qualitative change on cooling, except that two sharp rings suddenly appear at T~255 K. These rings indicate that a crystalline phase has formed, but their positions do not correspond to those for ice. Their sudden appearance is not reflected in any change in the properties (unit cell, mosaicity, B-factor) of the protein crystal, but coincides with a slight clouding of the oil surrounding the sample, visible at T=100 K in Figure 6.2b. When a drop containing only Paratone-n oil is slow cooled, identical diffraction rings form at the same temperature, but no rings are observed when the drop is flash cooled. These results suggest that the rings are an artefact of slowly cooling the oil, and that the crystalline phase responsible does not interact with the protein crystal in any way.

Figure 6.4 shows the unit cell volume, mosaicity, and Wilson B-factor for two slow-cooled thaumatin crystals, one taken directly from the mother liquor and one soaked in a cryoprotectant solution. These quantities change most rapidly above T~200 K, and are more weakly temperature dependent below that temperature. At T=100 K, the

mosaicities are 0.15° and 0.20° for the as-grown and 40 % glycerol samples, respectively. All of the mosaicity increase on cooling to T=100 K occurs between T=300 K and T~200 K; the mosaicity is constant below 200 K.

The B-factor in Figure 6.4c decreases on cooling, indicating a reduction in thermal motions. For the glycerol-free sample, there is an abrupt change in slope dB/dT at T~210 K. Below T~180 K in both glycerol-free and glycerol-containing samples, the B-factor varies linearly with temperature with a slope of $3 \cdot 10^{-5}$ Å^2/K. As discussed below, the slope change is a signature of the protein dynamical transition (glass transition) and the value of the slope below T=180 K in principle provides information about the protein's potential energy landscape.

Figure 6.5 shows how the diffuse X-ray background varies with temperature. The low-resolution diffuse intensity is clearly reduced at low temperatures. When this intensity is plotted versus temperature (data not shown), it also changes most rapidly above T~200 K, is relatively constant below that temperature, and shows an abrupt change in slope near T~210 K. Arrows in Figure 6.5 indicate the expected positions of Ih (hexagonal) and Ic (cubic) ice diffraction, but there is no evidence of either phase.

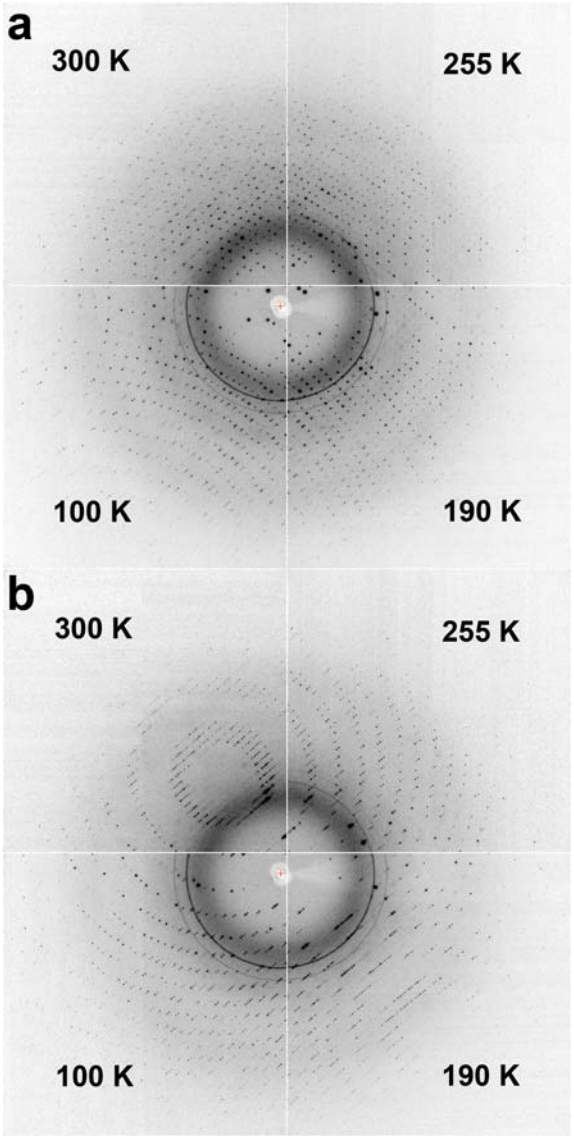

Figure 6.3

Diffraction images acquired at T=300 K, 255 K, 190 K and 100 K during slow cooling of (a) a thaumatin crystal prepared from its mother liquor; and (b) a thaumatin crystal first soaked in 40 % (w/v) glycerol/mother liquor solution. Although diffraction rings from the Paratone oil appear at 255 K, the crystal's diffraction quality does not visibly degrade and no evidence for ice appears during slow cooling.

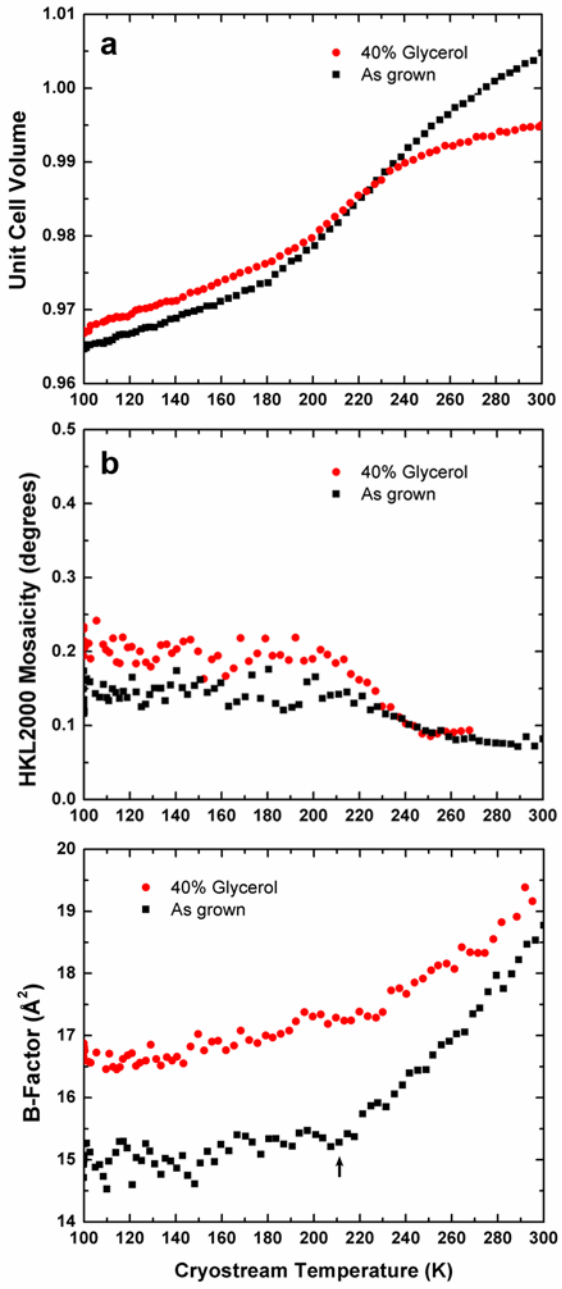

Figure 6.4

Relative cell volume, mosaicity and Wilson B-factor of native and 40% w/v glycerol-soaked thaumatin crystals versus temperature during slow cooling. **(a)** The unit cell volume for both samples rapidly contracts above ~200 K, and contracts more modestly below 180 K. The contraction is anisotropic above 200 K but becomes isotropic below

180 K (see Figure 6.6.) The cell volume for both samples is referenced to an arbitrary value midway between their respective initial cell volumes. **(b)** The mosaicity increases most rapidly in the temperature range where the lattice contraction is both rapid and anisotropic. **(c)** The B-factor decreases with decreasing temperature. The abrupt change in slope at ~210 K (marked by an arrow) for the as-grown sample is evidence of a dynamical transition in the protein.

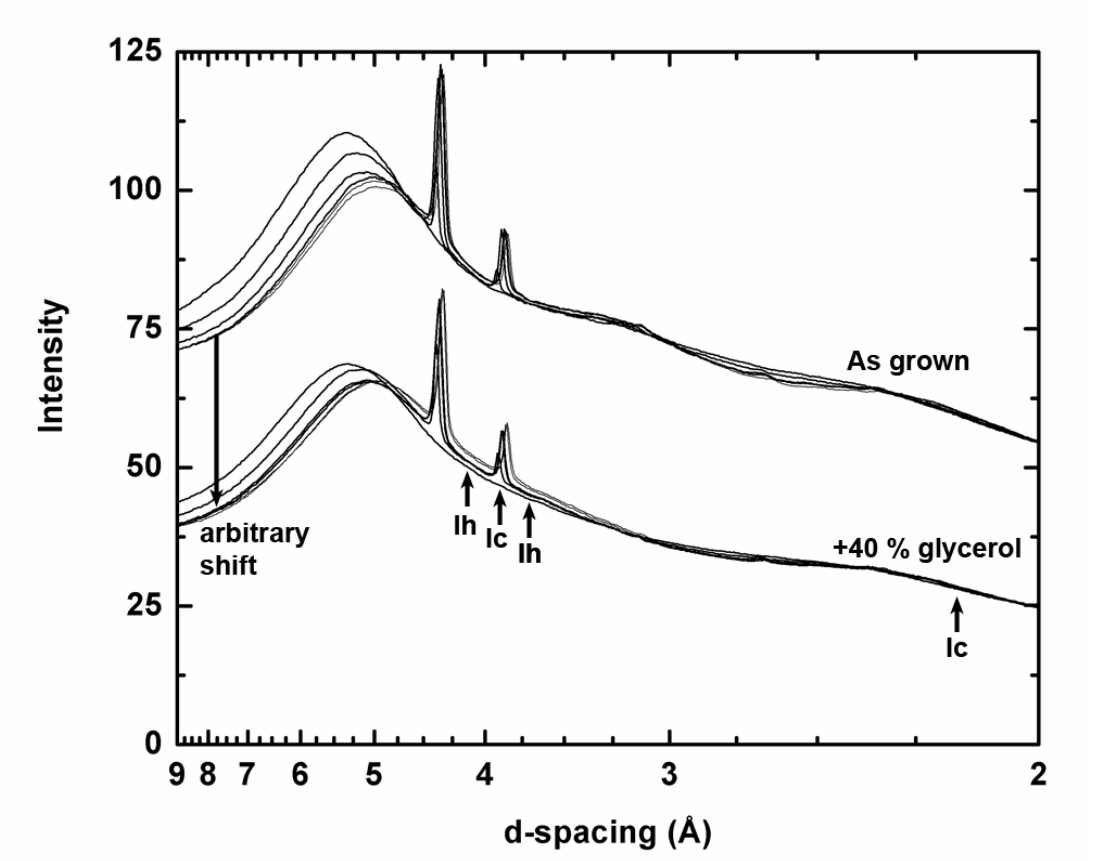

Figure 6.5

The azimuthally-integrated X-ray background intensity versus resolution for the as-grown and 40 % (w/v) glycerol thaumatin crystals, at temperatures (from top to bottom) of 300, 250, 210, 170, 140 and 100 K. The data for the glycerol-soaked

crystal is shifted down by 25 for clarity. The large peak at 5.2 Å is diffuse scatter from the Paratone-n oil, and the sharp rings are due to a crystalline phase that forms within the oil during slow cooling. Arrows indicate the expected d values for Bragg scattering from ice Ih or Ic would be expected. Most of the decrease in the diffuse scatter at low resolution on slow cooling occurs above T=200 K, roughly tracking the behavior of the B factor in Figure 6.4c.

6.4 Discussion

6.4.1 Slow cooling gives high diffraction quality without penetrating cryoprotectants or high pressures

Slow cooling with no cryoprotectants — at rates 10^3 to 10^4 times smaller than are achieved in flash cooling — yields thaumatin crystal mosaicities at T=100 K that are as good as or better than have been obtained using any other method. The mosaicity of the as-grown (cryoprotectant-free) crystal in Figure 6.3a increased from 0.08° to 0.15° on cooling to 100 K. Of the four slow-cooled thaumatin crystals examined (two at 0% glycerol, one at 30% glycerol and one at 40% glycerol), the average T=100 K mosaicity is 0.2°. This can be compared with a typical mosaicity of 0.4 to 0.5° for thaumatin crystals that have been flash cooled in our lab using conventional methods.

These results can also be compared with those of Kim *et al.* (2005), who examined penetrating cryoprotectant-free thaumatin crystals that were cooled under high pressures (up to 200 MPa) to prevent hexagonal ice formation. The average mosaicity for the four thaumatin crystals studied was 0.3°, and the smallest mosaicity obtained was 0.11°, much smaller than was obtained by Kim *et al.* using conventional flash

cooling. The crystals were coated in NVH oil to prevent dehydration during pressurization — which removed external solvent — and the apparatus and cooling protocol gave relatively slow cooling rates — perhaps at 1-10 K/s. Our results show that high pressures were not needed to prevent ice crystallization within the crystals, and that the improved mosaicities may have been primarily due to external solvent removal by the oil, suppression of ice formation by the protein, and slower cooling. High pressures may then only be necessary for crystals with very high solvent contents and large solvent channels (at least larger than the ~35 Å in thaumatin), where the protein alone may provide inadequate cryoprotection.

6.4.2 How much ice is present in slow-cooled crystals?

The diffraction data in Figure 6.5 shows no evidence for the ice rings expected from either Ih (hexagonal) or Ic (cubic) ice, the two phases that can form at ambient pressure. As discussed above, the two observed peaks/rings are not due to ice, and are present when drops containing only Paratone-n oil are cooled. However, the smaller of the two oil-related peaks lies very close to the expected position of the low-resolution peak from ice Ic, and so could obscure the presence of a small amount of that ice phase.

The presence of ice Ic could be revealed in at least two ways. First, Ic has a strong second-order peak at 2.19 Å with an intensity 0.41 times that of the primary peak. No peak is observed at this position (indicated by an arrow) in Figure 6.5. Second, the abrupt formation of cubic ice at some temperature should abruptly change the intensity ratio between the large and small Paratone-n peaks. No such change is observed.

An upper bound on the ice fraction present within our samples can be estimated as follows. The total number of scattered X-rays (into all of k-space) from a given crystalline phase is proportional to the total integrated electron density in that phase that is illuminated (in real space) by the X-ray beam. Provided that a representative region of k-space is examined, the ratio of the diffraction intensity from the two phases is equal to the ratio of the number of electrons in each phase. For our estimate, we include all diffraction collected in a series of five 1° oscillation frames to a resolution of 1.8 Å, which includes the positions of all integrable reflections from the protein and the first three rings from cubic ice. The total number of detected X-ray photons contained in the protein peaks is computed for each frame (as the sum of integrated peak intensities from Denzo), and varies by roughly 10% between frames. This total, averaged over five frames, is $\sim 2 \times 10^6$ "intensity units" (as reported in the dark-corrected image file produced by the ADSC Q-210 detector software). This total is then used as an estimate of the total number of the illuminated electrons that are associated with the protein (in arbitrary units). Any disorder in the protein or its lattice shifts intensity from the peaks to the diffuse background, and so this is an underestimate.

Figure 6.5 shows the X-ray intensity measured in a given resolution shell (one pixel wide), averaged over 5 frames / 5° in ϕ (sample rotation), versus resolution. Pixels within a 10 × 10-pixel square centered on the position of each reflection (obtained from Denzo's .x output files) were omitted from the average A smooth fit to the background gives an estimate of the fluctuations (from all sources) in this averaged value of 0.1 “intensity units” per pixel. The ice Ic detection limit is proportional to this fluctuation level. It is inversely proportional to the grain size of the cubic ice, which

determines the number of pixels over which ice diffraction is spread and thus the ice intensity in each pixel.

Consider the as-grown thaumatin sample. Using the Scherrer equation, the width of the powder ring (on the detector, in pixels) expected from microcrystallites of a given size can be calculated. If cubic ice with a grain size of 15 nm is present, then its first and second order reflections will illuminate approximately 10^5 pixels on the detector, including those pixels within each powder ring's FWHM. If detecting the ice requires an extra 0.1 "intensity units" in each of these pixels, then ~10^4 intensity units must be scattered from cubic ice to be detectable. The total integrated intensity per frame from protein for this sample was ~10^6, giving an order-of-magnitude upper bound for the ice fraction of less than 1 %. If the ice instead has a grain size of 150 nm, then the detection limit according to this crude estimate would be 0.1 %.

6.4.3 Why can crystals be slow cooled without cryoprotectants?

Key to the successful slow cooling of thaumatin crystals is the surprising fact that no ice forms within them, even when no penetrating cryoprotectants are used. Previous measurements on aqueous glycerol solutions (Sutton, 1991; Berejnov *et al*., 2006; Warkentin *et al*., 2008) have shown that glycerol concentrations of at least 50 – 60 % (w/v) are required to prevent ice formation at cooling rates of 1 K/s. Extrapolating to the present cooling rate of 0.1 K/s implies that the protein and salt (derived from the 1.5 M sodium-potassium tartrate of the mother liquor within thaumatin crystals) is as effective in inhibiting ice formation as 70% w/v glycerol. Sartor *et al.* (1995) have determined the minimum cooling rates needed to prevent ice formation in hydrated protein powders. For hydration levels of 0.56 to 0.73 (mass water/mass protein), the

required cooling rates were 25 K/s to 4 K/s. The hydration level in thaumatin (1.22) is much larger, and the required cooling rate is much smaller. This suggests that regular crystalline packing of the protein increases its ability to inhibit ice nucleation.

Experiments on pure water in porous glass found that crystalline ice only forms in pores larger than ~25 Å. (Rault *et al.*, 2003). In experiments on protein crystals, crystalline ice formed from vitrified solvent on warming from 150 K to 200 K in crystals with solvent channels 65 Å or larger, but no internal ice formed in crystals with solvent channels smaller than 20 Å (Weik *et al*., 2001; Weik *et al.,* 2005). Because the first hydration layer behaves very differently from bulk water, a protein crystal's effective pore/channel size for nucleation is reduced from its geometric value. Thus, the channel diameter of thaumatin crystals (25 – 35 Å) may be smaller than is required for nucleation of cubic ice on our experimental timescales.

6.4.4 Origins of disorder on cooling

The mechanisms that create disorder on cooling should be affected by cooling rate. Slower cooling allows more time for ice crystal nucleation and growth (and perhaps other processes) that degrade protein crystal diffraction properties, and this has been the most important obstacle in previous diffraction studies of slow-cooled crystals. On the other hand, slower cooling reduces thermal gradients within the crystal and associated crystal strains that can drive cracking and broaden mosaicity (Kriminski *et al.,* 2003).

Slower cooling may also reduce strains and disorder associated with the inherent thermal expansivity mismatch between the protein lattice and the solvent that fills its

voids (Juers and Matthews 2001; Kriminski *et al.*, 2002; Juers & Matthews, 2004b; Lovelace *et al*., 2006). This mismatch requires that the solvent either flow (to the crystal surface or to grain boundaries and other defective regions where the lattice is weak) or compress. We estimate that pressures of 10 – 100 MPa could be generated within the crystal if negligible flow occurs, based upon the observed expansivity of the thaumatin lattice and the measured expansivity of water confined to 2 nm pores (Mallamace *et al*., 2007). Slower cooling allows more time before vitrification for solvent to flow and to accommodate the contracting protein lattice, and so may reduce stresses and solvent pooling in defective regions and thereby help maintain crystal order.

In the present experiments, essentially all of the mosaicity increase occurs above 200 K, where the mismatch between solvent expansion and lattice contraction is large (Mallamace *et al*., 2007). The largest rate of mosaicity increase occurs at temperatures (200 – 220 K) where the unit cell volume is rapidly decreasing and the solvent viscosity is rapidly increasing. If expansion mismatch in fact accounts for some of the increased crystal disorder, one might expect that adding glycerol, which unlike water only contracts on cooling, would reduce the mismatch and the amount of disorder. However, glycerol also strongly increases solvent viscosity and reduces solvent diffusion, and so the flow required to relieve the stresses caused by any remaining mismatch is inhibited.

We also note that above 200 K, thaumatin's lattice contraction on cooling is strongly anisotropic. Below 180 K it is very nearly isotropic (Figure 6.6), and occurs at a rate ($\sim 10^{-4}$ K^{-1}) very close to the thermal contraction of amorphous water (also $\sim 10^{-4}$ K^{-1}) at that temperature (Mallamace *et al*., 2007). Anisotropic contraction requires transport

of solvent within the unit cell, i.e., solvent molecules must flow past or around protein molecules. Below 200 K, solvent flow and translational diffusion are negligible (Weik *et al*., 2004; Wood *et al*., 2007; Wood *et al*., 2008) and so contraction should become nearly isotropic.

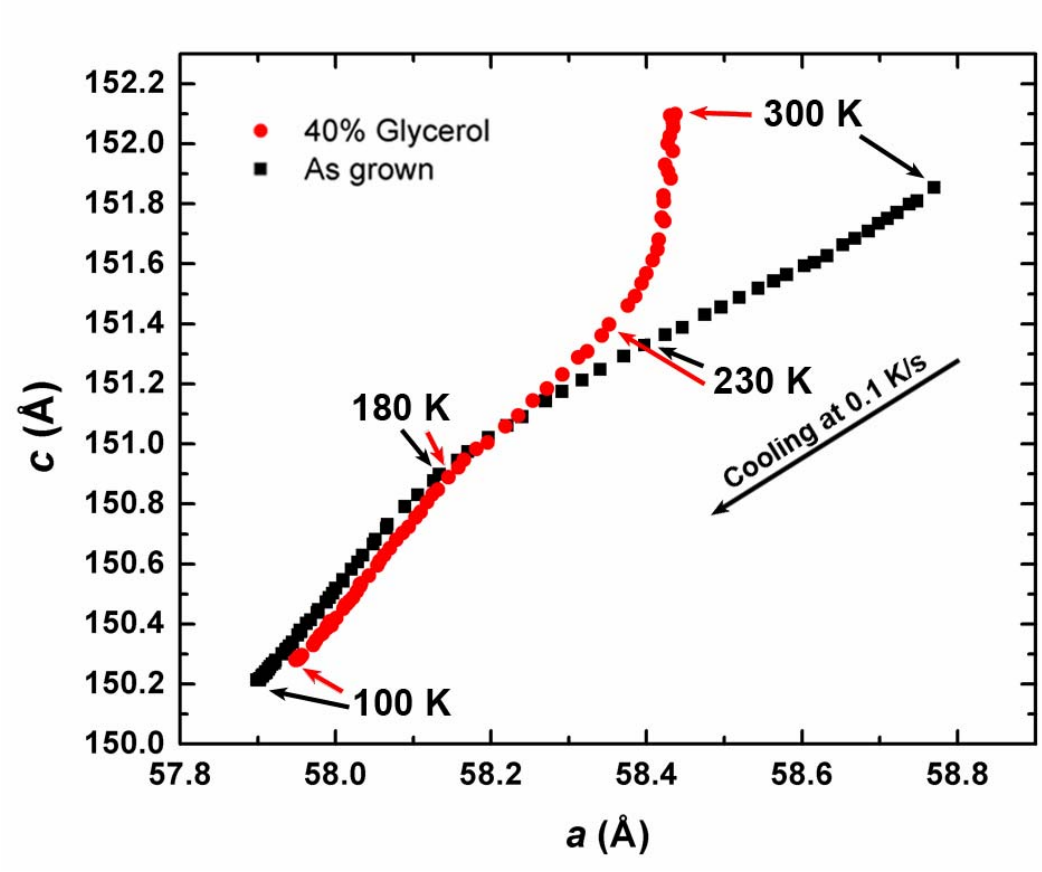

Figure 6.6

Lattice parameters *a* vs *c* during cooling for the as-grown and 40 % glycerol crystals. Both crystals show very nearly isotropic contraction below ~180 K (indicated by an arrow).

6.4.5 Comparison to previous work

Petsko and co-workers demonstrated that ribonuclease A goes through a "dynamical transition" at ~220 K (Tilton *et al*., 1992; Rasmussen *et al*., 1992). This transition was characterized by a kink in the crystallographic Debye-Waller factor (B-factor), indicating the onset of long-range, anharmonic motions (e.g. translational diffusion in the solvent, motion of surface side-chains, or larger conformational changes) on warming above the transition temperature. This kink was also observed in mean-square displacements measured in earlier Mössbauer spectroscopy studies of ^{57}Fe in myoglobin (Parak *et al*., 1982), as well as with inelastic neutron scattering (Doster *et al*., 1989), but the transition does not appear in myoglobin's crystallographic B-factors (Chong *et al*., 2001).

Figure 6.4c shows the Wilson B-factors of two slow-cooled thaumatin crystals. The crystal without glycerol shows a well-defined kink (change in slope) in B(T) signalling a transition at 210 K, whereas the crystal soaked in 40 % glycerol shows what could be interpreted as a broadened transition. The integrated diffuse background intensity in the resolution range 15 – 5 Å, shown in Figure 6.5, also shows a kink. This is not surprising, as both the B factor and diffuse scatter are related to thermal motions (and/or static disorder) of the protein. However, for both crystals the transition as seen through diffuse scatter occurs at a lower temperature than as seen through the B-factor (associated with Bragg reflections). We note that this loss of diffuse intensity at low resolution cannot be accounted for by the appearance of oil rings at T=255 K: the diffuse intensity shows most of its decrease above 255 K, and it varies smoothly near 255 K despite the abrupt appearance of the oil rings.

Previous studies on flash-cooled protein crystals have shown that the solvent undergoes an amorphous solid to liquid transition as the temperature is increased through the range 180 K to 220 K, driving a solid-like to liquid-like transition in the protein molecule itself. (Vitkup *et al*., 2000; Weik *et al*., 2001a; Weik *et al*., 2001b; Weik *et al*., 2005; Wood *et al*., 2007; Wood *et al*., 2008). Below this transition, the B-factor decreases linearly with decreasing temperature. This decrease is usually attributed to a reduction in the amplitudes of harmonic thermal motions, consistent with the notion that the system is solid-like below 180 K.

For slow-cooled thaumatin crystals (Figure 6.4c), the average mean-squared-displacement's (MSD = $B/8\pi^2$) variation with temperature below T=180 K is dMSD/dT ~$5 \cdot 10^{-5}$ Å^2/K. The dMSD/dT values obtained from crystals of myoglobin (Parak *et al*., 1982; Chong *et al*., 2001), ribonuclease A (Tilton *et al.,* 1992; Rasmussen *et al*., 1992), lysozyme (Joti *et al*., 2002), maltose binding protein (Wood *et al*., 2008) and purple membrane (Wood *et al*., 2007) are in the range 10^{-4} to 10^{-3} Å^2/K; the rate for hexagonal ice is ~ $2 \cdot 10^{-4}$ Å^2/K (Teeter *et al*., 2001). These studies followed a variety of thermal trajectories from room temperature to the measurement temperature, including slow cooling and warming to each temperature (Parak *et al.,* 1982; Wood *et al.,* 2007; Wood *et al*., 2008)), quenching from room temperature to each measurement temperature (Tilton *et al.,* 1992; Rasmussen *et al.,*1992; Chong *et al.,* 2001; Teeter *et al.,* 2001), and quenching to low temperature and then slowly warming to each measurement temperature (Joti *et al*., 2002). If the entire change in B is due to changes in harmonic motions, then thaumatin must be an unusually "stiff" protein in this temperature range. B(T) can also be affected by changes in static disorder. A reduced magnitude of dB/dT could result if there is a gradual increase in

static disorder — either due to a gradual trapping of metastable microstates, or due to an increase in lattice-level disorder — during slow cooling.

Previous temperature-dependent studies of protein crystals required the use of large cryoprotectant concentrations. To prevent ice formation and loss of diffraction at temperatures approaching 200 K, Singh *et al.* (1980) used 45% - 75% methanol in their bovine trypsinogen crystals (47 % w/v solvent.) Tilton *et al*. (1992) used 50 % methanol or 50 % MPD in their ribonuclease A crystals, but were still unable to obtain data at 200 K because the crystals "rapidly became opaque and ceased to diffract". These results highlight how remarkable it is that thaumatin can be successfully cooled to any temperature without cryoprotectants.

6.4.6 A generally applicable method?

The method described here has been applied to ribonuclease A (cell volume 225,000 $Å^3$, solvent content 45 %), lysozyme (cell volume 220,000 $Å^3$, solvent content 36 %), trypsin (200,000 $Å^3$, solvent content 42 %), insulin (cell volume 456,000 $Å^3$, solvent content 63 %), and urease (cell volume 4,900,000 $Å^3$, solvent content 48 %) crystals (Jabri *et al.,* 1992; Jabri *et al*., 1995; Jabri & Karplus, 1996), in addition to the thaumatin samples described above. As-grown (cryoprotectant-free) urease and insulin crystals can be slow-cooled to T=100 K without ice formation or significant degradation of diffraction quality, with a success rate of ~75 %, based upon approximately 15 trials. Lysozyme and trypsin crystals can be successfully slow-cooled in 40 % glycerol. But when as-grown (cryoprotectant-free) crystals are cooled, diffraction quality abruptly degrades and cubic ice forms near T=210 K, and in almost every case the diffraction is too poor to continue the experiment. Ribonuclease A

crystals were grown in high salt (4 M sodium chloride), and this salt precipitated out as the temperature was lowered, destroying the crystalline order. These results suggest that, with continued methodological refinement, it may be possible to slow cool a substantial fraction of protein and virus crystals without the use of penetrating cryoprotectants. Slow cooling may thus provide an alternative as well as a complement to flash cooling in cryocrystallographic studies.

We have also successfully flash cooled thaumatin, lysozyme, trypsin, insulin and urease crystals to specific temperatures between 300 K and 100 K using the same solvent removal and mounting protocol as for slow cooling and then simply placing them in a gas stream at the desired temperature. Although glycerol improves the success rate significantly, high quality diffraction data has been obtained without use of penetrating cryoprotectants from all five proteins.

6.5 Conclusion

The present results demonstrate that high-quality diffraction data can be continuously collected from an individual crystal, over the entire temperature range between 300 K and 100 K, by cooling at 0.1 K/s. Successful slow cooling does not require large cryoprotectant concentrations or special apparatus (e.g., for generating high pressures), but only that all external solvent be removed from the crystal. Thaumatin crystals cooled in this way show exceptionally low mosaicity and no evidence of crystalline ice at T=100 K. The small observed mosaicity increase occurs above 200 K, where the mismatch between protein lattice contraction and solvent expansion is largest and where the unit cell contraction is anisotropic. This suggests that the mismatch is an important source of crystal disorder, as has been observed in previous studies.

Cooling rates 10^3-10^4 times slower than in conventional flash cooling (and 10^5-10^6 times slower than in hyperquenching (Warkentin *et al.*, 2007)) will affect how a protein explores its energy landscape and the conformational states observed during and after cooling to low or intermediate temperatures. Slow cooling may thus provide a new window into protein structure and function.

REFERENCES

Berejnov, V., Husseini, N. S., Alsaied, O. A., & Thorne, R. E. (2006). *Journal of Applied Crystallography* **39**, 244-251.

Bourgeois, D. & Royant, A. (2005). *Current Opinion in Structural Biology* **15**, 538-547.

Bourgeois, D. & Weik M. (2009). *Reviews of Crystallography* **15**, 87-118.

Cervelle, B., Cesbron, F., Berthou, J., and Jolles, P. (1974). *Acta Crystallogr. A* **30** 645-648.

Chong, S. H., Joti, Y., Kidera, A., Go, N., Ostermann, A., Gassmann, A., & Parak, F. (2001). *European Biophysics Journal with Biophysics Letters* **30**, 319-329.

Colletier, J. P., Bourgeois, D., Sanson, B., Fournier, D., Sussman, J. L., Silman, I., & Weik, M. (2008). Proceedings of the National Academy of Sciences of the United States of America **105**, 11742-11747.

Doster, W., Cusack, S., & Petry, W. (1989). Nature **337**, 754-756.

Edayathumangalam, R. S. & Luger, K. (2005). Acta Crystallographica Section D-Biological Crystallography **61**, 891-898.

Frauenfelder, H., Petsko, G. A., & Tsernoglou, D. (1979). *Nature* **280**, 558-563.

Gakhar, L. & Wiencek, J. M. (2005). *Journal of Applied Crystallography* **38**, 945-950.

Garman, E. (1999). *Acta Crystallographica Section D-Biological Crystallography* **55**, 1641-1653.

Garman, E. F. & Schneider, T. R. (1997). *Journal of Applied Crystallography* **30**, 211-237.

Harp, J. M., Timm, D. E., & Bunick, G. J. (1998). *Acta Crystallographica Section D-Biological Crystallography* **54**, 622-628.

Harp, J. M., Hanson, B. L., Timm, D. E., & Bunick, G. J. (1999). *Acta Crystallographica Section D-Biological Crystallography* **55**, 1329-1334.

Hope, H. (1988). *Acta Crystallographica Section B-Structural Science* **44**, 22-26.

Hope, H. (1990). *Annual Review of Biophysics and Biophysical Chemistry* **19**, 107-126.

Jabri, E., Lee, M. H., Hausinger, R. P., & Karplus, P. A. (1992). *Journal of Molecular Biology* **227**, 934-937.

Jabri, E., Carr, M. B., Hausinger, R. P., & Karplus, P. A. (1995). *Science* **268**, 998-1004.

Jabri, E. & Karplus, P. A. (1996). *Biochemistry* **35**, 10616-10626.

Joti, Y., Nakasako, M., Kidera, A., & Go, N. (2002). *Acta Crystallographica Section D-Biological Crystallography* **58**, 1421-1432.

Juers, D. H. & Matthews, B. W. (2001). *Journal of Molecular Biology* **311**, 851-862.

Juers, D. H. & Matthews, B. W. (2004). *Quarterly Reviews of Biophysics* **37**, 105-119.

Juers, D. H. & Matthews, B. W. (2004). *Acta Crystallographica Section D-Biological Crystallography* **60**, 412-421.

Kim, C. U., Kapfer, R., & Gruner, S. M. (2005). *Acta Crystallographica Section D-Biological Crystallography* **61**, 881-890.

Kmetko, J., Husseini, N. S., Naides, M., Kalinin, Y., & Thorne, R. E. (2006). *Acta Crystallographica Section D-Biological Crystallography* **62**, 1030-1038.

Kriminski, S., Caylor, C. L., Nonato, M. C., Finkelstein, K. D., & Thorne, R. E. (2002). *Acta Crystallogr. D. Biol. Crystallogr.* **58**, 459-471.

Kriminski, S., Kazmierczak, M., & Thorne, R. E. (2003). *Acta Crystallographica Section D-Biological Crystallography* **59**, 697-708.

Kurinov, I. V. & Harrison, R. W. (1995). *Acta Crystallographica Section D-Biological Crystallography* **51**, 98-109.

Lovelace, J. J., Murphy, C. R., Pahl, R., Keith, B., & Borgstahl, G. E. O. (2006). *Journal of Applied Crystallography* **39**, 425-432.

Low, B. W., Chen, C. C. H., Berger, J. E., Singman, L., & Pletcher, J. F. (1966). *Proceedings of the National Academy of Sciences of the United States of America* **56**, 1746-&.

Mallamace, F., Branca, C., Broccio, M., Corsaro, C., Mou, C. Y., & Chen, S. H. (2007). *Proceedings of the National Academy of Sciences of the United States of America* **104**, 18387-18391.

McFerrin, M. B. & Snell, E. H. (2002). *Journal of Applied Crystallography* **35**, 538-545.

McPherson, A. (1999). *Crystallization of Biological Macromolecules.* New York: Cold Spring Harbor Laboratory Press.

Mitchell, E. P. & Garman, E. F. (1994). *Journal of Applied Crystallography* **27**, 1070-1074.

Otwinowski, Z. & Minor, W. (1997). *Macromolecular Crystallography, Pt A* **276**, 307-326.

Parak, F., Knapp, E. W., & Kucheida, D. (1982). *Journal of Molecular Biology* **161**, 177-194.

Pflugrath, J. W. (2004). *Methods* **34**, 415-423.

Rasmussen, B. F., Stock, A. M., Ringe, D., & Petsko, G. A. (1992). *Nature* **357**, 423-424.

Rault, J., Neffati, R., & Judeinstein, P. (2003). *European Physical Journal B* **36**, 627-637.

Rodgers, D. W. (1994). *Structure* **2**, 1135-1140.

Sartor, G., Hallbrucker, A., & Mayer, E. (1995). *Biophysical Journal* **69**, 2679-2694.

Singh, T. P., Bode, W., & Huber, R. (1980). *Acta Crystallographica Section B-Structural Science* **36** , 621-627.

Snell, E. H., Judge, R. A., Larson, M., & van der Woerd, M. J. (2002). *Journal of Synchrotron Radiation* **9**, 361-367.

Sutton, R. L. (1991). *Journal of the Chemical Society-Faraday Transactions* **87**, 101-105.

Teeter, M. M., Yamano, A., Stec, B., & Mohanty, U. (2001). *Proceedings of the National Academy of Sciences of the United States of America* **98**, 11242-11247.

Teng, T. Y. & Moffat, K. (1998). *Journal of Applied Crystallography* **31**, 252-257.

Thorne, R., Kriminski, S., Caylor, C., & Kisselev, A. (2001). *Biophysical Journal* **80**, 58A.

Tilton, R. F., Dewan, J. C., & Petsko, G. A. (1992). *Biochemistry* **31**, 2469-2481.

Vitkup, D., Ringe, D., Petsko, G. A., & Karplus, M. (2000). *Nature Structural Biology* **7**, 34-38.

Walker, L. J., Moreno, P. O., & Hope, H. (1998). *Journal of Applied Crystallography* **31**, 954-956.

Warkentin, M., Berejnov, V., Husseini, N. S., & Thorne, R. E. (2006). *Journal of Applied Crystallography* **39**, 805-811.

Warkentin, M., Stanislavskaia, V., Hammes, K., & Thorne, R. E. (2008). *Journal of Applied Crystallography* **41**, 791-797.

Weik, M., Kryger, G., Schreurs, A. M. M., Bouma, B., Silman, I., Sussman, J. L., Gros, P., & Kroon, J. (2001). *Acta Crystallographica Section D-Biological Crystallography* **57**, 566-573.

Weik, M., Vernede, X., Royant, A., & Bourgeois, D. (2004). *Biophysical Journal* **86**, 3176-3185.

Weik, M., Schreurs, A. M. M., Leiros, H. K. S., Zaccai, G., Ravelli, R. B. G., & Gros, P. (2005). *Journal of Synchrotron Radiation* **12**, 310-317.

Wood, K., Plazanet, M., Gabel, F., Kessler, B., Oesterhel, D., Tobias, D. J., Zaccai, G., & Weik, M. (2007). *Proceedings of the National Academy of Sciences of the United States of America* **104**, 18049-18054.

Wood, K., Frolich, A., Paciaroni, A., Moulin, M., Hartlein, M., Zaccai, G., Tobias, D. J., & Weik, M. (2008). *Journal of the American Chemical Society* **130**, 4586-4587.

CHAPTER 7

TEMPERATURE DEPENDENCE OF X-RAY RADIATION DAMAGE TO PROTEIN CRYSTALS: ACTIVATION ENERGY OF SECONDARY DAMAGE

7.1 Introduction

Any study of biological matter that utilizes ionizing radiation must contend with the problem of radiation damage. Even under ideal experimental conditions, radiation damage places a fundamental limit on the amount of information that can be obtained from a sample before it stops yielding useful information. It is important to remember that this limit is naturally arbitrary, as it depends on the experimenter's definition of "useful information"—indeed, the sample could be said to be "damaged" as soon as the first inelastic scattering event takes place. An operational rule of thumb, with origins in the cryo-electron microscopy community has been adopted and is appropriate in most circumstances. (Henderson, 1990)

In X-ray protein crystallography, radiation damage is an important consideration when planning and experiment. Originally, it was overcome by using large crystals, and scaling together data from many crystals. Once reliable cryocrystallography protocols were established, it became common practice to collect data at 100 K, where protein crystals are approximately 50 – 100 times less sensitive to X-rays. (Nave & Garman, 2005; Southworth-Davies *et al*., 2008) Since that time, X-ray radiation damage to protein crystals has become much better understood, at least at the practical level required for structural biology.

The process of radiation damage proceeds in two phases, which have been called "primary" and "secondary", as follows: First, a ~10 keV photon is absorbed or inelastically scattered, either by a protein or solvent atom, depositing a large amount of energy. This energy is then carried away from the location of the initial event as a shower of ~10-100 eV electrons (Singh & Singh, 1982; Cowan & Nave, 2008). This spur spreads out, resulting in a cascade of radiochemical reactions, and additional photoelectrons, covering a range of ~3 microns (Holton, 2009). The reactions include the production of free-radicals in the solvent, as well as the breaking of bonds in the protein molecule itself. All of this occurs on sub-picosecond timescales, faster than atomic motions (Henderson, 1995). As a result, these processes are expected to be relatively temperature independent, and are called *primary radiation damage.*

Once primary damage has occurred, the free radicals and (now destabilized) protein molecules can begin to move. These motions involve the diffusion of free radicals through the solvent channels in the crystal to the protein molecules, where they may react and cause further damage. They also involve the disordering of damaged protein molecules, and the eventual amorphization of entire unit cells (Blake & Phillips, 1962). All of these processes require diffusive motions of large numbers of atoms, which must move a distance that is many times larger than their vibrational extent. These processes occur on the micro- to millisecond timescale, and are thus many orders of magnitude slower than primary damage. In addition, they require long-range diffusive motion of many atoms, and so they are expected to be strongly temperature-dependent. Because there is such a clear separation of the two processes in timescale, this second set of events is called *secondary radiation damage*.

The primary aim of this study is to shed light on the mechanism of radiation damage by measuring its temperature dependence over the range 300 K to 100 K. It is known that the sensitivity of typical protein crystals is reduced by a factor of 50 to 100 on cooling from 300 K to 100 K (Nave & Garman, 2005). This effect is believed to be due to the glass transition in the solvent + protein system, which limits the mobility of both radical species and the protein molecules themselves. Our results confirm this view. Between 300 and 170 K, the reduction in sensitivity is driven by the decreasing rates of diffusion of protein hydration water, reaction of radical species, and conformational motions of protein molecules. We measure an activation energy for radiation damage of 2.7 kcal/mol, consistent with hydration water diffusion. This "diffusion limited" view is further supported by the fact that the addition of 40 % glycerol to the crystals causes the activation energy to increase by 50%. Below 170 K, the sensitivity is relatively temperature independent, and in agreement with previous studies.

We also discuss the nature of radiation damage in terms of how it is commonly measured. Our understanding of radiation damage comes from two types of effects, called "specific" and "global". Studies of specific damage examine *systematic* changes in the molecular structure after irradiation.

These changes happen comparatively rapidly (Holton, 2009), vary greatly from protein to protein and from site to site within a given protein (Burmeister, 2000), can complicate phasing (Ravelli & McSweeney, 2000), and can affect the biological relevance of the data (Weik *et al.,* 2000). Specific damage can also be useful for solving structures, because the anomalous differences introduced by the damage can be used for phasing (Ravelli *et al*., 2003; 2005). It has also recently been introduced

as a tool in kinetic crystallography, where X-rays were used to drive a reaction in the active site of an enzyme (Bourgeois & Royant, 2005; Colletier *et al*., 2008).

Studies of global damage measure the *random* disordering of the crystalline lattice (at both the intra- and inter-molecular levels). In practice, a global measure of damage includes any systematic changes as well as random ones. While global damage reduces the overall quality of the data obtained, it is less likely to affect the biological relevance of the data: Insofar as it only introduces random motions in each unit cell, the effects will be averaged out in the final structure and just contribute to a loss of resolution, not to errors at specific sites. What is more, all but the smallest crystals yield a complete dataset long before appreciable global damage has occurred at 100 K. For this reason, specific damage is of the most immediate practical concern to a structural biologist using X-ray crystallography.

On the other hand, global damage lends itself more readily to systematic study. At 100 K, it has been shown to be relatively constant (within a factor of 2) for a variety of different protein crystals (Kmetko *et al*., 2006; Owen *et al.*, 2006; Holton, 2009), not to depend on the dose rate (Leiros *et al*., 2001; 2006; Ravelli *et al*., 2002; Sliz *et al*., 2003; Shimizu *et al*., 2007) and to depend linearly on the total absorbed dose. While the mechanisms are still not completely understood, these facts suggest that there *is* a general set of mechanisms, common to all protein crystals.

Finally, we show that the "character" of global damage is strikingly independent of temperature. This was not expected, because many molecular motions are available at 300 K that are frozen out at 100 K. Specifically, one might expect that at high temperature, large regions of the crystal would become totally amorphous, leading to a

complete loss of diffraction intensity. At low temperature, the solid solvent matrix would confine motions to nearer to their ideal lattice positions, leading to an increased Debeye-Waller factor (B-factor). If this were the case, then the ratio of the change in total intensity to the change in B-factor would depend on the temperature. We find instead that the ratio is constant (i.e. a fixed loss of total intensity corresponds to a fixed increase in B-factor at all temperatures.) This finding also informs the discussion of global metrics of radiation damage and facilitates comparisons between studies carried out under different experimental conditions.

7.2 Methods

7.2.1 Crystallization

Tetragonal lysozyme crystals were grown in 24-well trays using the hanging drop method. The well solution was comprised of 7 % (w/v) sodium chloride in 100 mM sodium acetate buffer at pH 4.25. Protein from Sigma-Aldrich was obtained as a purified powder, and dissolved to a concentration of 50 mg/mL in the same buffer. 10 μL hanging drops were prepared by mixing 5 μL each of the protein solution and well solution. 500 μL of well solution was placed at the bottom of each well, and 22 mm siliconized coverglass (Hampton Research, Aliso Viejo, CA, USA) was sealed over the top of the well with high vacuum grease (Dow-Corning).

Tetragonal thaumatin crystals were grown in 24-well trays using the hanging drop method. The well solution was comprised of 1 M sodium potassium tartrate in 100 mM potassium phosphate buffer at pH 6.8. Protein from Sigma-Aldrich was obtained as a purified powder, and dissolved to a concentration of 25 mg/mL in the same

buffer. 10 μL hanging drops were prepared by mixing 5 μL each of the protein solution and well solution. 500 μL of well solution was placed at the bottom of each well, and 22 mm siliconized coverglass (Hampton Research, Aliso Viejo, CA, USA) was sealed over the top of the well with high vacuum grease (Dow-Corning).

Orthorhombic trypsin crystals were grown in 24-well trays using the hanging drop method. The well solution was comprised of 25 % (w/v) polyethylene glycol (molecular weight 8000) and 0.2 M ammonium sulphate in 100 mM Tris buffer at pH 8. Protein from Sigma-Aldrich was obtained as a purified powder, and dissolved to a concentration of 15 mg/mL in the same buffer. 10 μL hanging drops were prepared by mixing 5 μL each of the protein solution and well solution. 500 μL of well solution was placed at the bottom of each well, and 22 mm siliconized coverglass (Hampton Research, Aliso Viejo, CA, USA) was sealed over the top of the well with high vacuum grease (Dow-Corning).

7.2.2 Glycerol Soaks

To incorporate glycerol into the crystals, solutions of glycerol in the appropriate well solution (see above) were prepared in increments of 10 % (w/v). Half of the concentration of protein used for growth was also added to each soaking solution to prevent the crystals from dissolving. For the larger concentrations of glycerol, very small crystals of protein grew in the soaking solutions. Crystals were transferred from their mother liquor to the 0 % glycerol solution (well solution + half initial protein concentration), and from there to each successive solution up to 40 % (w/v). Times between transfers were not controlled, and were on the order of 30 - 90 seconds. Each

crystal was allowed to sit in the final soaking solution for at least 5 minutes. Transfers between soaking drops were done using MicroMounts (Mitegen, Ithaca, NY, USA).

7.2.3 Crystal mounting

In order to perform experiments at temperatures near 200 K, special techniques had to be applied to prevent the formation of crystalline ice during data collection. These techniques are described in detail in Warkentin & Thorne (2009), which is Chapter 6 of this dissertation. Briefly, the presence of aqueous solvent on the surface of the crystal makes it susceptible to ice formation, which dehydrates the protein lattice, often destroying it. When all of the external solvent is removed under oil, the crystal can be cooled to any temperature without danger of ice formation. This is because ice formation within the protein crystal is suppressed due to being confined in nanometer-scale pores (Neffati *et al*., 2003).

At temperatures below 270 K, crystals were first transfered from their growth droplet or cryoprotectant soak into thick immersion oil (Hampton Research, Aliso Viejo, CA, USA). They were then manipulated under the oil with μTools, Micromounts (Mitegen, Ithaca, NY, USA), and nylon loops (Hampton Research, Aliso Viejo, CA, USA) until all of the solvent clinging to the surface had been removed. Finally, they were mounted on a Micromount with as little surrounding oil as possible. They were then simply placed on the goniometer and into the Cryostream set to the desired temperature.

At temperatures of 270 K and 300 K, a large drop of oil was mounted surrounding the crystal to prevent dehydration during the entire experiment.

7.2.4 X-ray diffraction experiments

Data were collected at MacCHESS at stations A1, F1, and F2 using a 100 μm collimator (150 μm at F2), a Cryostream 700 (Oxford Cryosystems, Devens, MA, USA), a Quantum 210 CCD detector (Quantum 270 at F1) (ADSC, Poway, CA, USA), and an energy of 12.6 keV. The X-ray flux was determined using a 6 cm nitrogen ionization chamber whose calibration was supplied by the CHESS staff.

Consecutive runs of 5 frames of data were collected, with an oscillation width of 1 degree per frame, always over the same 5 degree-wedge. As a result, the dose was delivered to the same volume of crystal. (The spreading of the dose due to rotation of the crystal causes the calculated dose to be overstated by a factor that depends on the crystal's length along the beam. For our geometry, the effect is 4 % for a 200 μm length and 9 % for a 400 μm length. Because it is so small, it is not included in the reported sensitivities. To do so would require careful measurement of the crystal geometry during experiments at the synchrotron.)

7.2.5 Data processing

Each run of 5 frames was indexed and integrated independently from the others, with both MOSFLM (Leslie, 2006) and Denzo (Otwinowski & Minor, 1997). The total intensities were calculated by simple summation of the intensities of each reflection integrated by the respective programs. Virtually no differences were seen between the resulting half-dose values calculated from the total intensity as a function of dose. Relative B-factors between each set and the original set were obtained with SCALEIT

(www.ccp4.ac.uk) and with SCALEPACK (Otwinowski & Minor, 1997) as described in Kmetko *et al*., (2006). Aside from a constant factor of 1.33, the results were again very similar. (The relative B-factor values from SCALEPACK were consistently 1.33 times larger than those from SCALEIT.) SCALEPACK did produce smoother dose curves, so those were used, but the coefficients of sensitivity were scaled down by 1.33 to reflect that would have been obtained from SCALEIT, so as to be in line with Kmetko *et al*., (2006).

7.3 Results

Dose curves were obtained at 10 different temperatures in the range 300 K to 100 K. Relative B-factors were determined by scaling successive 5 degree datasets against the initial set as described in Kmetko *et al*., (2006) (see methods). Crystals of thaumatin, trypsin, and lysozyme were investigated, both as-grown and with the addition of 40 % glycerol (dataset 1). In Figure 7.1, we show the increase in the relative B-factor as a function of dose for crystals of Thaumatin soaked in 40 % glycerol as an example. At all temperatures, the response to the dose is linear, at least initially. It was found that once the relative B-factor exceeded ~ 15 $Å^2$ it would become constant *vs.* dose. (not shown - It is not clear whether or not this effect is real, or an artifact of the scaling procedure: once a sufficiently large number of high-resolution spots have faded to zero intensity, the relative B-factor becomes poorly defined.)

The slope of the B_{rel} versus dose curve is divided by $8\pi^2$ (so that it reflects the actual atomic mean-squared displacement), and called the *coefficient of sensitivity to absorbed dose* (s_{AD}) (Kmetko *et al.,* 2006). We have calculated the coefficient of

sensitivity for each sample at each temperature, from plots analogous to the one shown in Figure 7.1. The results are presented in Figure 7.2.

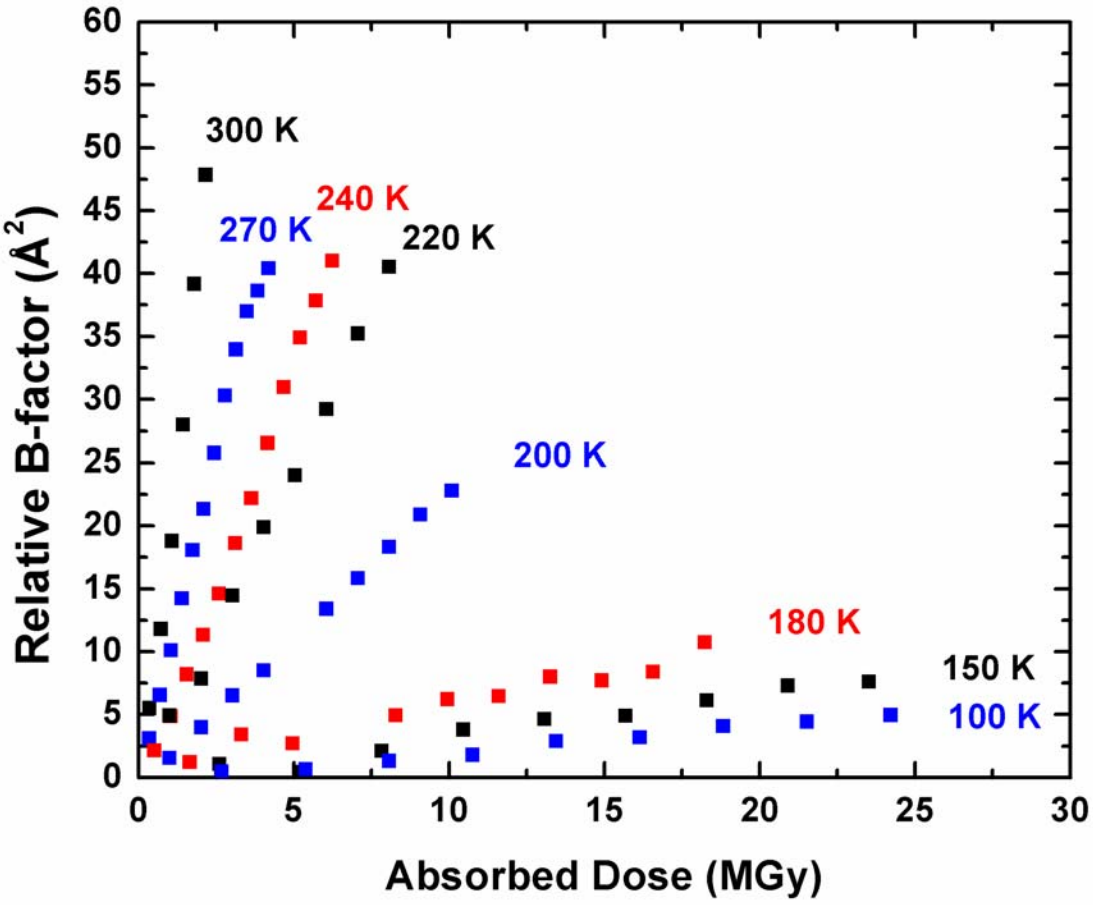

Figure 7.1

Representative dose curves are shown for samples of thaumatin containing 40 % (w/v) glycerol at each of the temperatures investigated. The curves level off for larger doses, so only the initial, linear part of the curve is used in estimating the coefficient of sensitivity.

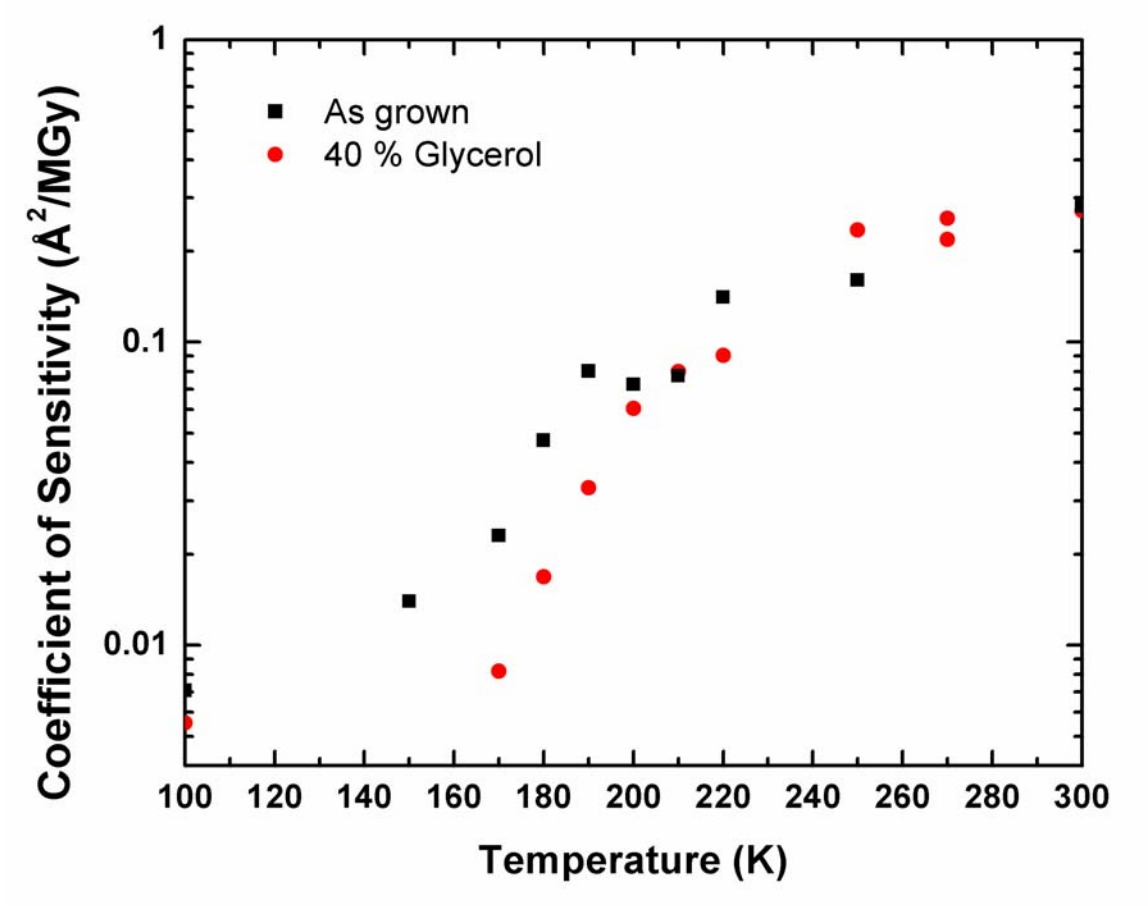

Figure 7.2a

The coefficient of sensitivity of trypsin crystals is plotted as a function of temperature for as-grown crystals and crystals soaked in 40 % (w/v) glycerol.

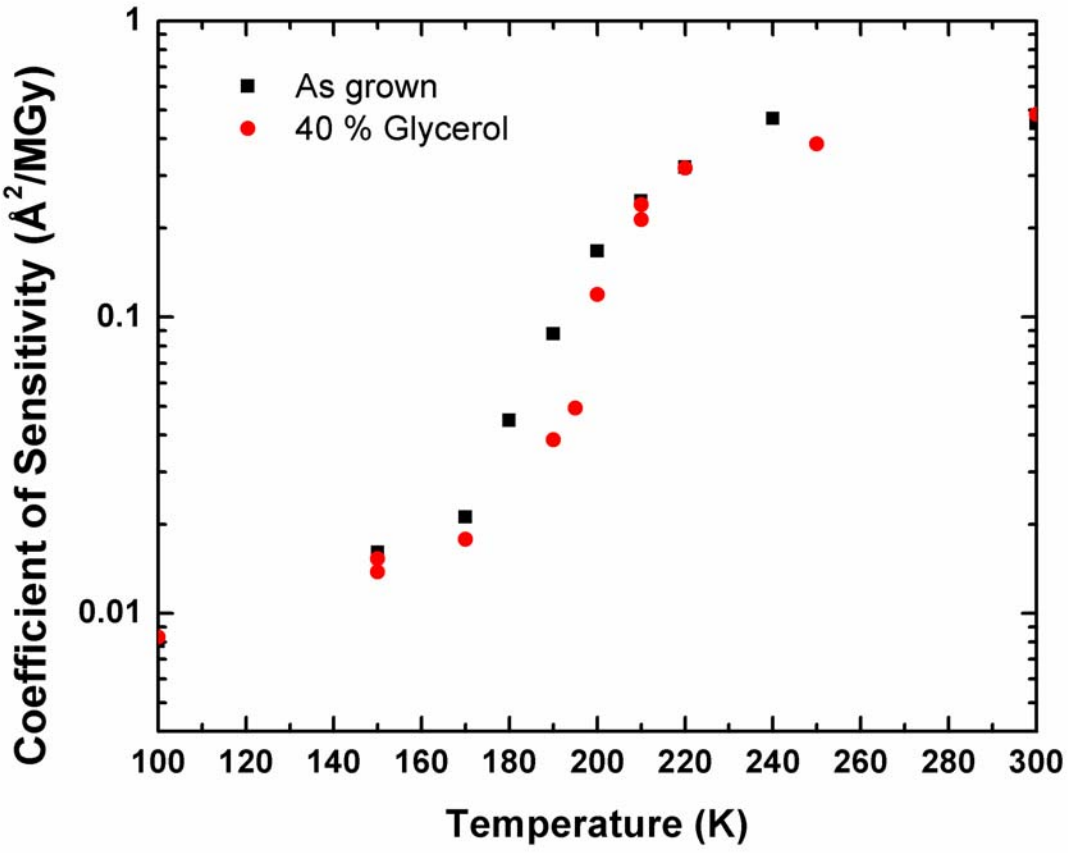

Figure 7.2b

The coefficient of sensitivity of lysozyme crystals is plotted as a function of temperature for as-grown crystals and crystals soaked in 40 % (w/v) glycerol.

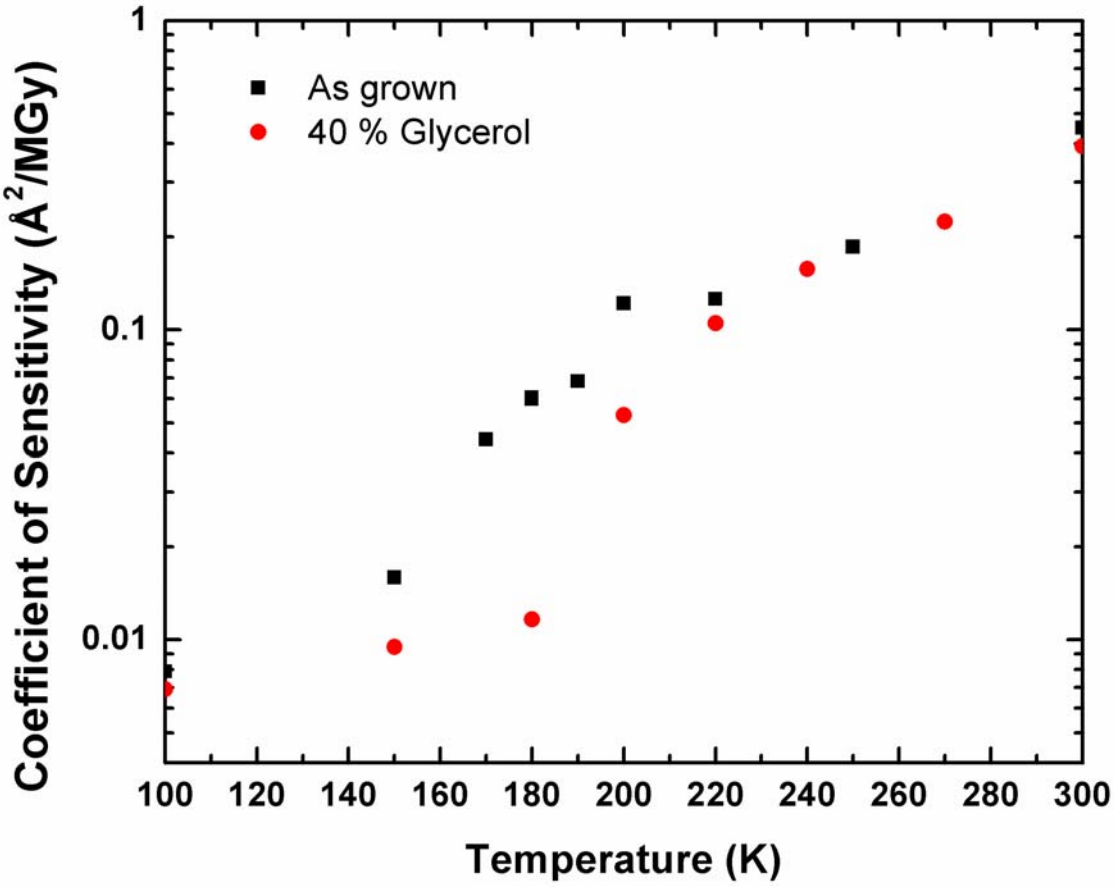

Figure 7.2c

The coefficient of sensitivity of thaumatin crystals is plotted as a function of temperature for as-grown crystals and crystals soaked in 40 % (w/v) glycerol.

In every case, the total reduction in sensitivity is approximately the same (a factor of 50). The results for all three proteins has a similar "S" shape, with relatively small variation at high and low temperatures and a steeper variation at intermediate temperatures. The greatest reduction in sensitivity occurs in the range 220 K to 160 K, with comparably less variation with temperature at either high or low temperatures. The coefficients of sensitivity for the as grown and glycerol-soaked crystals are similar at both T=300 K and T=100 K, but glycerol reduces the sensitivity in the range 200 K to 160 K.

Thaumatin was chosen for a more comprehensive study (dataset 2), and dose curves were collected as described in the Methods section. Between 2 and 6 curves were collected at each temperature down to 170 K. All of the measured coefficients of sensitivity for each sample are shown in Figure 7.3, but they are separated by color because data for the second study were collected on a different beamline (see methods), and show a different behavior. The data are plotted on Arrhenius axes to facilitate the discussion of activation energies below.

In addition to computing the relative B-factors and coefficients of sensitivity, we have also computed the total integrated spot intensity for each dataset, and used the resulting summed intensity dose curves to determine the *half-dose* (the X-ray dose at which the total diffraction intensity has fallen to half of its initial value) for each sample. As with the relative B-factors, the summed intensity was linearly related to dose for low dose, in agreement with the previous studies that have used this metric (Owen *et al*., 2006, Southworth-Davies *et al*., 2008). A comparison plot of the two metrics for each sample is shown in Figure 7.4. The half dose is inversely

proportional ($D_{half} \sim s_{AD}^{-0.97}$) to the coefficient of sensitivity over nearly two orders of magnitude in either measure, and the average deviation is 15 %. The half dose at 100 K is in the range 30 - 50 MGy, and at 300 K the value is 1.0 - 0.6 MGy (see discussion below). As in Figure 7.3, the data are separated by which experimental setup was used.

7.4 Discussion

7.4.1 The glass transition in radiation sensitivity

In Figure 7.3, we plot the radiation sensitivity on Arrhenius axes. The slope of the curve gives the effective activation energy of the rate-limiting step, if the temperature dependence is interpreted as being a thermally activated process. (Of course it also requires the presence of ionizing radiation, but given a dose rate, the rate at which damage occurs still depends strongly on temperature.) This is a reasonable interpretation, because secondary radiation damage is thought to be due to the diffusion of radical species, or else the (diffusive) motions of the protein molecules themselves.

Between 300 K and 170 K, the sensitivities show a constant activation energy of 2.7 kcal/mol (1.8 kcal/mol for the original dataset). This value is in reasonable agreement with values for diffusion-controlled reactions of solvated electrons, H, and OH radicals with a wide variety of small molecules in solution (Anbar & Hart, 1967; Buxton *et al*., 1988). The values are predominantly in the range 3 to 4 kcal/mol. There is also fair agreement with the activation energy for diffusion in lysozyme hydration water in this temperature range, as determined with NMR And MD

simulation, 4.14 and 3.48 kcal/mol, respectively (Lagi *et al*, 2008). Protein conformational motions and folding have a wider range of activation energies, roughly from 2 to 8 kcal/mol, and also must contribute to damage in this temperature range (Wolynes *et al*., 1996; Socci *et al*; 1996; Schuler *et al*., 2002; Grabolle *et al*,2006; Munoz *et al*., 2006).

Further evidence that radiation damage is diffusion controlled in this temperature range comes from the data for crystals containing glycerol. The activation energy for diffusion in pure glycerol is 20 – 30 kcal/mol in this temperature range (Schneider *et al*., 1998; Jain *et al*., 2009), and so the fact that the addition of 40 % glycerol increases the activation energy from 2.7 to ~4.5 kcal/mol (not shown) supports the claim that radiation damage is diffusion controlled. (Note that because of coupling between the solvent and protein dynamics (Tilton *et al*., 1992; Wood *et al*., 2007; 2008a; 2008b), an increase in the activation energy for diffusion in the solvent will lead to an increase in the activation energy for (diffusive) motions of the protein surface.)

At low temperatures, diffusive motions in both the solvent and the protein are frozen out, and the temperature dependence of the damage reflects this. A transition to a nearly temperature-independent regime is observed at ~170 K. If this is taken to mean that diffusive motions are frozen out below 170 K, then the dominant source of damage in this temperature range is primary damage (defined here as the chemical and physical changes produced by the inelastically-scattered X-ray *and* the resulting spur of high-energy electrons, all of which happens in ~10^{-14} seconds.) It also means that this is another manifestation of the protein glass transition (see below).

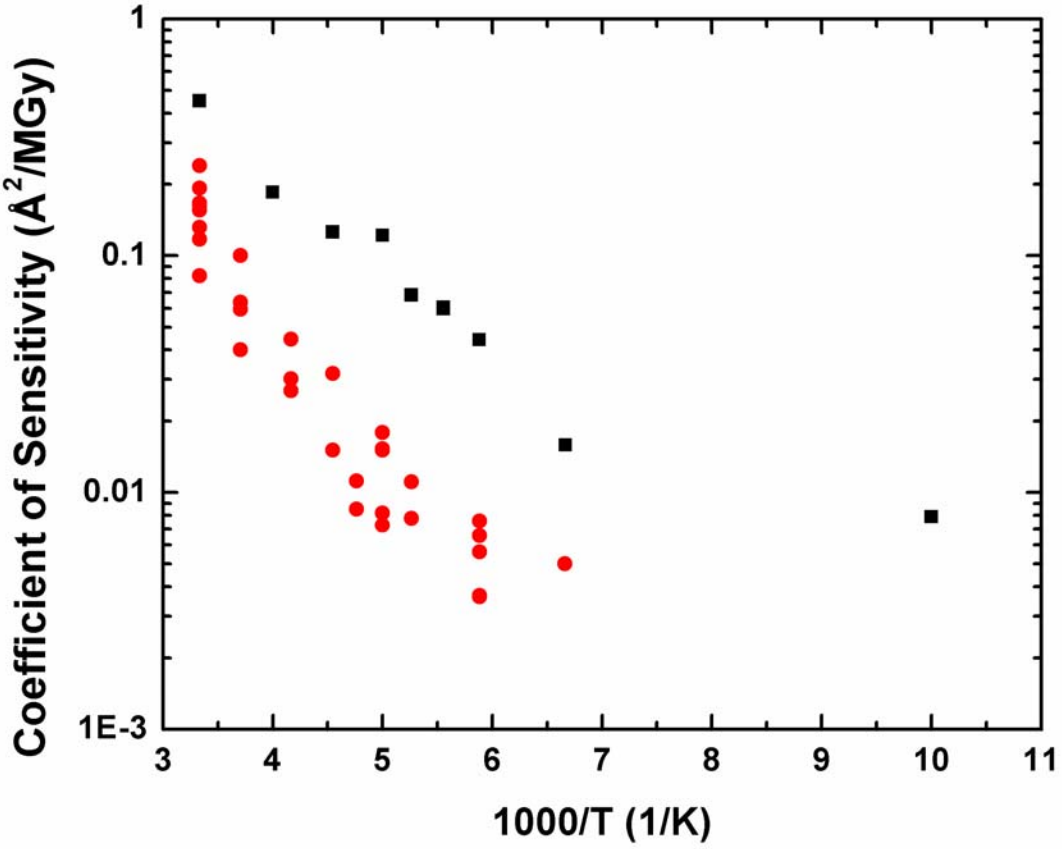

Figure 7.3

The coefficient of sensitivity of thaumatin crystals is plotted as a function of temperature for as-grown crystals and crystals soaked in 40 % (w/v) glycerol.

7.4.2 The character of global damage is temperature-independent

We have discussed two ways to quantify global radiation damage: changes in the B-factor (coefficient of sensitivity) and changes in the summed intensity (half dose). These two metrics, while related, arise from distinct physical changes in the crystal. As atoms move away from their ideal lattice positions, the intensities of reflections are reduced, more so at higher resolution. This leads to a) a reduction in the total Bragg-scatter, and b) an increase in the B-factor. This is the "disordered" state in the model of Blake & Phillips, (1962). Eventually, some atoms will have moved so far from their lattice positions that they no longer contribute to Bragg scatter at all. This is the "amorphous" state, and causes a reduction in total Bragg scatter without a corresponding increase in B-factor. The amount of each type of damage present in the crystal can be characterized by the ratio of B-factor increase to total intensity decrease ($\Delta B/\Delta I$).

It is reasonable to expect that at low temperatures, radiation damage would involve many small displacements of atoms, thus leading to mostly "disordered" protein, and $\Delta B/\Delta I$ would be comparatively large. At high temperatures, large-scale motions are possible, and the "amorphous" state is more readily reached. This suggests that $\Delta B/\Delta I$ would be comparatively low at high temperature. We find instead that $\Delta B/\Delta I$ is essentially temperature independent (Figure 7.4.) The surprising conclusion is that radiation damage proceeds along the same pathway independent of temperature, at least at low dose.

It is also evident from Figure 7.4 that the discrepancy between the two studies cannot be explained by a difference in flux calibration. A change in the flux calibration of

one dataset would shift the cluster of points along its own length, never side-to-side. This means that whatever difference exists between the two studies must be innate to either the crystals or a detail of the experimental setup that has been overlooked. We suggest that future studies quantifying radiation sensitivity report both half-dose and coefficient of sensitivity, since they do not appear to be simply related, and are known to measure different physical quantities.

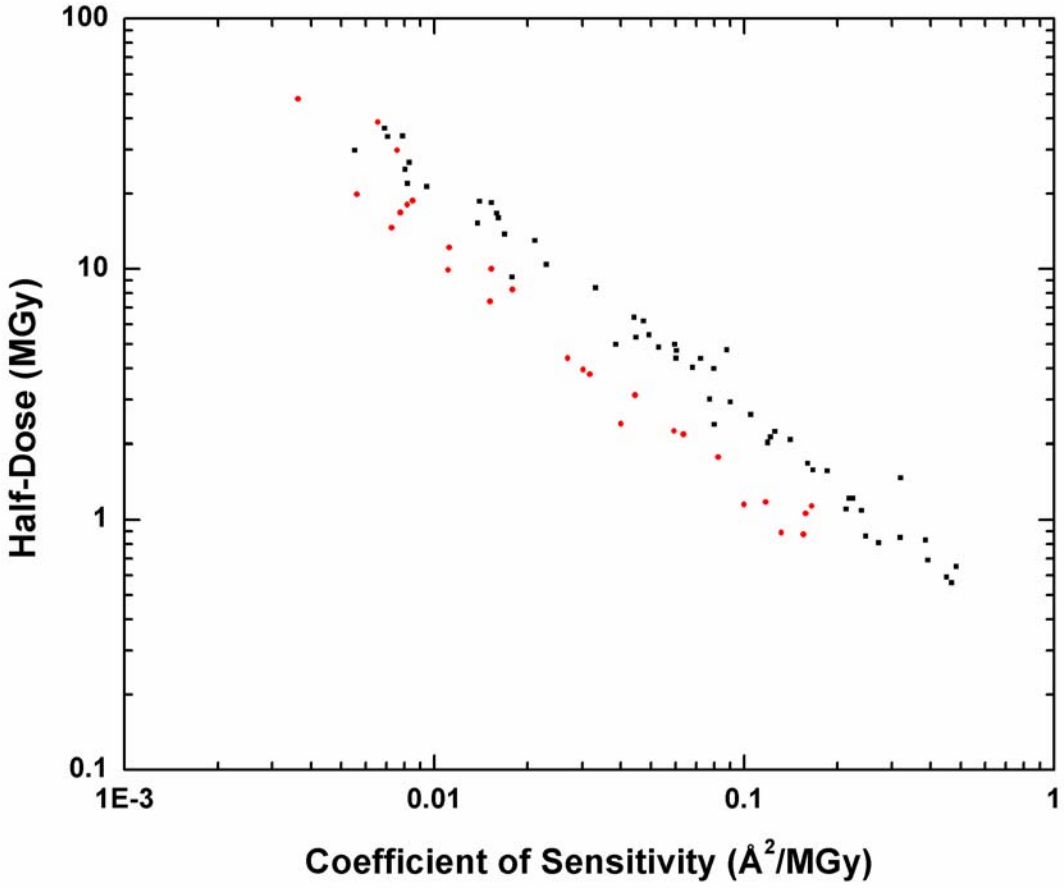

Figure 7.4

The correlation between half-dose and coefficient of sensitivity. Different studies are plotted in different colors. The difference between them cannot be explained by a difference in dose calibration alone.

7.4.3 Comparison to previous work

Where our findings for radiation sensitivity overlap with previous studies, there is at best factor-of-two agreement, which is typical for radiation damage studies conducted in different labs (see below). One factor contributing to the continuing discrepancies (even between supposedly identical experiments) is that articles rarely give all of the information needed to reconstruct exactly how sensitivity was calculated. A discussion of the many sources of error when comparing different studies is beyond the scope of this paper. Here, we simply summarize previous findings that are most readily compared to ours.

At 100 K, Kmetko *et al*. (2006) determined the coefficients of sensitivities of lysozyme and thaumatin to be 0.012 and 0.018 $Å^2$, respectively. These values are larger than many of the values found here, even up to 240 K. Teng & Moffat (2000, 2002), however, found a linear dependence of B-factor on dose, which gives a value of 0.006 $Å^2$ for lysozyme. Their 2002 study reported no temperature dependence in the range 40 to 150 K, and reported a half-intensity-dose (half dose) of ~15 MGy, which is at least half of our value of 30 - 50 MGy. Burmeister *et al*., (2000) report of a half dose of ~23 MGy for mirosinase, and Owen *et al*., (2006) found a half dose of 43 MGy for holo- and apo-ferritin, after taking account of the different absorption cross-sections of the two proteins. Owen *et al*. state that they did not take account of the extra irradiated volume due to rotating the crystal, however, and if this is taken into account (using the values they give: 100 μm square beam footprint, 200 μm cubed crystal, 30 degree range of phi), the actual half dose is 31 MGy.

Meents *et al*. (2007) measured the sensitivity of insulin and holoferritin using *I/σ(I)*, which differs from the usual method of determining half dose, however, they obtained *I/σ(I)*-half dose values of ~20-25 MGy for both protein crystals, at both 15 K and 90 K, after assuming that the iron-rich core of ferritin reabsorbs whatever Auger electrons are generated there due to an inelastic X-ray scattering event (a factor of 4 effect). They also observe a slight temperature dependence, although it is very weak compared to the one we measure between 160 K and 100 K. The weakening of the temperature dependence below 100 K is corroborated by Borek *et al*. (2007), who studied glucose isomerase. They obtained relative sensitivity data as high as 200 K, and in general found similar temperature dependencies to the ones we found, both between 100 K and 160 K, and between 160 K and 200 K (see above).

The coefficient of sensitivity can be calculated from the data given in Shimizu *et al*. (2007) for lysozyme crystals, giving very approximate values in the range 0.001 to 0.004 $Å^2$, with the smaller values obtained at higher X-ray energies (16.5 to 33 keV.) Based on the beam size, oscillation range, and the sizes of the crystals used, these sensitivities are probably understated by a factor of two, due to the irradiated volume effect. The dose calculations were performed with RADDOSE (Murray *et al*., 2004), which does not take account of this effect. This would bring most of their observed sensitivities into the range we measure.

At 300 K, Southworth-Davies *et al*., (2008) reported half doses for lysozyme crystals in the range 0.4 to 1.7 MGy, which were positively correlated with the dose rate in the range 6 to 10 Gy/s (home source). We find a half dose of 0.7 MGy, at a dose rate of 20 kGy/s. This value is in the middle of their range of half doses, which suggests that the dose rate correlation is limited to low dose rates. We also note that the

Southworth-Davies *et al*., study does not take account of the irradiated volume effect, though they provide the necessary information in their paper to do so. In some cases, the correction to the half-dose they report is in excess of a factor of two.

7.5 Conclusion

In agreement with Borek *et al*., 2007, the dependence of radiation sensitivity on temperature is relatively weak below ~170 K. This supports the conclusion that temperature-dependent studies are possible in that temperature range without much additional concern about radiation damage. This is perhaps most useful in the developing field of kinetic crystallography, where temperature can be used as a parameter to control reaction rates within crystals.

We also point out that there are clearly many factors contributing to radiation sensitivity and its measurement that have not been fully understood. We have observed variations between nominally identical experiments of up to a factor three at temperatures between 300 K and 170 K. Though these variations are smaller at lower temperatures, (see Meents *et al*., 2007), they are still considerable. While it is possible that these variations are innate to the samples themselves, further investigation is required to draw this conclusion.

Despite these difficulties, we have demonstrated an Arrhenius dependence of radiation sensitivity, with an activation energy of ~2.7 kcal/mol. This value is in the same range as that for translational diffusion of lysozyme hydration water (4.14 kcal/mol), reactions of hydrated electrons, H, and OH radicals (3 - 4 kcal/mol), and protein conformational motions (2 - 8 kcal/mol). This suggests that some combination of

these processes are responsible for protein radiation sensitivity above 170 K. Below that temperature, they are frozen out, and radiation damage must proceed without diffusional motions.

REFERENCES

Anbar, M. & Hart, E. J. (1967). *Journal of Physical Chemistry* **71**, 3700-&.

Blake, C. & Phillips, D. C. *Proceedings of the Symposium on theBiological Effects of Ionising Radiation at the Molecular Level (Vienna:International Atomic Energy Agency)*,pp. 183-191.

Bourgeois, D. & Royant, A. (2005). *Current Opinion in Structural Biology* **15**, 538-547.

Burmeister, W. P. (2000). *Acta Crystallographica Section D-Biological Crystallography* **56**, 328-341.

Buxton, G. V., Greenstock, C. L., Helman, W. P., & Ross, A. B. (1988). *Journal of Physical and Chemical Reference Data* **17**, 513-886.

Colletier, J. P., Bourgeois, D., Sanson, B., Fournier, D., Sussman, J. L., Silman, I., & Weik, M. (2008). *Proceedings of the National Academy of Sciences of the United States of America* **105**, 11742-11747.

Cowan, J. A. & Nave, C. (2008). *Journal of Synchrotron Radiation* **15**, 458-462.

Grabolle, M., Haumann, M., Muller, C., Liebisch, P., & Dau, H. (2006). *Journal of Biological Chemistry* **281**, 4580-4588.

Henderson, R. (1990). *Proceedings of the Royal Society of London Series B-Biological Sciences* **241**, 6-8.

Henderson, R. (1995). *Quarterly Reviews of Biophysics* **28**, 171-193.

Holton, J. M. (2009). *Journal of Synchrotron Radiation* **16**, 133-142.

Jain, P., Levchenko, A., Yu, P., & Sen, S. (2009). *Journal of Chemical Physics* **130**.

Lagi, M., Chu, X. Q., Kim, C. S., Mallamace, F., Baglioni, P., & Chen, S. H. (2008). *Journal of Physical Chemistry B* **112**, 1571-1575.

Leiros, H. K. S., McSweeney, S. M., & Smalas, A. O. (2001). *Acta Crystallographica Section D-Biological Crystallography* **57**, 488-497.

Leiros, H. K. S., Timmins, J., Ravelli, R. B. G., & McSweeney, S. M. (2006). *Acta Crystallographica Section D-Biological Crystallography* **62**, 125-132.

Leslie, A. G. W. (2006). *Acta Crystallographica Section D-Biological Crystallography* **62**, 48-57.

Munoz, V., Ghirlando, R., Blanco, F. J., Jas, G. S., Hofrichter, J., & Eaton, W. A. (2006). *Biochemistry* **45**, 7023-7035.

Murray, J. W., Garman, E. F., & Ravelli, R. B. G. (2004). *Journal of Applied Crystallography* **37**, 513-522.

Nave, C. & Garman, E. F. (2005). *Journal of Synchrotron Radiation* **12**, 257-260.

Otwinowski, Z. & Minor, W. (1997). *Macromolecular Crystallography, Pt A* **276**, 307-326.

Owen, R. L., Rudino-Pinera, E., & Garman, E. F. (2006). *Proceedings of the National Academy of Sciences of the United States of America* **103**, 4912-4917.

Rault, J., Neffati, R., & Judeinstein, P. (2003). *European Physical Journal B* **36**, 627-637.

Ravelli, R. B. G. & McSweeney, S. M. (2000). *Structure* **8**, 315-328.

Ravelli, R. B. G., Theveneau, P., McSweeney, S., & Caffrey, M. (2002). *Journal of Synchrotron Radiation* **9**, 355-360.

Ravelli, R. B. G., Leiros, H. K. S., Pan, B. C., Caffrey, M., & McSweeney, S. (2003). *Structure* **11** , 217-224.

Ravelli, R. B. G., Nanao, M. H., Lovering, A., White, S., & McSweeney, S. (2005). *Journal of Synchrotron Radiation* **12**, 276-284.

Schneider, U., Lunkenheimer, P., Brand, R., & Loidl, A. (1998). *Journal of Non-Crystalline Solids* **235**, 173-179.

Schuler, B., Lipman, E. A., & Eaton, W. A. (2002). *Nature* **419**, 743-747.

Shimizu, N., Hirata, K., Hasegawa, K., Ueno, G., & Yamamoto, M. (2007). *Journal of Synchrotron Radiation* **14**, 4-10.

Singh, A. & Singh, H. (1982). *Progress in Biophysics & Molecular Biology* **39**, 69-107.

Sliz, P., Harrison, S. C., & Rosenbaum, G. (2003). *Structure* **11**, 13-19.

Socci, N. D., Onuchic, J. N., & Wolynes, P. G. (1996). *Journal of Chemical Physics* **104**, 5860-5868.

Southworth-Davies, R. J., Medina, M. A., Carmichael, I., & Garman, E. F. (2007). *Structure* **15**, 1531-1541.

Tilton, R. F., Dewan, J. C., & Petsko, G. A. (1992). *Biochemistry* **31**, 2469-2481.

Warkentin, M. & Thorne, R. E. (2008). *Journal of Applied Crystallography* **41**, 791-797.

Weik, M., Ravelli, R. B. G., Kryger, G., McSweeney, S., Raves, M. L., Harel, M., Gros, P., Silman, I., Kroon, J., & Sussman, J. L. (2000). *Proceedings of the National Academy of Sciences of the United States of America* **97**, 623-628.

Weik, M., Kryger, G., Schreurs, A. M. M., Bouma, B., Silman, I., Sussman, J. L., Gros, P., & Kroon, J. (2001). *Acta Crystallographica Section D-Biological Crystallography* **57**, 566-573.

Weik, M., Vernede, X., Royant, A., & Bourgeois, D. (2004). *Biophysical Journal* **86**, 3176-3185.

Weik, M., Schreurs, A. M. M., Leiros, H. K. S., Zaccai, G., Ravelli, R. B. G., & Gros, P. (2005). *Journal of Synchrotron Radiation* **12**, 310-317.

Wolynes, P. G., LutheySchulten, Z., & Onuchic, J. N. (1996). *Chemistry & Biology* **3**, 425-432.

Wood, K., Plazanet, M., Gabel, F., Kessler, B., Oesterhel, D., Tobias, D. J., Zaccai, G., & Weik, M. (2007). *Proceedings of the National Academy of Sciences of the United States of America* **104**, 18049-18054.

Wood, K., Plazanet, M., Gabel, F., Kessler, B., Oesterhelt, D., Zaccai, G., & Weik, M. (2008). *European Biophysics Journal with Biophysics Letters* **37**, 619-626.

Wood, K., Frolich, A., Paciaroni, A., Moulin, M., Hartlein, M., Zaccai, G., Tobias, D. J., & Weik, M. (2008). *Journal of the American Chemical Society* **130**, 4586-4591.

APPENDIX A

A PROTEIN CRYSTAL AS A COMPRESSION CELL, AND THE LIQUID-LIQUID PHASE TRANSITION IN SUPERCOOLED WATER

A.1 Introduction

The following is a manuscript that, at the time of this writing, has not been submitted to a journal. The implications of the supposed finding are far-reaching, and of immense scientific interest, but the evidence is not conclusive. In particular, the abrupt unit-cell contraction shown in Figure A.2 can be explained by the formation of a small amount of ice in the crystals. In Chapter 6 it is argued that up to ~1 % of a protein crystal may be ice without the signal being detectable by X-ray diffraction. While the contractions of the solvent space shown in Figure A.2 are 4 and 9 %, the ~1 % estimate from Chapter 6 is an order-of-magnitude estimate only.

A.2 Manuscript

Recent results[1-3] for supercooled water confined to nanometer-sized pores have demonstrated many of the features of the highly-anticipated liquid-liquid phase boundary[4-6]. These studies have the advantage that water in pores smaller than ~2 nm does not crystallize[7], allowing access to the supercooled state at any temperature. Still, no direct observation of the phase transition (i.e. an abrupt change in density as a function of temperature or pressure) exists in the temperature range where water is a liquid (above 150 K). Here we describe how the solvent confined to the 1 to 2 nm channels in a protein crystal pressurizes as

the system cools, so that the trajectory taken through the *P-T* plane crosses the likely location of the liquid-liquid phase boundary at ~210 K. We then present cooling experiments in which an abrupt ~4-9% increase in density is observed at this temperature in two different protein crystal systems (tetragonal lysozyme and orthorhombic trypsin), which we attribute to this crossing. These results will inform more detailed studies of this transition in the future, as well as open the door to temperature-dependent studies of protein crystal systems.

It has been known for a long time that the various thermodynamic properties of water show anomalous behavior on supercooling, appearing to diverge at temperatures just below the homogenous nucleation temperature[8-10]. This, combined with the discovery of a first order phase transition between two amorphous forms of ice as a function of pressure[11], led some to speculate that this phase boundary extends to higher temperatures, either terminating at a critical point[4], or else connecting to the liquid-vapor phase boundary at negative pressures[12]. The location of the phase boundary in the temperature range 200-230 K has been investigated by compression/decompression induced melting experiments[13,14], neutron measurements of the fragile-to-strong crossover[15], computer simulations[16,17], and scaling theory[18], among others, reviewed by Stanley and Mishima[5]. Additionally, the notion of the phase boundary terminating at a critical point, as opposed to continuing to negative pressures, is supported by ambient pressure measurements of heat capacity[3], density[1], and relaxation-time/diffusivity[2]. They show a continuous evolution, with anomalies where the phase boundary would be, were there no critical point. This line, along which fluctuations are maximal, is the continuation of the phase boundary past the critical point, and is called a Widom line[19].

The investigations described above must contend with the fact that supercooled water spontaneously crystallizes below ~235 K at ambient pressure[8]. This difficulty can be avoided by working with water confined to nanopores no larger than ~2 nm[7]. Previously, porous silica[1-3] has been used to achieve confinement. We recognize that in protein crystals, water is confined to solvent channels in the range 1 to 2 nm (and up), and focus on the protein crystal system as a possible place to study the properties of supercooled water. One immediate advantage is that in X-ray diffraction, the unit cell volume can be determined very accurately, providing a measurement of the density. Another interesting twist in protein crystal systems is that simply lowering the temperature can create large pressures, as we will now describe.

As a protein crystal cools, the protein molecules move closer together, reducing the total volume available to the solvent. At the same time, the solvent should be expanding, so it must either compress or flow (to the surface of the crystal or to a grain boundary). Since a pressure is required to drive the flow, compression and flow will happen simultaneously. Near the vicinity of the critical point, the compressibility, expansivity, and viscosity of the solvent are not known, however what data are available can be used to produce an estimate of the trajectory that the system follows through the *P*-*T* plane.

Using constant values of α_s and κ for the expansivity and compressibility of the solvent, and α_c for the thermal contraction coefficient of the protein lattice, it can be shown that the slope of the trajectory is $(\alpha_s - \alpha_c)/\kappa$ in the absence of flow. To the extent that flow also occurs, the slope will be less than this value. In the opposite limit, the solvent is incompressible. If the protein crystal is modeled as a tube of

length L and diameter d, with L being the average grain size and d being the channel diameter, the pressure required to drive a flow of rate v through the tube is

$$p = \frac{128\eta L}{\pi d^4} v \tag{1}$$

The flow rate is related to the temperature through the cooling rate and the thermal expansion coefficients of the crystal lattice and solvent. This condition sets a maximum on the pressure at any given temperature. The trajectory taken by the crystal is then the one that never exceeds either maximum: it follows (1) if the slope is less than $(\alpha_s - \alpha_c)/\kappa$, otherwise it follows a straight line of slope $(\alpha_s - \alpha_c)/\kappa$.

A trajectory of the type described is shown in Figure A.1, along with data and estimates of the location of the critical point and phase boundary. Due to uncertainties in both the trajectory and the phase boundary, the temperature at which they cross cannot be predicted with precision. There is also the question of how large a region of metastability exists at this temperature, which might allow the sample to remain untransformed long after crossing the equilibrium phase boundary. However, it should be clear from the figure that the crossing is inevitable, and is likely to be in the range 200 - 220 K.

At this temperature, the pressure is in the range 100 - 200 MPa. It is important to note that the bulk modulus of protein crystals is 2.7 - 5.3 GPa at room temperature[20], and that it increases rapidly with decreasing temperature[21]. At a temperature of 210 K, it is likely to be in excess of 10 GPa, so the strain at 100 MPa is only 1%, still in the elastic regime.

The results of two separate experiments of the type described above are shown in Figure A.2. For both a lysozyme and trypsin crystal, a constant contraction of the unit

cell volume is observed down to a temperature of ~210 K, at which point an abrupt decrease occurs. This coincides with a shift in the intensity of the diffuse scatter to larger scattering-angle (smaller *d*-spacing), indicating that the amorphous solvent in the sample has undergone an abrupt increase in density. We attribute this density increase to the crossing of the liquid-liquid phase boundary pictured in Figure A.1.

One important assumption in the calculation of the *P*-*T* trajectory shown in Figure A.1 is that the grain size is large. In order for pressure to build up, the solvent must need to flow a large distance (~100 μm), before reaching a grain boundary. Evidence that this is the case comes from two measures of crystalline order shown in Figure A.3. That they both remain constant down to the transition temperature implies that a relatively minor amount of solvent has escaped the crystalline lattice (see caption). The sharp jump in these measures of disorder is consistent with a first-order transition, in which a front of phase transformation sweeps through the sample, causing many tiny cracks, as has been observed for the same transition at ~140 K[22].

There are a number of reasons to expect that the transition described here should differ from that in pure, bulk water. The most obvious is the confinement, but this has been discussed previously, and has been shown in several studies not to have a major effect[1-3,7,23,24]. There is also the effect of the protein side-chains, which have been shown to decrease the diffusion constant of protein hydration water by a factor of 10[23]. Finally there are the solutes contained in the solutions from which the crystals grew. For lysozyme there is 1.2 M NaCl, and for trypsin there is 25 % PEG 6000. The effect of solutes on the thermodynamic properties of water -- in particular, the location of phase boundaries -- has been shown to be equivalent to that of an effective pressure, through the two variables' effect on the water activity[25]. Thus one would expect that solutes (or side chains) would shift the phase boundary to lower pressures, and this has

been demonstrated by Mishima[26]. Based on their correspondence through water activity, and on Mishima's measurements in LiCl solutions, the solutions used in this study are expected to shift the phase boundaries for lysozyme and trypsin to lower pressures approximately 50 MPa. This also explains why the same experiment, with the inclusion of 40 % glycerol, shows no phase transition (data not shown): in that case the phase boundary would be shifted entirely to negative pressures, and the solvent would always be in the high-density-like phase.

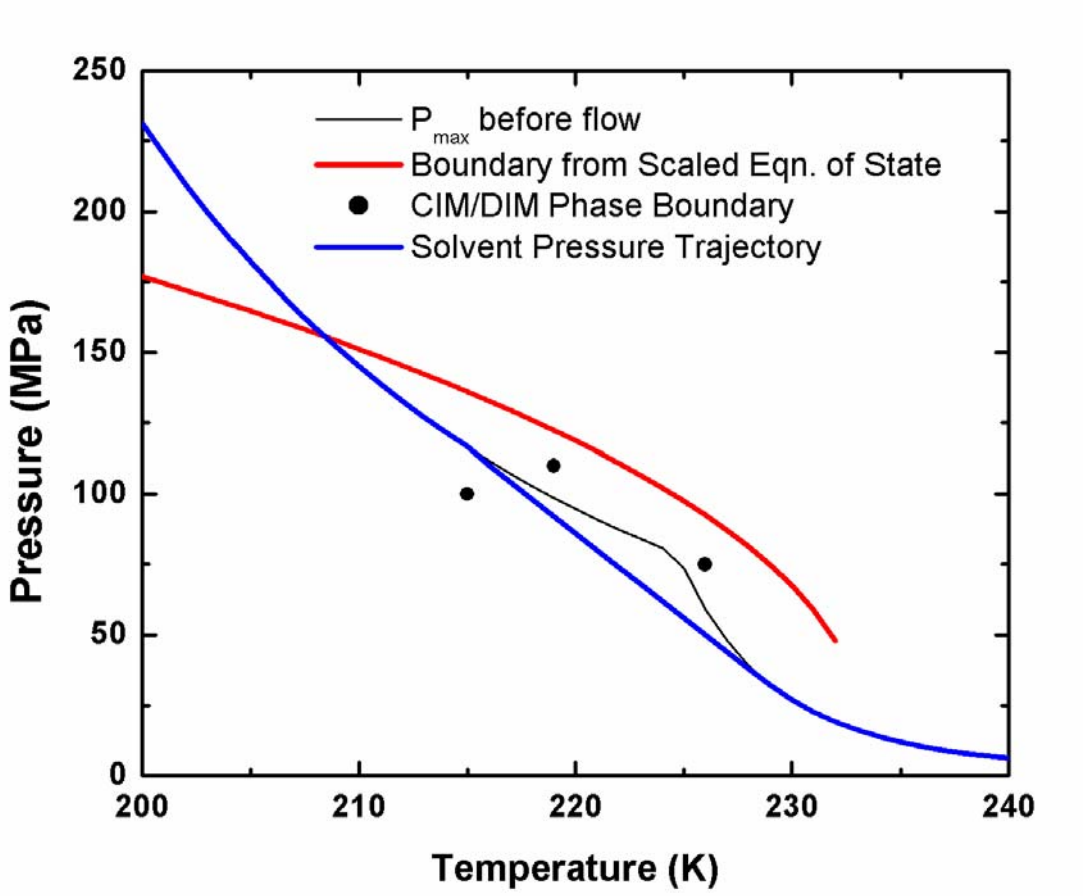

Figure A.1

The *P-T* phase diagram of supercooled water is shown, with the trajectory of a protein crystal being cooled at 0.1 K/s superimposed. Black circles are points from compression/decompression induced melting of H_2O and D_2O ices, and the red line is the result from a semi-empirical equation of state[18] based on data from ref. 26. The maximum pressure attainable in the crystal is shown as a thin black line, and this line is the trajectory followed by the system when its slope is less than $(\alpha_s - \alpha_c)/\kappa$ (see text). Otherwise the trajectory is a line of that slope. Viscosity values used are the geometrical average of T/D measurements in pure confined water[2], and protein hydration water[24], linearly scaled so as to agree with actual viscosity measurements in pure water[27].

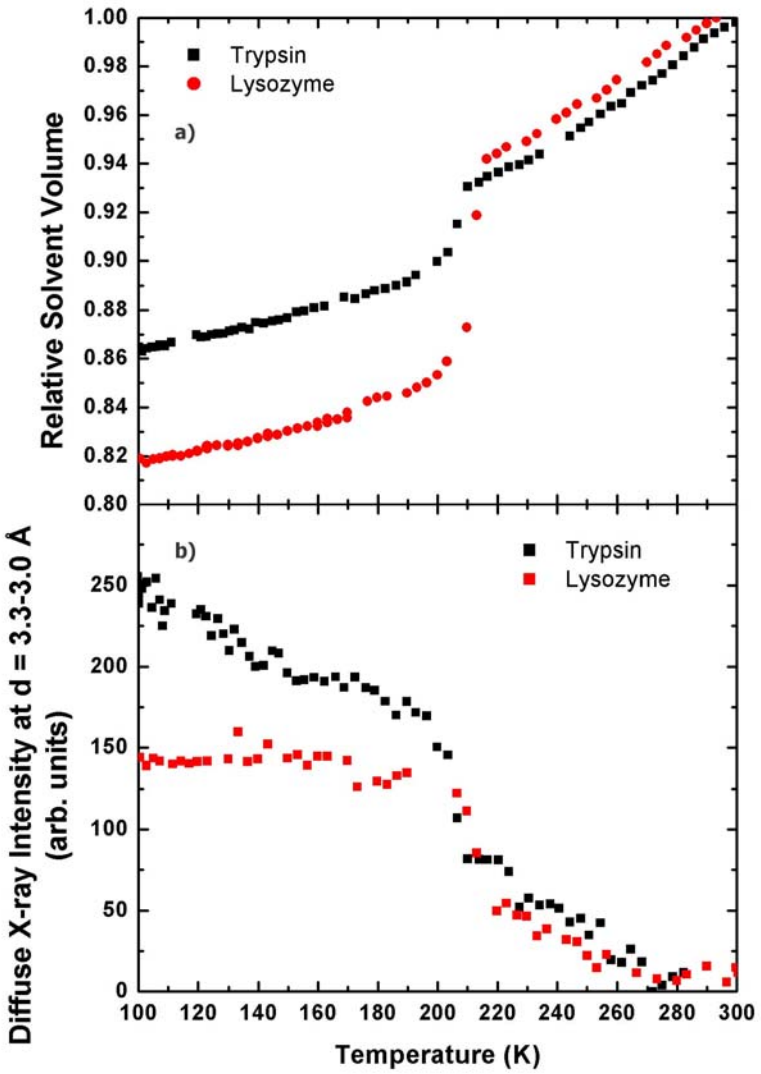

Figure A.2

The result of slow-cooling experiments on lysozyme and trypsin crystals. Panel a) shows the relative change in the volume of the confined solvent, determined from unit cell measurements, and corrected for the contraction of the protein molecule[28], and the solvent fraction of the cell in lysozyme and trypsin. In panel b), the relative change in intensity of the diffuse scatter in the resolution range 3 - 3.3 Å is shown, where the smooth variation is due to the contraction of the oil surrounding the crystal. In both panels, an abrupt transition at ~210 K is evident, indicating a density increase of 9% for the lysozyme solvent and 4% for the trypsin solvent.

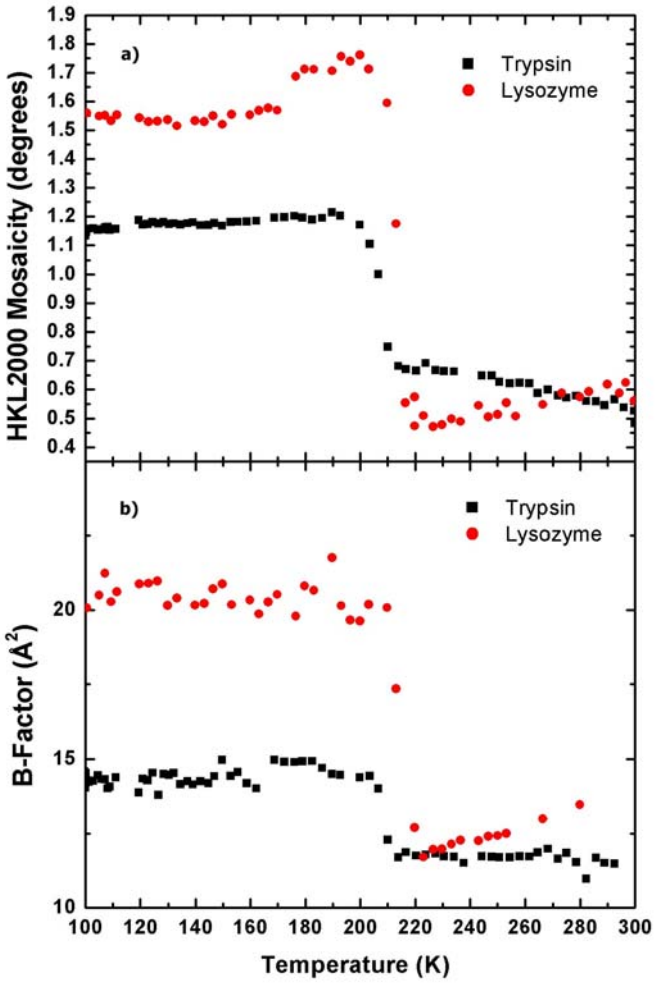

Figure A.3

The mosaicity a), and b-factor b), for both crystals. The fact that they are relatively temperature independent down to the transition temperature indicates that the crystals are composed of a small number of large grains, and that they contract and pressurize uniformly. If there were many small grains, a large amount (~5% of total sample volume[28]) of solvent would flow to grain boundaries, resulting in increased misalignment of the grains, and increased disorder. The mosaicity is a measure of the width of the angular distribution of grains, and the b-factor is proportional to the root-mean-square displacements of individual atoms from their locations in an ideal lattice. Both were determined using the HKL 2000 suite.

The difference in the density jumps in trypsin and in lysozyme may be accounted for by this difference in their solution activity. It may also have to do with the greater disorder in the trypsin crystal, which could be due in part to more grain boundaries. While many grains were large enough to produce the necessary pressure, some fraction of the grains in both crystals surely were not, and remained in the low-density phase. In this view, both the ~4% density jump in trypsin and the ~9% density jump in lysozyme should represent lower limits on the true value of the density discontinuity across the phase boundary in pure water.

Finally we will address the question of the reproducibility of these results. The most common outcome when slowly cooling lysozyme or trypsin crystals is a curve that looks very much like that in Figure A.2, except that the sudden contraction of the solvent is typically so large that it results in a total loss of diffraction from the crystal, terminating the experiment at ~200 K. We have observed this type of sudden contraction in lysozyme, trypsin and (less often) in thaumatin crystals, always between 200 and 225 K, and only when using the pure solutions from which the crystals grew -- never in the presence of 30 - 40% glycerol or equivalent. Since the transition always occurs in a narrow range of temperature, is seen to be very similar across several different protein crystal systems, and is eliminated by the addition of too much glycerol, we conclude that it is a feature of the aqueous solvent. In particular, it is the first (albeit uncontrolled) observation of the liquid-liquid phase transition in supercooled water.

REFERENCES

1. Mallamace, F. *et al.* The anomalous behavior of the density of water in the range 30K < T < 373K. *Proceedings of the National Academy of Sciences of the United States of America* **104**, 18387-18391 (2007).

2. Chen, S. H. *et al.* The violation of the Stokes-Einstein relation in supercooled water. *Proceedings of the National Academy of Sciences of the United States of America* **103**, 12974-12978 (2006).

3. Oguni, M., Maruyama, S., Wakabayashi, K. & Nagoe, A. Glass transitions of ordinary and heavy water within silica-gel nanopores. *Chemistry-An Asian Journal* **2**, 514-520 (2007).

4. Poole, P. H., Sciortino, F., Essmann, U. & Stanley, H. E. Phase-Behavior of Metastable Water. *Nature* **360**, 324-328 (1992).

5. Mishima, O. & Stanley, H. E. The relationship between liquid, supercooled and glassy water. *Nature* **396**, 329-335 (1998).

6. Mishima, O. Application of polyamorphism in water to spontaneous crystallization of emulsified LiCl-H2O solution. *Journal of Chemical Physics* **123**, (2005).

7. Rault, J., Neffati, R. & Judeinstein, P. Melting of ice in porous glass: why water and solvents confined in small pores do not crystallize? *European Physical Journal B* **36**, 627-637 (2003).

8. Debenedetti, P. G. Supercooled and glassy water. *Journal of Physics-Condensed Matter* **15**, R1669-R1726 (2003).

9. Kanno, H. & Angell, C. A. Water - Anomalous Compressibilities to 1.9-Kbar and Correlation with Supercooling Limits. *Journal of Chemical Physics* **70**, 4008-4016 (1979).

10. Hare, D. E. & Sorensen, C. M. Densities of Supercooled H2O and D2O in 25-Mu Glass-Capillaries. *Journal of Chemical Physics* **84**, 5085-5089 (1986).

11. Mishima, O. Reversible 1St-Order Transition Between 2 H2O Amorphs at Similar-To-0.2 Gpa and Similar-To-135-K. *Journal of Chemical Physics* **100**, 5910-5912 (1994).

12. Speedy, R. J. Stability-Limit Conjecture - An Interpretation of the Properties of Water. *Journal of Physical Chemistry* **86**, 982-991 (1982).

13. Mishima, O. & Stanley, H. E. Decompression-induced melting of ice IV and the liquid-liquid transition in water. *Nature* **392**, 164-168 (1998).

14. Mishima, O. Liquid-liquid critical point in heavy water. *Physical Review Letters* **85**, 334-336 (2000).

15. Liu, L., Chen, S. H., Faraone, A., Yen, C. W. & Mou, C. Y. Pressure dependence of fragile-to-strong transition and a possible second critical point in supercooled confined water. *Physical Review Letters* **95**, (2005).

16. Harrington, S., Zhang, R., Poole, P. H., Sciortino, F. & Stanley, H. E. Liquid-liquid phase transition: Evidence from simulations. *Physical Review Letters* **78**, 2409-2412 (1997).

17. Sciortino, F., Poole, P. H., Essmann, U. & Stanley, H. E. Line of compressibility maxima in the phase diagram of supercooled water. *Physical Review e* **55**, 727-737 (1997).

18. Fuentevilla, D. A. & Anisimov, M. A. Scaled equation of state for supercooled water near the liquid-liquid critical point. *Physical Review Letters* **97**, (2006).

19. Xu, L. M. *et al.* Relation between the Widom line and the dynamic crossover in systems with a liquid-liquid phase transition. *Proceedings of the National Academy of Sciences of the United States of America* **102**, 16558-16562 (2005).

20. Speziale, S. *et al.* Sound velocity and elasticity of tetragonal lysozyme crystals by Brillouin spectroscopy. *Biophysical Journal* **85**, 3202-3213 (2003).

21. Morozov, V. N. & Morozova, T. Y. Elasticity of Globular-Proteins - the Relation Between Mechanics, Thermodynamics and Mobility. *Journal of Biomolecular Structure & Dynamics* **11**, 459-481 (1993).

22. Mishima, O. & Suzuki, Y. Propagation of the polyamorphic transition of ice and the liquid-liquid critical point. *Nature* **419**, 599-603 (2002).

23. Liu, L. *et al.* Quasielastic and inelastic neutron scattering investigation of fragile-to-strong crossover in deeply supercooled water confined in nanoporous silica matrices. *Journal of Physics-Condensed Matter* **18**, S2261-S2284 (2006).

24. Mallamace, F. *et al.* Role of the solvent in the dynamical transitions of proteins: The case of the lysozyme-water system. *Journal of Chemical Physics* **127**, (2007).

25. Koop, T., Luo, B. P., Tsias, A. & Peter, T. Water activity as the determinant for homogeneous ice nucleation in aqueous solutions. *Nature* **406**, 611-614 (2000).

26. ocrystallization of emulsified LiCl-H2O solution. *Journal of Chemical Physics* **123**, (2005).

27. Osipov Y.A., Zheleznyi B.V. & Bondarenko N.F. The Shear Viscosity of Water Supercooled to -35 C. *Russian Journal of Physical Chemistry* **51**, 748-749 (1977).

28. Juers, D. H. & Matthews, B. W. Reversible lattice repacking illustrates the temperature dependence of macromolecular interactions. *Journal of Molecular Biology* **311**, 851-862 (2001).